Improving nuclear physics models for neutron star crusts

Matthew Shelley

Doctor of Philosophy

University of York
Physics
April 2021

Abstract

The composition of the inner and outer crusts of neutron stars is explored, using nuclear models with considerable improvements.

We first directly compare the Hartree–Fock–Bogoliubov method and the extended Thomas–Fermi + Strutinsky integral (ETFSI) method in the inner crust, and find a large energy discrepancy, caused by the lack of neutron paring correlations in the ETFSI method. We implement neutron pairing using the local-density approximation, and find that the energy discrepancy is essentially eliminated.

We systematically investigate the inner crust using a variety of Skyrme energy density functionals, and find that there is a strong correlation between the pure neutron matter (PNM) equation of state (EoS) of a functional, and its predictions for the proton fraction and pressure in the inner crust. This calls for the use of Skyrme functionals with more stringent constraints on the low-density part of the PNM EoS.

Finally, we present a new mass model for the outer crust, where the existing *DZ10* model is supplemented with a Gaussian process term. This new model provides reliable extrapolation beyond the limit of measured nuclei, and crucially comes with error bars, so that predictions for the outer crust composition can be given with confidence intervals.

Contents

List of Figures

List of Tables

List of abbreviations

NS	neutron star
TOV	Tolman–Oppenheimer–Volkoff
EoS	equation of state
WS	Wigner–Seitz
ETF	extended Thomas–Fermi
ETFSI	extended Thomas–Fermi + Strutinsky integral
HF	Hartree–Fock
HFB	Hartree–Fock–Bogoliubov
BCS	Bardeen–Cooper–Schrieffer
LDA	local-density approximation
INM	infinite nuclear matter
PNM	pure neutron matter
SNM	symmetric nuclear matter
GP	Gaussian process

Acknowledgements

I would first like to thank my supervisors, Alessandro and Christian, for all the great advice and encouragement through both the easy and difficult times — from my Binding Blocks summer project and MPhys project to my PhD work. After Christian's initial inspiration five years ago for us to use Gaussian processes, I am still constantly looking for exciting new applications for them in my future work. Thank you especially to Alessandro, whose expertise on neutron star crusts made this PhD project go so smoothly. Thank you also to Rex, who was a great TAP panel member, and always showed a keen interest in my research.

Thank you to David, Antonio, Juan, Ben, Mei, Irene, Ryan, Chris, Suso, Sivi, Ruth, and Gustavo, for endless fun and laughs. Thank you to everyone with whom I had Zoom and Skype calls throughout the lockdowns, which definitely made working from home a lot more manageable. Thank you to my parents for always being supportive and expressing their interest in my work. And finally, thank you to Jenn, without whom my PhD journey would have been a lot more difficult, especially given the pandemic circumstances!

This project was supported by STFC Grant No. ST/P003885/1.

Author's declaration

I declare that this thesis is a presentation of original work and that I am the sole author. This work has not previously been presented for an award at this university or at any other. All sources are acknowledged as references.

The present work led to the publication of five original articles:

- M Shelley, P Becker, A Gration, and A Pastore. "Advanced Statistical Methods to Fit Nuclear Models". *Acta Physica Polonica B Proceedings Supplement* **12** (2019), 649.
- M Shelley and A Pastore. "How accurately can the extended Thomas–Fermi method describe the inner crust of a neutron star?" *Journal of Physics: Conference Series* **1668** (2020), 012037.
- M Shelley and A Pastore. "Comparison between the Thomas—Fermi and Hartree–Fock–Bogoliubov Methods in the Inner Crust of a Neutron Star: The Role of Pairing Correlations". *Universe* **6** (2020), 206.
- M Shelley and A Pastore. "Systematic analysis of inner crust composition using the extended Thomas–Fermi approximation with pairing correlations". *Physical Review C* **103** (2021), 035807.
- M Shelley and A Pastore. "A new mass model for nuclear astrophysics: crossing 200 keV accuracy". (Submitted to *Universe*, under review.) Mar. 31, 2021. arXiv: 2102.07497v2 [nucl-th].

This followed the work of my MPhys project, which led to the publication of two original articles:

- A Pastore, M Shelley and CA Diget. "Impact Of Pairing Correlations On The Chemical Composition Of The Inner Crust Of A Neutron Star". *Proceedings of Science (INPC 2016)* **281** (2017), 145.
- A Pastore, M Shelley and CA Diget. "A new statistical method for the structure of the inner crust of neutron stars". *Journal of Physics G: Nuclear and Particle Physics* **44** (2017), 094003.

As part of my physics outreach work with the Binding Blocks project[1], I co-authored a further two articles:

- CA Diget et al. (including M Shelley). “Binding blocks: building the Universe one nucleus at a time”. *Physics Education* **52** (2017), 024001.
- EC Simpson and M Shelley. “Nuclear cartography: patterns in binding energies and subatomic structure”. *Physics Education* **52** (2017), 064002.

---

[1] `http://york.ac.uk/physics/public-and-schools/secondary/binding-blocks`

Chapter 1

Introduction

1.1 History, formation, and phenomenology

Neutron stars are fascinating objects: with a typical mass of 1.5 times the mass of the sun, and radius $R \approx 12$ km [Gre19], they are an ideal laboratory to study the properties of nuclear matter under extreme conditions. They bring together numerous fields of physics, from solid state and nuclear physics to general relativity and astronomy.

The existence of an ultra-dense star, composed of entirely of neutrons, was first proposed by Landau in 1932 [Lan32]. Two years later, Baade and Zwicky then suggested that neutron stars could be the final stage of stars after having undergone supernova explosions [BZ34]. The equations to determine the structure of a spherically-symmetric star using General Relativity were developed in 1939, by Tolman [Tol39] and also by Oppenheimer and Volkoff [OV39]. These same TOV equations were solved by Oppenheimer and Volkoff, by assuming that a neutron star is composed of a simple non-interacting neutron gas, and are still used to this day in the global modelling of neutron stars.

The first observations came in 1967, when PhD student Jocelyn Bell together with Antony Hewish detected periodic pulses of radio waves every 1.337 s [Hew68], and suggested that the source of this *pulsar* could be either a neutron star or a white dwarf. It was confirmed as a neutron star the following year [Gol68].

As depicted in Fig. 1.1, neutron stars are the remnants of core-collapse supernova explosions which occur at the end of the life of massive stars, i.e., with a mass of $M \approx 10 - 20 M_\odot$, where $M_\odot$ is the mass of the Sun [CH08]. After successive fusion reactions create layers of increasingly heavy elements inside the massive star, a core of ^{56}Fe begins to form. Being the isotope with the highest binding energy per nucleon, it is no longer energetically favourable to form heavier elements through fusion, and instead the iron core grows. It is supported temporarily by the

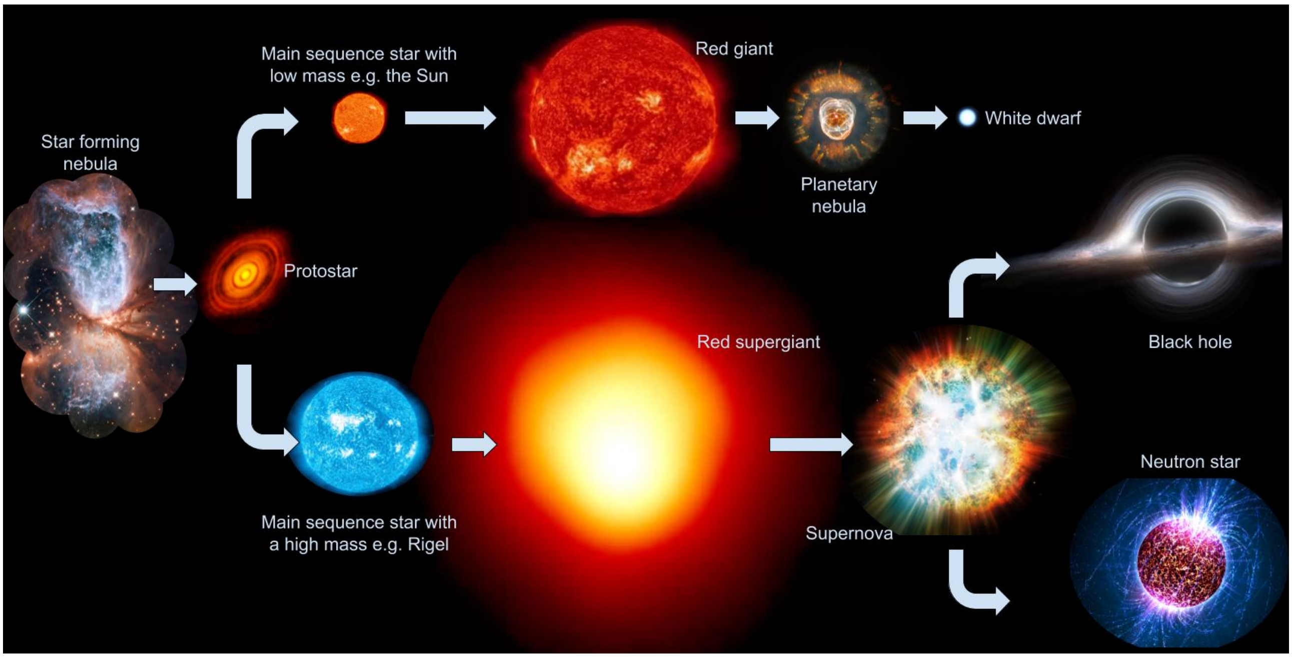

Figure 1.1: The stellar life cycle.

degenerate relativistic electron gas present in the core, but as the core grows, the electron fraction decreases, and the core rapidly decreases in size [ST08], forming the beginnings of a neutron star. The observed supernova explosion comes from the rapid contraction of the upper layers of the star, followed by their bouncing off the core, helped by large amounts of heating from the escaping neutrinos. A huge amount of gravitational energy is released in this explosion ($> 10^{46}$ J).

Many neutron stars are often found in binary systems, where the companion star can be a variety of objects, from a main sequence star to another neutron star. They have a wide range of masses, as shown in Fig. 1.2. They typically rotate with highly stable frequencies between $\approx 1 - 800$ Hz, which we now observe not only at radio frequencies but also as X-ray and gamma-ray emissions. Occasionally however they undergo *pulsar glitches*, where there is a sudden increase in rotation speed. Explaining this phenomenon requires a detailed description of the outer layers of the neutron star, including the superfluid neutrons within. Today, we can now observe neutron stars as sources of both electromagnetic and gravitational [Abb17] radiation concurrently. The gravitational wave observations in particular offer new possibilities of constraints on the equation of state (EoS) of nuclear matter, especially with next-generation detectors.

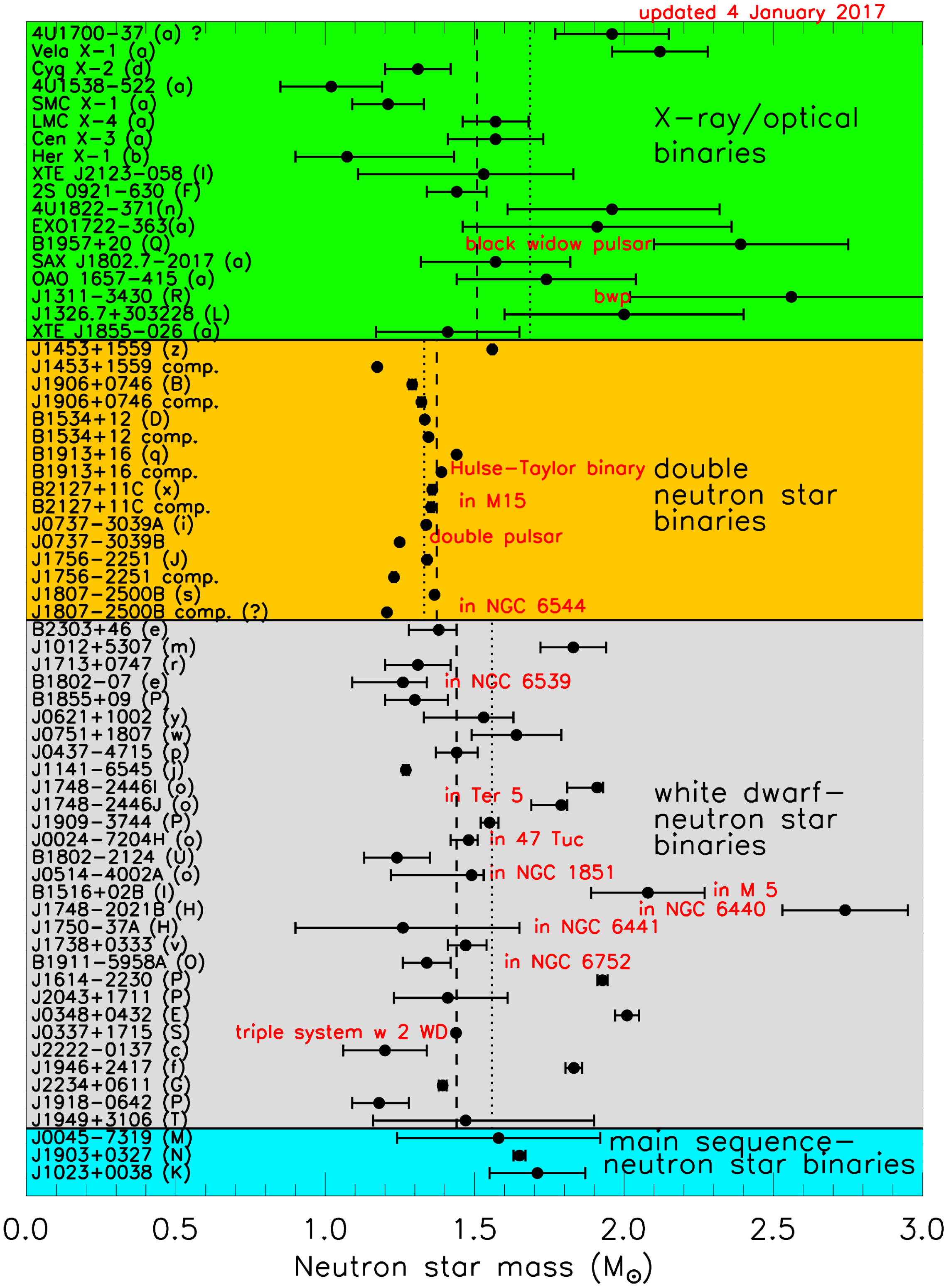

Figure 1.2: All measured masses of pulsars in binary systems, in units of solar masses, as of January 2017. Image taken from Ref. [Lat19].

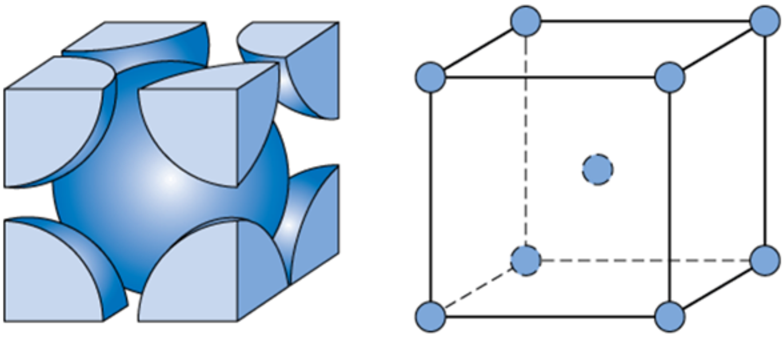

Figure 1.3: The BCC (body-centred cubic) lattice structure, as found in neutron star crusts. Each lattice site, as shown in the right panel, is occupied by a nucleus (outer crust) or nuclear cluster (inner crust).

1.2 Structure

Due to a strong pressure gradient, the matter within a neutron star arranges itself into layers with different properties [CH08]. Going from the most external regions of the star to its centre, the matter density ρ spans several orders of magnitude from $\approx 10^{-11} n_0$ to $\approx$ 3–5n_0, where $n_0 = 0.16\ \mathrm{fm}^{-3} \approx 2.7 \times 10^{14}\mathrm{g\,cm}^{-3}$ is the typical value of the density at the centre of an atomic nucleus [RS80], called the *saturation density*.

Due to the extreme pressure gradient, neutron star matter is not homogeneous. With current models [CH08], one can identify two main regions. Near the surface is the *crust*, which has a crystalline structure, represented schematically in Fig. 1.3, comprising neutrons and protons in nuclei or nuclear clusters. This crystal structure is known to be a body-centred cubic lattice (BCC) [CH08; BC18]; in the right panel of this figure, each lattice site is occupied by a nucleus in the outer crust, or a large neutron-rich nuclear cluster in the inner crust.

Going further towards to the centre of the star, there is a gradual transition through a *pasta* phase to a liquid phase [Man20] in the core [Xu09], whose composition is still under debate [LP04; Alf07; CV16; Vid18; LSW18]. These various layers are depicted in Fig. 1.4.

The crust spans a density range of $\approx 10^{-8} n_0$ to $\approx 0.5 n_0$. Although the crust only accounts for a small fraction of the mass of the neutron star, it plays a major role in a variety of astrophysical phenomena, including the r-process [Lat77], short gamma-ray burst precursors caused by resonant shattering [Tsa12a], soft gamma-ray repeater giant flares [TD95; SW06], and thermal relaxation in soft x-ray transients. The EoS of the crust is also believed to influence many properties of neutron stars, such as the moment of inertia [Cha13; PFH14] which influences pulsar glitches, transport phenomena within the star [LEL99; BRT06; Bro00], the relation be-

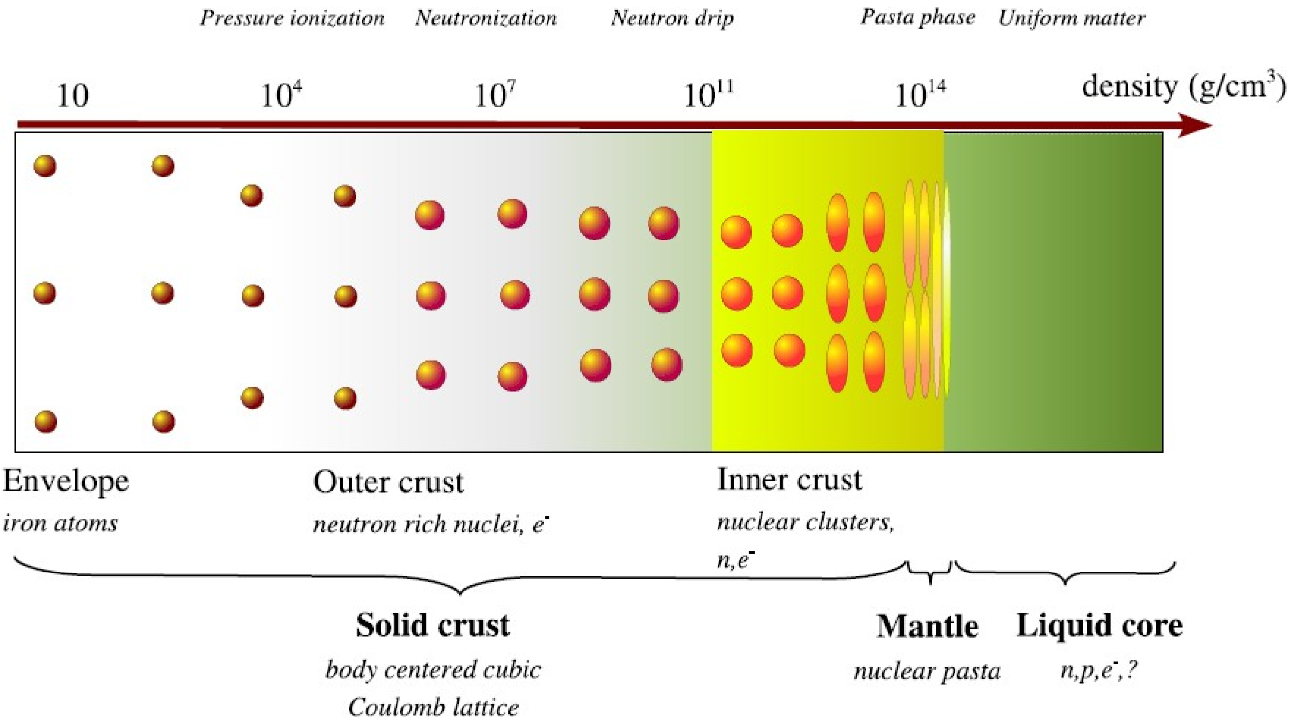

Figure 1.4: A schematic representation of the the different phases of nuclear matter within a neutron star, starting with the outermost layers on the left.

tween the radius and tidal deformability in low-mass neutron star [FP20], and the value of the second Love number, k_2 [PF19; PCS20]. Therefore it is crucial to have a reliable model of the crust of a neutron star, to achieve accurate descriptions of these phenomena.

In the simple case of a cold non-accreting neutron star, the crust can be separated into the *inner* and *outer* parts. From the earliest models [BPS71] to more modern ones [PGC11; CF16], it has been predicted that the outer crust has a crystalline structure of neutron-rich nuclei surrounded by a gas of free ultra-relativistic electrons [BPS71; Pas20; Fan20]. The inner crust begins above baryonic densities of $n_b \approx 10^{11}$ g cm^{-3}. Here, neutrons are no longer confined to bound states in finite nuclei, but they begin to *drip* out of the nuclei, forming a gas [NV73; Cha15; Pas20] which surrounds these nuclear clusters.

The quest to find the EoS that best describes the properties of neutron stars [CH08] is one of the major challenges in nuclear physics. Neutron stars are extremely compact objects, and so the density and pressure through their interior spans several orders of magnitude, and consequently it is important to use a theoretical model that can accurately describe such a large density range. Without a reliable EoS model, one cannot safely make predictions about global properties of a neutron star, such as its maximum mass, or the radius at a given mass.

The tool of choice to describe both finite nuclei and neutron stars is the nuclear energy density functional (NEDF) [RB04]. By carefully adjusting the parameters of the functional [GCP09b], it is possible to obtain a *unified* EoS [Sha15; Pea18] that can describe the entire neutron star, from the low-density outer regions to the core. Thanks to the latest advances both in the way one observes them [GAO12] and the technique used [Abb17], it is possible to provide additional constraints to the EoS [Mos18; BC18]. By combining those with more traditional constraints based on heavy-ion collision experiments [SG86; DLL02], it is possible to obtain interesting information about the properties of nuclear matter at high densities. Using all this information together with the most recent measurements of finite nuclei [Ste08], it is possible to construct accurate models to describe the physics of such massive objects.

The crust of a neutron star, while not comprising a large portion of the star's mass, nevertheless represents an important component of the EoS that is not yet precisely determined. The goal of this thesis is to make improvements to current nuclear models used in calculations of the EoS of neutron stars, in order to improve our understanding of the crust. In particular, I have investigated four key questions during my PhD thesis:

1. How does the *semiclassical* extended Thomas–Fermi + Strutinsky integral (ETFSI) approach compare with the Hartree–Fock–Bogoliubov (HFB) method when used to describe the inner crust?
2. In such semiclassical methods, the pairing correlations are typically ignored. What is the role of neutron and proton superfluidity in the composition of the crust?
3. How do the properties of the NEDF used in the ETFSI method affect the results for the inner crust?
4. When using a nuclear mass model to describe the composition of the outer crust, can we use machine learning techniques to provide more reliable extrapolations?

In Chapter 2, we outline the approximations made in order to model the inner crust, and detail the various contributions to the total energy of the system. In Chapter 3, we describe the two theoretical methods used to perform calculations for the inner crust, *ETFSI* and *HFB*, and compare in general the results each one produces. In Chapter 4, we introduce a method to include neutron pairing within the ETFSI method, and again compare with HFB. In Chapter 5, we employ a number of different Skyrme models, using the ETFSI+pairing method developed in Chapter 4, and investigate how their infinite nuclear matter properties influence their predictions of the inner crust's composition. In Chapter 6, we briefly overview how the outer crust is modelled, and present a new way of improving the performance of nuclear mass models in regions where there is no experimental data. Finally, in Chapter 7 we present our conclusions, and provide an outlook for future work for the modelling of neutron star crusts.

Chapter 2

The inner crust

Since the pioneering work of Negele and Vautherin [NV73], many theoretical models have been developed to study the properties of the inner crust. The presence of a neutron gas dramatically changes the properties of the clusters [Avo07], in contrast to the outer crust, whose nuclei are isolated. Consequently, determining the composition of the inner crust requires a simultaneous treatment of the clusters and the neutron gas. Ideally one should use band theory, as typically used in solid state physics, to discuss the properties of a crystal with delocalised electrons [Cha07; Cha12].

To simplify this task, it is customary to adopt the Wigner–Seitz (WS) approximation [WS33], in which the inner crust is decomposed into independent spheres with a radius R_{WS}, centered around each cluster, named *Wigner–Seitz cells*. It is assumed that there is no interaction between the cells. We refer to Ref. [Cha07] for a detailed discussion on the validity of such an approximation. Each cell is at β-equilibrium, with a certain number of protons, Z, and the same number of electrons (under the condition of charge-neutrality) spread through the cell. Using this approximation, the values of Z (the *chemical composition*) and R_{WS} can be determined at a given baryonic density, n_b, by minimising the total energy per particle, e, of the cell [Pea12]. This then yields the total particle number A, and the proton fraction $Y_p = Z/A$, a quantity of astrophysical importance. This procedure is valid only in the zero-temperature limit, which is applicable to the case of a non-accreting neutron star (NS). To consider the effects of finite-temperature in the inner crust, one should minimise the Helmholtz or Gibbs free energy, as done in Refs. [Ons08; GR15; Bur15].

Since the density of electrons in the crust is essentially uniform [WI03], it is possible to calculate their contribution to e analytically [CH08]. The nuclear contribution is more complex and requires the use of a model. In the literature, several models are used to determine the nuclear binding energy of the system, such as the compressible liquid drop model [DH00], semiclassical models using the Thomas–Fermi approximation [OY94; OPP97; Ons08; Pea12; MU15; Sha15; LH17], or the Hartree–Fock(–Bogoliubov) equations [NV73; GMS11].

Ideally, to model the EoS of a NS in a unified way, one should use the same model for all of its layers. The ideal choice is a fully microscopic method based on solving the Hartree–Fock–Bogoliubov equations [PBL11; GMS11; Pas17], using an effective nucleon-nucleon interaction [Sky56; RB04] adjusted to reproduce selected nuclear observables [Kor14]. One typically uses Dirichlet–Neumann boundary conditions [BST06; MVS08; Pas17] in solving the HFB equations. However, this causes a discretisation of the neutron continuum states, leading to spurious shell effects. New methods to overcome such a problem have been suggested [Cha12; Jin17], but no systematic calculations of the WS cells have been yet been performed.

To avoid this difficulty, several authors have opted to instead use the extended Thomas–Fermi method [OPP97; MU15; Mon20]. Due to its semiclassical nature, the ETF method is not affected by the spurious shell effects of the neutron gas encountered in the standard HFB approach. In Ref. [Ons08], the ETF method was extended to use the Strutinsky integral (SI) correction to recover the important shell effects for the protons in the clusters. This method, named ETFSI, calculates the nuclear energy contribution using parameterised nuclear density profiles, while still using the same energy density functional to generate the fields as in the HFB method. In Ref. [Pea15], the ETFSI method was further developed to take into account the effects of proton pairing correlations. However, there has so far not been a direct and systematic comparison of the ETFSI and HFB methods in the inner crust.

2.1 The Wigner–Seitz approximation

In the Wigner–Seitz (WS) approximation, we divide the periodic body-centred-cubic (BCC) lattice of nuclei in the inner crust into spherical charge-neutral non-interacting WS cells, shown schematically in Fig 2.1. The radius of each cell is such that the total number of baryons in each cell divided by the cell volume is equal to the baryonic density n_b. Therefore, there is a small overlap between cells. For a given n_b, all cells are assumed identical. Each contains a nuclear cluster at its center surrounded by a gas of superfluid neutrons, and also contains a near-homogeneous ultra-relativistic electron gas.

The radius of a cell R_{WS} is defined as half of the distance between neighboring clusters. Under the condition of charge neutrality, the number of protons Z in the WS cell must equal the number of electrons. For given values of n_b and R_{WS}, the total number of particles A is fixed by the relation

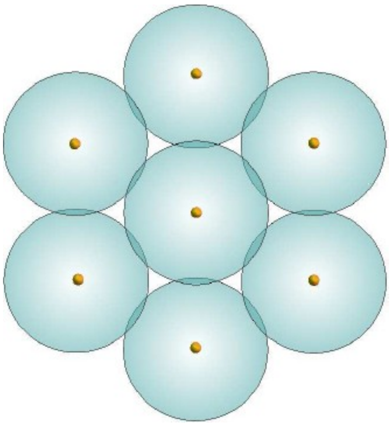

Figure 2.1: A schematic representation of the Wigner–Seitz approximation for a hexagonal lattice. Figure taken from Ref. [CH08].

$$A = n_b \frac{4\pi}{3} R_{\rm WS}^3. \tag{2.1}$$

Consequently, a WS cell is uniquely defined by the parameters $\{n_b, Z, R_{\rm WS}\}$. At zero temperature, the total energy per particle of the system is given by

$$e = e_{\rm Sky} + e_e - Y_p Q_{n,\beta}, \tag{2.2}$$

where $e_{\rm Sky}$ is the contribution arising from the baryons interacting via the strong force and from the Coulomb interaction between protons, while e_e is sum of the kinetic and potential energies of ultra-relativistic electrons [ST08] and the proton-electron interaction [GMS11]. The last term accounts for the mass difference between neutrons and protons, $Q_{n,\beta} = 0.782$ MeV. $Y_p = Z/A$ is the proton fraction of the cell.

The terms related to electrons (e_e) and to the Coulomb component of $e_{\rm Sky}$ are treated on equal footing for the HFB and ETFSI methods. We follow closely the approach of Ref. [Pea12], and provide the relevant expressions in the following sections.

2.2 Nuclear contribution

The energy contribution per particle for an effective interaction [Sky56] is expressed as functional of local densities[1]

$$e_{\rm Sky} = \frac{1}{A} \int \mathcal{E}_{\rm Sky}\left(\rho_q(\vec{r}), \tau_q(\vec{r}), \vec{J}(\vec{r})\right) d\vec{r}, \tag{2.3}$$

---

[1] In this work, we only consider time-even systems.

where $q = n, p$ stands for the nuclear charge. Considering only time-reversal invariant systems, the Skyrme functional depends only on a linear combination of the matter densities $\rho_q(r)$, kinetic densities $\tau_q(r)$, the spin current densities $\vec{J}(r)$ and their derivatives [Per04]. The procedure used to calculate the local densities differs in the HFB and semiclassical methods, and it is outlined in the Sections 3.1 and 3.2. Other authors have opted to use a finite-range Gogny interaction in place of a Skyrme interaction to model the inner crust [Mon20]. However, at present, Gogny interactions are not suitable for calculations of an entire NS, since their EoS are not able to predict the existence of the most massive neutron stars [SR14].

The standard Skyrme energy density functional (EDF) is given by:

$$\begin{aligned}\mathcal{E}_{\text{Sky}} = {} & \frac{\hbar^2}{2m}(\tau_n + \tau_p) \\ & + \frac{1}{4}t_0\left[(2+x_0)\rho^2 - (2x_0+1)(\rho_n^2+\rho_p^2)\right] \\ & + \frac{1}{24}t_3\rho^\sigma\left[(2+x_3)\rho^2 - (2x_3+1)(\rho_n^2+\rho_p^2)\right] \\ & + \frac{1}{8}[t_1(2+x_1)+t_2(2+x_2)]\rho\tau \\ & + \frac{1}{8}[t_2(2x_2+1)-t_1(2x_1+1)](\rho_n\tau_n+\rho_p\tau_p) \\ & + \frac{1}{32}[3t_1(2+x_1)-t_2(2+x_2)](\nabla\rho)^2 \\ & - \frac{1}{32}[3t_1(2x_1+1)+t_2(2x_2+1)]\left[(\nabla\rho_n)^2+(\nabla\rho_p)^2\right] \\ & + \frac{1}{2}W_0\left[\vec{J}\cdot\nabla\rho + \vec{J}_n\cdot\nabla\rho_n + \vec{J}_p\cdot\nabla\rho_p\right],\end{aligned} \tag{2.4}$$

where ρ is the total density $\rho_n + \rho_p$, and $t_{0-3}, x_{0-3}, \sigma, W_0$ are parameters that are adjusted using some optimisation procedure [Kor14].

By performing the first functional derivative of $\mathcal{E}_{\text{Sky}}$ with respect to $\tau_q, \vec{J}_q, \rho_q$, one obtains the effective mass m_q^*, spin-orbit field $\vec{W}_q$, and central field U_q respectively. These fields are used in the HFB and ETFSI calculations, detailed in Chapter 3. The effective mass is given by

$$\frac{\hbar^2}{2m_q^*} = \frac{\hbar^2}{2m} + \frac{1}{8}[t_1(2+x_1)+t_2(2+x_2)]\rho + \frac{1}{8}[t_2(2x_2+1)-t_1(2x_1+1)]\rho_q. \tag{2.5}$$

The spin-orbit field is given by

$$\vec{W}_q = \frac{W_0}{2}\vec{\nabla}(\rho+\rho_q). \tag{2.6}$$

The central field is given by

$$\begin{aligned}
U_q = t_0 &\left[\left(1+\frac{x_0}{2}\right)\rho - \left(x_0+\frac{1}{2}\right)\rho_q\right] \\
&+ \frac{t_1}{4}\left[\left(1+\frac{x_1}{2}\right)\left(\tau - \frac{3}{2}\Delta\rho\right) - \left(x_1+\frac{1}{2}\right)\left(\tau_q - \frac{3}{2}\Delta\rho_q\right)\right] \\
&+ \frac{t_2}{4}\left[\left(1+\frac{x_2}{2}\right)\left(\tau + \frac{1}{2}\Delta\rho\right) + \left(x_2+\frac{1}{2}\right)\left(\tau_q + \frac{1}{2}\Delta\rho_q\right)\right] \\
&+ \frac{t_3}{12}\left[\left(1+\frac{x_3}{2}\right)(2+\sigma)\rho^{\sigma+1} - \left(x_3+\frac{1}{2}\right)\left(\sigma\rho^{\sigma-1}\sum_{q'}\rho_{q'}^2 + 2\rho^\sigma\rho_q\right)\right] \\
&- \frac{W_0}{2}\left(\nabla\vec{J} + \nabla\vec{J}_q\right) \\
&+ \delta_{q,p}\left(V_{\text{Coul}} + V_{\text{Coul,pe}}\right),
\end{aligned} \tag{2.7}$$

where the Coulomb potential V_{Coul} from the interaction of protons is given by

$$V_{\text{Coul}}(r) = \frac{e^2}{2}\int_0^{R_{\text{WS}}} d^3r' \frac{\rho_p(r')}{|r-r'|} - e^2\left(\frac{3}{\pi}\right)^{1/3}\rho_p^{1/3}(r), \tag{2.8}$$

and the potential arising from the proton-electron interaction $V_{\text{Coul,pe}}$ is detailed in Sec. 2.3. The second term of Eq. 2.8, the exchange term $V_{\text{Coul,exc}}$, has been treated with the Slater approximation, and the first (direct) term is treated as follows:

$$V_{\text{Coul,dir}} = 4\pi e^2\left[\frac{1}{r}\int_0^r dr'\rho_p(r')r'^2 - \int_0^r dr'\rho_p(r')r' + \int_0^{R_{\text{WS}}} dr'\rho_p(r')r'\right]. \tag{2.9}$$

The energy density for the proton-proton Coulomb interaction is then given by

$$\mathcal{E}_{\text{Coul}} = \frac{\rho_p V_{\text{Coul,dir}}}{2} + \frac{3\rho_p V_{\text{Coul,exc}}}{4}. \tag{2.10}$$

Eqs. 2.4 to 2.7 contain extra terms for the BSk family of forces (BSk18 [CGP09] and newer), details of which are given in Appendix A. For BSk15 [GP08] and newer, the Coulomb exchange terms are set to 0, and in Eqs. 2.8 and 2.9 the proton densities are replaced with the charge density.

2.3 Electronic contribution

It is generally assumed that the electron density ρ_e in the WS cell is constant. Martin and Urban [MU15; Mar16] investigated the possibility of a non-uniform electron gas, by solving the

Poison equation for the electric charges in the WS cell, but they found no significant effect on the results. We can therefore safely define a constant ρ_e as

$$\rho_e = \frac{3Z}{4\pi R_{\mathrm{WS}}^3}. \tag{2.11}$$

There are three energy components to consider: the electron kinetic energy, the electron-electron potential energy, and the proton-electron potential energy. The total kinetic energy for the relativistic electrons in the WS cell is given by [Sal61]

$$E_{e,\mathrm{kin}} = Zm_e c^2 \left(\frac{3}{8x^3} \left[x(1+2x^2)\sqrt{1+x^2} - \sinh^{-1} x \right] - 1 \right), \tag{2.12}$$

where m_e is the electron mass, and the relativistic parameter x is

$$x = \frac{\hbar c k_{F,e}}{m_e c^2}, \tag{2.13}$$

where the electron Fermi momentum $k_{F,e} = (3\pi^2 \rho_e)^{1/3}$. The total potential energy for the electrons is given by [Sal61]

$$E_{ee,\mathrm{pot}} = \frac{3Z^2 e^2}{5R_{\mathrm{WS}}} \left[1 - \frac{5}{4} \left(\frac{3}{2\pi Z} \right)^{2/3} \Phi(x) \right], \tag{2.14}$$

where the function $\Phi(x)$ is given by

$$\Phi(x) = -\frac{1}{2x^4} \left[3x^2 + x^4 - 6x\sqrt{1+x^2} \sinh^{-1} x + 3 \left(\sinh^{-1} x \right)^2 \right]. \tag{2.15}$$

Finally, the total proton-electron potential energy is [GMS11]

$$E_{pe,\mathrm{pot}} = -\frac{3Z^2 e^2}{2R_{\mathrm{WS}}} + \frac{Ze^2}{2R_{\mathrm{WS}}^3} \int_0^{R_{\mathrm{WS}}} \rho_p r^2 \cdot 4\pi r^2 dr. \tag{2.16}$$

The corresponding proton-electron potential, included in the central potential U_q in Eq. 2.7, is [GMS11]

$$V_{\mathrm{Coul,pe}}(r) = \frac{Ze^2}{2R_{\mathrm{WS}}} \left[\left(\frac{r}{R_{\mathrm{WS}}} \right)^2 - 3 \right]. \tag{2.17}$$

Chapter 3

Comparison between the ETF and HFB methods

Within the NEDF framework, one should calculate the nuclear contribution to the total energy of the WS cell using the Hartree–Fock–Bogoliubov equations [RS80], since they provide a fully quantum mechanical description of the system without making an artificial distinction between bound and unbound neutrons. The downsides of the HFB method are its computational cost and the possible numerical inaccuracies related to the boundary conditions adopted in the calculation [BST06; MVS08; PBL11]. We refer to Ref. [Pas17] for a more detailed discussion. More recently, the HFB method has been used to investigate heating of the crust [Fan18] and the crust-core transition [Sch19], though these are not systematic studies of the crust.

To overcome the numerical difficulties that arise in the HFB method, but also to reduce the computational cost, several authors have adopted semiclassical methods based on the extended Thomas–Fermi approximation [BJC76]. To account for nuclear shell structure, an energy correction is added using the Strutinsky integral (SI) method [Pea12]. Combined, these are named the ETFSI method.

The results obtained using the two methods seem to qualitatively disagree. Using HFB, one typically observes clusters with a variety of different Z through the crust [GMS11; Pas17]. On the other hand, ETFSI points towards an inner crust comprising clusters with only $Z = 40$, both with Skyrme forces [Pea12; Pea15; Pea18] and with finite-range Gogny forces [Mon20]. The main reason for this disagreement is probably related to the properties of the functional used to perform the calculations.

In this chapter, we outline and then directly compare the HFB and ETFSI approach, in particular the densities, fields, and total energy predictions for each method.

3.1 The Hartree–Fock–Bogoliubov method

In the HFB approach, the densities (and thus the fields) are calculated directly using the quasi-particle wave-functions, which are the solutions of the HFB equations [RS80]:

$$\sum_{n'}(h^q_{n'nlj} - \varepsilon_{F,q})U^{iq}_{n'lj} + \sum_{n'} \Delta^q_{nn'lj} V^{iq}_{n'lj} = E^q_{ilj} U^{iq}_{nlj} \tag{3.1a}$$

$$\sum_{n'} \Delta^q_{nn'lj} U^{iq}_{n'lj} - \sum_{n'}(h^q_{n'nlj} - \varepsilon_{F,q})V^{iq}_{n'lj} = E^q_{ilj} V^{iq}_{nlj} \tag{3.1b}$$

where $\varepsilon_{F,q}$ is the Fermi energy. We used the standard notation nlj for the spherical single-particle states with radial quantum number n, orbital angular momentum l and total angular momentum j. V^{iq}_{nlj} and U^{iq}_{nlj} are the Bogoliubov amplitudes for the i-th quasi-particle with energy E^q_{ilj}. The single-particle Hamiltonian h is built from the Skyrme functional, while $\Delta^q_{nn'lj}$ are the matrix elements of the pairing gap obtained from a contact pairing interaction. In the case of vanishing pairing, these equations reduce to the Hartree–Fock (HF) one. For more details on the numerical methods used to solve these equations we refer to references [Pas17; PBL11; Pas12; Pas13]. The most relevant point for the following discussion is the choice of the boundary conditions used to solve Eqs. 3.1a and 3.1b. In this thesis, we use the Dirichlet–Neumann mixed boundary conditions: (i) even-parity wave-functions vanish at $r = R_{\text{WS}}$; (ii) the first derivative of odd-parity wave-functions vanishes at $r = R_{\text{WS}}$. We call them Boundary Conditions Even (BCE), in contrast to the boundary conditions odd (BCO) where the two parity states are treated in the opposite way. We have checked that this particular choice does not affect the final results. See also Ref. [Pas17] for more details.

3.2 The ETFSI method

In this section, we briefly describe the extended Thomas–Fermi + Strutinsky integral method, as developed in references [GV79; BB02; Ons08; Pea12] for a system with no pairing. Within the semiclassical approach, the neutron and proton densities are parameterised. This differs from the HFB method, in which all densities are calculating using the quasi-particle wave-functions. Assuming no proton gas, we use a generalized Fermi–Dirac distribution of the form

$$\rho_q(r) = \frac{\rho_q^{\mathrm{liq}} - \delta_{q,n}\rho^{\mathrm{gas}}}{1 + \exp\left(\frac{r - r_q}{a_q}\right)} + \delta_{q,n}\rho^{\mathrm{gas}}. \tag{3.2}$$

ρ_q^{liq} are the densities of the neutrons and protons at the center of the WS cell, $r = 0$, while ρ^{gas} is the density of neutrons at the edge, $r = R_{\mathrm{WS}}$. r_q are the cluster radii of the neutrons and protons, and a_q are the diffusivities of the cluster surface. These seven adjustable parameters are determined by the minimization of the energy per particle, given in Eq. 2.2, under the constraints of charge neutrality and β-equilibrium. See Sec. 3.2.1 for more details.

The authors of references [Ons08; Pea12; Pea18] have introduced an additional damping factor in Eq. 3.2. Although such a term may be useful for avoiding convergence problems at high n_b, it has a small impact on the energy per particle of the system, and for the following analysis we can safely proceed without it. In Ref. [MU15] the authors introduced an exponent for the denominator in Eq. 3.2, but they concluded that the results are largely unchanged, so we do not consider such a parameterisation.

The kinetic and spin-current densities are expressed as a function of the matter density ρ_q and its derivatives via the Wigner–Kirkwood expansion [RS80]. In the present work, we use the full expansion, up to 4th-order in gradients, employing the explicit expressions for the 4th-order density contributions as given in the appendix of Ref. [BB02]. This differs from the approach of Ref. [Pea12], explained in Section II of this reference. Below we present all terms up to 2nd-order in gradients, giving the 4th-order terms in Appendix B.

In the *Thomas-Fermi* approximation, i.e., 0th-order in gradients, the kinetic energy density $\tau_q^{(\mathrm{TF})}$ is simply given by

$$\tau_q^{(\mathrm{TF})}[\rho_q] = \frac{3}{5}(3\pi^2)^{2/3}\rho_q^{5/3}. \tag{3.3}$$

There is no contribution to the spin current density $\vec{J}$ at 0th-order.

The extended Thomas-Fermi approximation contains contributions to $\vec{J}$, and extra contributions to τ_q. At 2nd-order, the kinetic energy density contribution is

$$\begin{aligned}\tau_q^{(2)}[\rho_q] = & \frac{1}{36}\frac{(\vec{\nabla}\rho_q)^2}{\rho_q} + \frac{1}{3}\Delta\rho_q \\ & + \frac{1}{6}\frac{\vec{\nabla}\rho_q \cdot \vec{\nabla} f_q}{f_q} + \frac{1}{6}\rho_q\frac{\Delta f_q}{f_q} - \frac{1}{12}\rho_q\left(\frac{\vec{\nabla} f_q}{f_q}\right)^2 \\ & + \frac{1}{2}\left(\frac{2m}{\hbar^2}\right)^2 \rho_q \left(\frac{\vec{W}_q}{f_q}\right)^2 ,\end{aligned} \tag{3.4}$$

where f_q is the effective mass ratio m/m_q^*. The spin current density contribution at 2nd-order is

$$\vec{J}_q^{(2)} = -\frac{2m}{\hbar^2}\frac{\rho_q}{f_q}\vec{W}_q. \tag{3.5}$$

We have checked that all contributions to τ_q and $\vec{J}_q$ are calculated correctly by performing benchmarks (see Appendix C) against the calculations of Bartel and Bencheikh [BB02]. Our calculations are in exact agreement, proving the quality of our implementation.

Under the ETF approximation, shell effects are not accounted for. Consequently, the authors of Ref. [Ons08] suggested including (at least for protons) a perturbative contribution to the total energy using the Strutinsky integral (SI) theorem, without acting on the densities or fields. For the sake of completeness we implemented exactly the same method. For a system at $T = 0$ with no pairing between protons, the total energy correction is given by

$$E_p^{\mathrm{SI}} = \sum_i^{\mathrm{occ.}} n_i \epsilon_{i,p} - \int_0^{R_{\mathrm{WS}}} \left(\frac{\hbar^2}{2M_p^*}\tau_p + \rho_p U_p + \vec{J}_p \cdot \vec{W}_p\right) \cdot 4\pi r^2 dr, \tag{3.6}$$

where the sum goes over all *occupied* single-particle proton states i, n_i are the occupancies ($= 0$ or 1) for each state, and $\epsilon_{i,p}$ are corresponding single-particle energies, obtained by solving the single-particle Schrödinger equation:

$$\left\{-\vec{\nabla}\frac{\hbar^2}{2M_p^*(\vec{r})} \cdot \vec{\nabla} + U_p(\vec{r}) - i\vec{W}_p(\vec{r}) \cdot \vec{\nabla} \times \vec{\sigma}\right\} \phi_{i,p} = \epsilon_{i,p}\phi_{i,p}. \tag{3.7}$$

We made comparisons with ETFSI results from the literature, to check that our implementation gives consistent results. In Fig. 3.1, we show a comparison between the energy per particle e obtained from our work and from Pearson et al. [Pea12], for WS cells at the drip density $n_b = 0.00026346$ fm^{-3} using BSk19. The slight discrepancies are due to our slightly different choice of density profile, as explained in Sec. 3.2, given that all other aspects of the

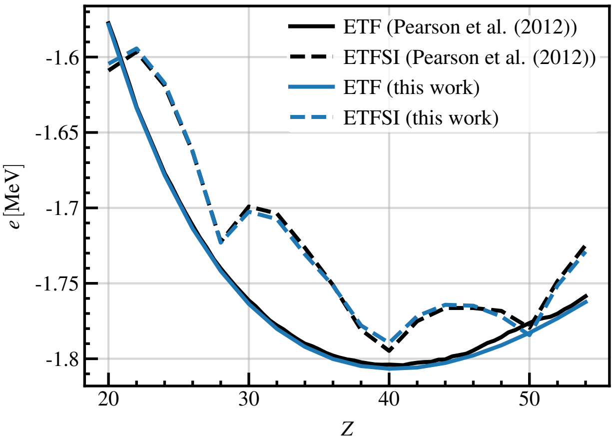

Figure 3.1: Comparison between the energy per particle e from our work and from the upper panel of Fig. 2 of Ref. [Pea12], for ETF only (solid lines), and for ETFSI (dashed lines). Calculations are for WS cells with $n_b = 0.00026346\ \text{fm}^{-3}$, using the BSk19 functional.

calculations are the same. These discrepancies are most pronounced at the drip density where the clusters are smallest. For larger n_b, the agreement is the same or better.

It is possible to extend the SI theorem to systems with proton pairing; this is outlined in Chapter 4.

3.2.1 Energy minimization with ETFSI

A key ingredient of the ETFSI calculation is the determination of the seven parameters of the density profiles, using a minimization procedure. For this case we have used the Python library SciPy [Sci20]. For a given n_b and Z, an initial guess is made for the number of neutrons, and the corresponding R_{WS} is calculated using Eq. 2.1. The parameters of the density profiles in Eq. 3.2 are varied to minimize the total energy of the WS cell (Eq. 2.2), which is calculated using a code [She21] written in Fortran 90. Two of the seven parameters can be expressed in terms of the others as follows:

$$\rho^{\text{gas}} = \frac{3\left(N - \mathcal{I}_n \rho_n^{\text{liq}}\right)}{4\pi R_{\text{WS}}^3} \cdot \left[1 - \frac{3\mathcal{I}_n}{4\pi R_{\text{WS}}^3}\right]^{-1}, \tag{3.8a}$$

$$\rho_p^{\text{liq}} = \frac{Z}{\mathcal{I}_p}, \tag{3.8b}$$

where $\mathcal{I}_q$ is given by

$$\mathcal{I}_q = \int_0^{R_{\mathrm{WS}}} \frac{4\pi r^2 dr}{1 + \exp\left\{\frac{r - r_q}{a_q}\right\}}. \tag{3.9}$$

This leaves only five free parameters in the minimisation.

After the profile parameters have been determined, the SI correction and proton pairing energy is added perturbatively, which is necessary to prevent anomalously large values for the SI correction [Pea12]. This energy minimization is systematically repeated with different neutron numbers to find the cell configuration with the minimum energy.

After repeating this process for every even value in $20 \leq Z \leq 60$, one finds the Z that yields the lowest energy per particle e; this is the optimum Z for a given n_b. We used this range of Z since it is the relevant range observed by previous authors; however, we always check that the global minima fall within this range.

Attempts to use the full 4th-order expressions for densities, along with the profiles using an extra damping factor as used in [Ons08; Pea12; Pea18], made the minimization much more difficult. Even without the damping factor, at $n_b \approx 0.05$ fm^{-3} and above, our minimization procedure begins to fail increasingly often. This is the same difficulty reported by the authors of Ref. [Pea12]. Furthermore, the presence of non-spherical clusters is expected above $n_b \approx 0.05$ fm^{-3} [PCP20]. Since the goal of this thesis is not to provide a complete EoS for calculations of an entire NS, we have limited our investigation to the range of baryonic densities 0.00025 fm^{-3} $\leq n_b \leq 0.048$ fm^{-3}. In our formalism, spherical symmetry is imposed, which is likely a poor assumption at higher n_b [PCP20].

3.3 Choice of functionals

Before a more detailed analysis on the results obtained with HFB and ETFSI, we briefly discuss the choice of the Skyrme functionals used in this chapter. In Fig. 3.2, we show the energy per particle e curves for pure neutron matter (PNM) as a function of the density of the system for the three functionals: SLy4 [Cha98], BSk21 [Pea12] and BSk24 [GCP13].

Their parameters were all adjusted for the functionals to be applicable to both finite nuclei and higher density neutron star matter. They have therefore been used frequently in the modelling of an entire neutron star. On the same figure we also show the *APR* EoS calculated using ab-initio methods by Akmal, Pandharipande, and Ravenhall in Ref. [WFF88; Wir93], and the *LS2* EoS calculated by Li and Schulze in Ref. [LS08]. Both BSk21 and BSk24 have been fit on the LS2 EoS, while SLy4 has been adjusted using APR.

In Table 3.1, we give some properties in infinite nuclear matter (INM) for each functional.

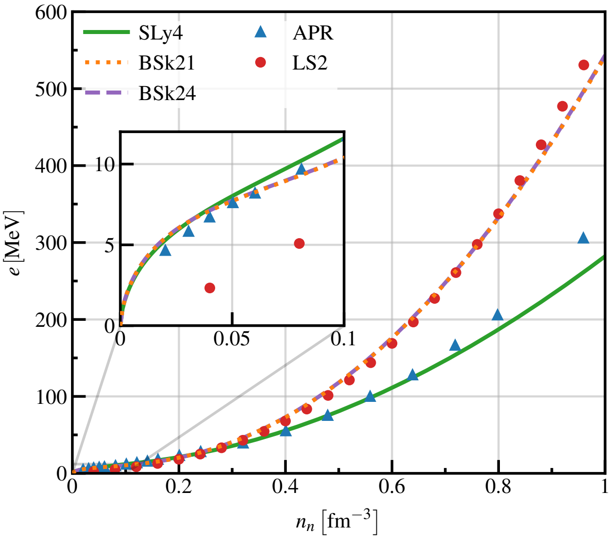

Figure 3.2: Energy per particle e in PNM for the three functionals used. The EoS calculated in references [WFF88; Wir93] (APR), and the one calculated in Ref. [LS08] (LS2) are also shown.

Functional	n_0 [fm^{-3}]	E_0 [MeV]	J [MeV]	L [MeV]	m^*/m
SLy4	0.160	-15.97	32.00	45.94	0.69
BSk21	0.158	-16.05	30.00	46.56	0.80
BSk24	0.158	-16.05	30.00	46.40	0.80

Table 3.1: Selected INM properties for the functionals used to compare ETFSI and HFB.

Each functional has very similar properties, having the canonical values for nuclear saturation density $n_0 \approx 0.16$ fm^{-3} and for the energy per particle at saturation $E_0 \approx 16$ MeV. As seen in the inset of Fig. 4.5, all three functionals have very similar PNM EoS at the low densities relevant for the inner crust. For this initial investigation, we do not seek to understand the effect of using functionals with very different properties. There is still no agreement in the literature on the exact form of the PNM EoS or on the values of the various INM properties; see for example the discussion in Ref. [Dut12]. These aspects are analysed in detail in Chapter 5.

3.4 Comparison between ETFSI and HFB

We now examine the quality of our semiclassical method by comparing the densities and fields with those obtained from a fully self-consistent HFB calculation. In Fig. 3.3, we illustrate the density profiles for a WS cell with $n_b = 0.02$ fm^{-3}, $Z = 40$ and $R_{\rm WS} = 24.0$ fm, obtained using the SLy4 functional [Cha98], by solving the HFB equations. In the same figure, we also illustrate the results obtained using ETFSI: the seven parameters characterizing the semiclassical matter densities (Eq. 3.2) were adjusted to reproduce the matter densities obtained from the HFB calculation.

We observe that the 4th-order expansion works nicely, and reproduces very well the neutron kinetic and spin-current densities, as shown in panel *a* of Fig. 3.3. The proton kinetic density presents a small bump around 7 fm, as seen in panel *b* of Fig. 3.3. Due to the large density gradient in the proton cluster surface compared to the neutron one, the 4th-order truncation is probably not fully satisfactory. The main consequence is the poor reproduction of the proton spin current density. This is not a major issue since the spin-orbit field is not too affected by such a difference.

From the densities, one obtains the corresponding fields [Per04]: the central potentials $U_q(r)$, the effective masses $\frac{\hbar^2}{2m_q^*(r)}$ and the spin-orbit fields $\vec{W}_q(r)$. They are shown in the lower panels of Fig. 3.3, together with the corresponding ones obtained solving the HF equations. In both neutron and proton cases the agreement is very good, thereby showing the validity of the semiclassical approximation in capturing the main features of the HFB calculation. The bump in the kinetic and spin current proton densities translates to an oscillation of the central proton potential at $r \approx 7$ fm, but the impact is small.

We now perform a systematic comparison between the ETFSI, HF (i.e., no pairing), and HFB methods, for various WS cells with baryonic densities in the range $0.0003\ \mathrm{fm}^{-3} < n_b < 0.024\ \mathrm{fm}^{-3}$. We use the SLy4 functional, and all cells have $Z = 50$ and a fixed cell radius $R_{\mathrm{WS}} = 60$ fm. No minimisation is carried out, as we only seek to compare the energy per particle e for a given cell with each method.

The left panel of Fig. 3.4 shows the difference in energy per particle Δe obtained between the ETFSI and HF methods, and between the ETFSI and HFB methods. At low n_b, Δe is as high as 0.09 MeV per particle, but then starts decreasing rapidly as n_b increases. This demonstrates that HF(B) is preferable near the drip density, where there is almost no neutron gas present. From $n_b = 0.001\ \mathrm{fm}^{-3}$ and above, the two curves show very different trends. ETFSI and HF agree to within about 0.02 MeV per particle for all densities, whereas for ETFSI-HFB the difference increases again as pairing switches on, reaching a maximum of ≈ 0.22 MeV per particle. At higher densities, when the pairing starts decreasing, Δe starts decreasing again. Except at very low densities, the discrepancy between the two methods is one order of magnitude worse than in the non-superfluid case.

In the right panel of Fig. 3.4, we give the pairing gap in PNM for the SLy4 functional, using the same pairing interaction (see Chapter 4 for details) as used in the HFB calculations. We observe a maximum at a similar density to where the ETFSI-HFB discrepancy is largest. This

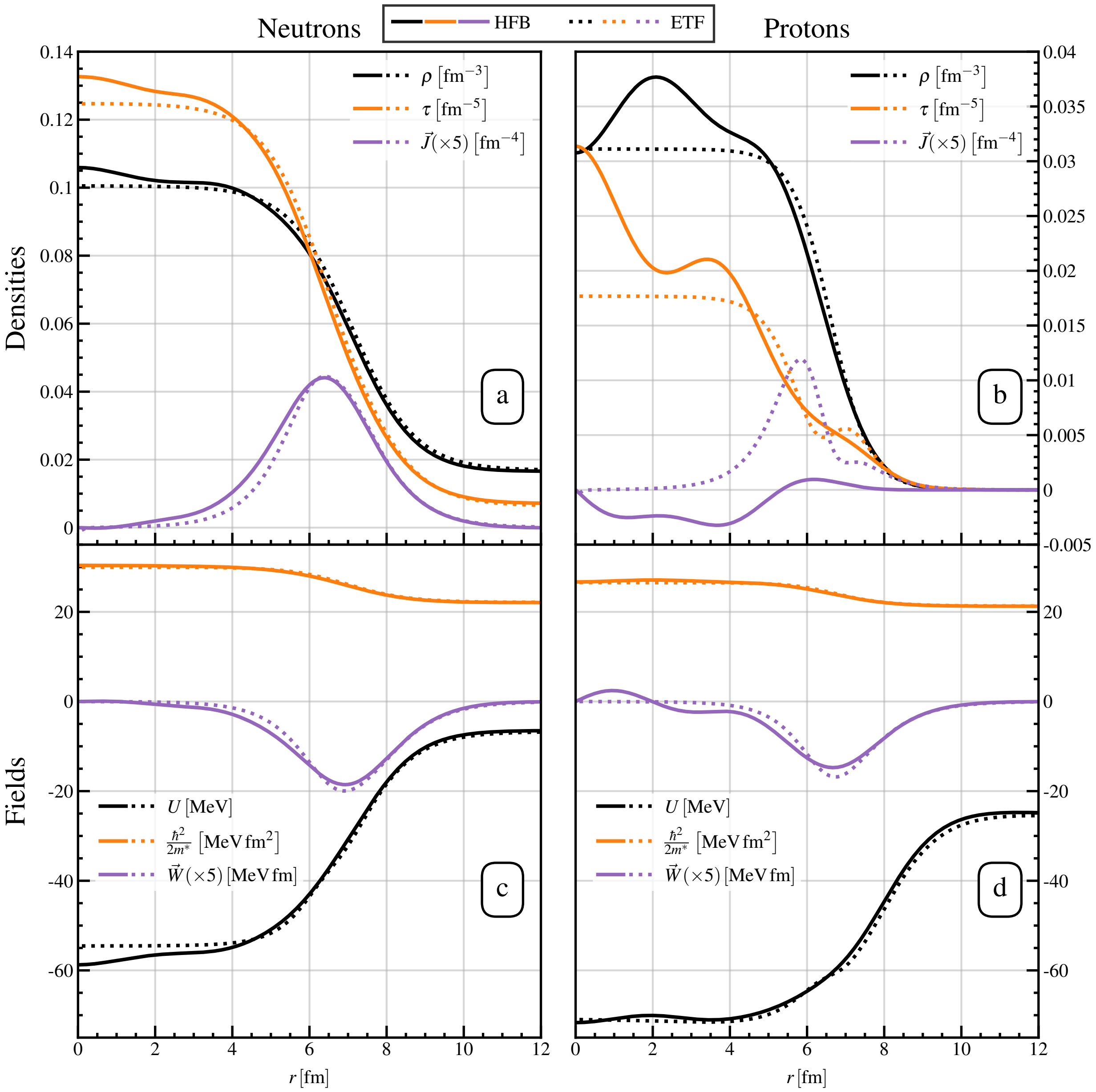

Figure 3.3: Densities (top row) and fields (bottom row), for neutrons (left column) and protons (right column), for a WS cell with $n_b = 0.02$ fm^{-3}, $Z = 40$ and $R_{\mathrm{WS}} = 24$ fm. Black lines show the matter densities and central potentials, orange lines show the kinetic densities and effective masses, and purple lines show the spin current densities $\vec{J}_q$ and spin-orbit fields $\vec{W}_q$. Solid lines show the HFB results, and dotted lines the ETFSI results; both use the SLy4 functional. Note the different scales used in panels a and b for the neutron and proton densities, and that $\vec{J}_q$ and $\vec{W}_q$ are multiplied by 5 to make them more visible.

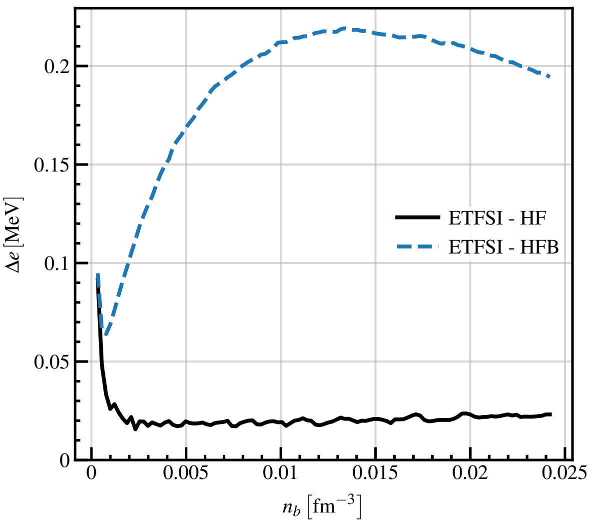

Figure 3.4: Left: the difference in energy per particle Δe obtained from the ETFSI and HF methods (solid line), and from the ETFSI and HFB methods (dashed line); all cells have $Z = 50$ and $R_{\rm WS} = 60$ fm. Right: the pairing gap in PNM at neutron density n_n for SLy4 with the Strong pairing interaction (see Chapter 4 for details).

clearly shows that neglecting pairing correlations for neutrons in the ETFSI approach leads to a large error, much larger than those arising from choice of boundary conditions and box-size effects as discussed in Ref. [SP20].

The implementation of pairing in the ETFSI method, in particular for neutrons, will be discussed in detail in Chapter 4.

Chapter 4

The role of pairing correlations

Within the literature, there is a wide consensus on the importance of pairing correlations within the inner crust of neutron stars [Bar97; DH03; BST06; GMS11; PBL11; SVL04; Cha12; MHF14; WP17; BK08]. In Chapter 3, we compared the structure of some WS cells, performing both ETFSI and HFB calculations using the same functionals. We observed an energy discrepancy far larger than the estimated error of the HFB method [Pas17], and we identified the cause as a lack of neutron pairing correlations [Pas13] in the ETFSI approach [Pea15]. In this chapter, we develop the ETFSI+pairing method for the inner crust, which for the first time takes into account the role of pairing for both protons and neutrons.

4.1 Proton pairing correlations

While pairing correlations are naturally included within the HFB equations (Eqs. 3.1a and 3.1b), the original ETFSI method [Ons08] is not capable of treating such correlations. As a consequence, in Ref. [Pea15] the authors have modified the ETFSI formalism to include the effects of proton pairing with the BCS approximation [RS80], but still with no explicit treatment of neutron pairing correlations.

We now briefly outline the combined Strutinsky integral and BCS formalism. When we include pairing in the BCS approximation, we have to both alter E_p^{SI} to account for different single-particle occupations, and we have to include the reduction in energy from proton pairing E_p^{pair}.

In Chapter 3 we gave the expression for the total Strutinsky integral energy correction E_p^{SI} without pairing (Eq. 3.6). E_p^{SI} is now given by

$$E_p^{\mathrm{SI}} = \sum_i^{\mathrm{all}} V_{i,p}^2 \epsilon_{i,p} - \int_0^{R_{\mathrm{WS}}} \left(\frac{\hbar^2}{2M_p^*}\tau_p + \rho_p U_p + \vec{J}_p \cdot \vec{W}_p \right) \cdot 4\pi r^2 dr, \tag{4.1}$$

where the sum now goes over *all* single-particle proton states i. $V_{i,p}^2$ are the single-particle occupation probabilities:

$$V_{i,p}^2 = \frac{1}{2}\left[1 - \frac{\epsilon_{i,p} - \mu_p}{E_{i,p}^{\mathrm{qp}}}\right]. \tag{4.2}$$

μ_p is the proton chemical potential, and $E_{i,p}^{\mathrm{qp}}$ are the quasi-particle energies for each state:

$$E_{i,p}^{\mathrm{qp}} = \sqrt{(\epsilon_{i,p} - \mu_p)^2 + \Delta_{i,p}^2}, \tag{4.3}$$

where $\Delta_{i,p}$ are the pairing gaps for each state, defined as

$$\Delta_{i,p} = \int_0^{R_{\mathrm{WS}}} \Delta_p(r) \phi_{i,p}^2(r) \cdot 4\pi r^2 dr. \tag{4.4}$$

$\Delta_p(r)$ is the pairing field and $\phi_{i,p}^2$ are the single-particle wave-functions appearing in Eq. 3.7. $\epsilon_{i,p}$, μ_p, and $\Delta_{i,p}$ are determined by solving the BCS equations:

$$Z = \sum_i^{\mathrm{all}} V_{i,p}^2, \qquad \text{number equation} \tag{4.5a}$$

$$\Delta_p(r) = \frac{1}{2} f_p(r) \widetilde{\rho}_p^{\mathrm{BCS}}(r), \qquad \text{gap equation} \tag{4.5b}$$

where f_p is the pairing strength (see Sec. 4.3) evaluated at a given BCS proton density ρ_p^{BCS}. The expressions for ρ_p^{BCS} and the anomalous density $\widetilde{\rho}_p^{\mathrm{BCS}}$ are

$$\rho_p^{\mathrm{BCS}} = \sum_i^{\mathrm{all}} (2j+1) V_{i,p}^2 \phi_{i,p}^2(r), \tag{4.6a}$$

$$\widetilde{\rho}_p^{\mathrm{BCS}} = \sum_i^{\mathrm{all}} (2j+1) U_{i,p} V_{i,p} \phi_{i,p}^2(r), \tag{4.6b}$$

where j is the total angular momentum of the i-th single-particle state, and $U_{i,p}^2 = 1 - V_{i,p}^2$.

Finally, from solving the BCS equations, we also obtain the proton pairing energy

$$E_p^{\mathrm{pair}} = \frac{1}{2} \int_0^{R_{\mathrm{WS}}} \Delta_p(r) \widetilde{\rho}_p^{\mathrm{BCS}}(r) \cdot 4\pi r^2 dr. \tag{4.7}$$

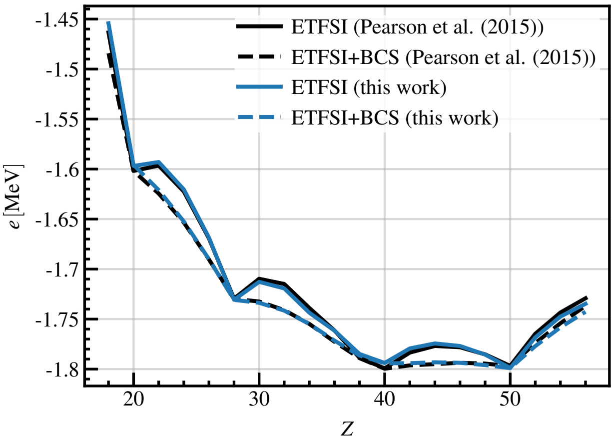

Figure 4.1: Comparison between the energy per particle e from our work and from the upper panel of Fig. 1 of Ref. [Pea15], for ETFSI only (solid lines), and for ETFSI+BCS (dashed lines). Calculations are for WS cells with $n_b = 0.00026$ fm^{-3}, using the BSk21 functional.

To verify our implementation of this ETFSI+BCS method, we made comparisons with the calculations of Pearson et al. [Pea15]. In Fig. 4.1, we overlay the energy per particle e obtained from our work with that from Pearson et al., for WS cells at the drip density $n_b = 0.00026$ fm^{-3} using BSk21. The slight discrepancies are the same as those seen and explained in the ETFSI benchmark that we made in Chapter 3. The fact that we obtain the same shift from ETFSI to ETFSI+BCS demonstrates our correct implementation of the BSk pairing protocol (detailed in Appendix A) and of the combined Strutinsky integral and BCS method.

4.2 Neutron pairing correlations

Since the neutrons in the inner crust form a gas, it is not possible to apply directly the same methodology without running into the same type of problems encountered with the HFB method, which are related to spurious shell effects in the neutron gas [MVS08]. In this work, we have developed an additional energy correction based on the local-density approximation (LDA). A similar approach was already proposed in Ref. [Bur15]. In the the weak-coupling limit, the correction to the energy per particle from superfluid neutrons is [PVB97]

$$e_{\text{cond}} = \int_0^{R_{\text{WS}}} -\frac{3\Delta_n^2(n_n(r))}{8\mu_n} n_n(r) \cdot 4\pi r^2 dr. \tag{4.8}$$

The chemical potential μ_n is approximated by the Fermi energy $\varepsilon_{\text{F}n} = k_{\text{F}n}^2 \hbar^2 / 2m_n^*$, where

$k_{\mathrm{F}n} = (3\pi^2 n_n)^{1/3}$. Δ_n is the local pairing gap as extracted from PNM calculations at a given neutron density n_n as discussed in Ref. [Pas08] and illustrated in Fig. 4.2. For the BSk forces, Δ_n has an analytical form, as explained in Appendix A. In the case of infinite nuclear matter, in which we can solve the BCS equations exactly, we have checked that the use of Eq. 4.8 leads to an error of the order of a few percent [PSD17]. It is therefore a reasonable approximation for treating neutron pairing in the WS cell, since at medium to high densities the effects of neutron pairing will occur predominantly in the neutron gas. We refer to Appendix D for a more detailed discussion. The energy correction in Eq. 4.8 can be easily implemented in the ETFSI formalism without a major increase in the computational cost.

4.3 Pairing interaction

The SLy4 functional was fit to doubly-magic nuclei; as a consequence, we are left with some freedom in choosing how to model pairing correlations. In this work, we use a simple density-dependent pairing interaction of the form [BE91]

$$v_q^{\mathrm{pair}}(\mathbf{r}_1, \mathbf{r}_2) = v_{0q}\left[1 - \eta\left(\frac{\rho_q(r)}{n_0}\right)^{\alpha}\right]\delta\left(\mathbf{r}_1 - \mathbf{r}_2\right). \tag{4.9}$$

We choose the parameters $\eta = 0.7$ and $\alpha = 0.45$. We assume that the pairing strength is the same for neutrons and protons and we fix the pairing strength v_{0q} to obtain a maximum pairing gap in PNM of ≈ 3 MeV, hereafter named *strong*, or a maximum of ≈ 1 MeV, hereafter named *weak*, as done in Ref. [GMS11]. These choices largely cover the available range of results concerning the density evolution of the pairing gap in infinite nuclear matter [Gan08]. To avoid the ultraviolet divergence of the interaction given in Eq. 4.9 [BY02], we adopt a smooth cut-off in quasi-particle space at $E_{ijl}^q \geq 20$ MeV that is defined by an Gaussian factor $\exp\left[\left(E_{ijl}^q - 20\right)/100\right]$. In Fig. 4.2, we report the density dependence of the pairing gap in PNM obtained by solving the BCS equations. The maxima of these pairing gaps are located at $n_n \approx 0.03$ fm^{-3} (SLy4), corresponding to a Fermi momentum of $k_{\mathrm{F}n} \approx 0.94$ fm^{-1}.

The pairing interactions for the BSk21 and BSk24 functionals [Cha10] have been adjusted to reproduce the $^1S_0$ pairing gaps in both symmetric nuclear matter and PNM, as obtained from Brueckner calculations using the Argonne $V18$ nucleon-nucleon potential [CLS06]. The implementation details are provided in Appendix A. The resulting pairing gap is also reported in Fig. 4.2 as a function of the neutron density. We observe that in this case, the pairing gap reaches a maximum of $\Delta_n \approx 2.5$ MeV around $n_n \approx 0.02$ fm^{-3}, corresponding to a Fermi

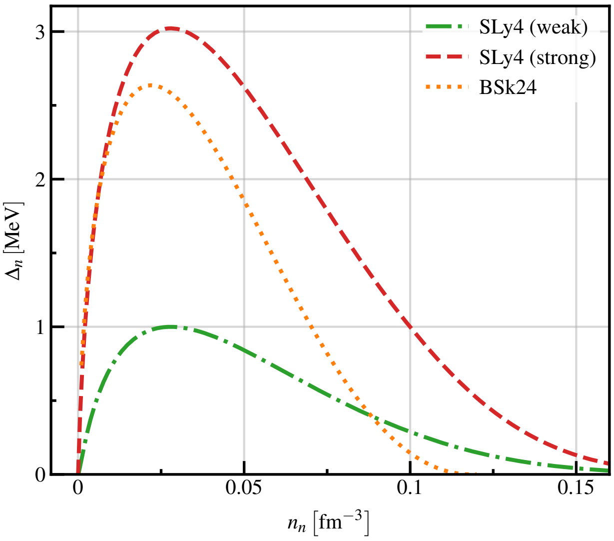

Figure 4.2: The pairing gap in PNM, as a function of density, for the two pairing strengths used with the SLy4 functional (green dash-dotted line shows weak, red dashed line shows strong), and for the BSk24 functional (orange dotted line).

momentum of $k_{\mathrm{F}n} \approx 0.87$ fm^{-1}.

For a given functional and pairing interaction, one would expect that any changes to the inner crust from including neutron pairing would be greatest at n_b near the value of n_n for which $\Delta_n(n_n)$ is at its greatest.

In Fig. 4.3 we illustrate the different contributions to the energy per particle e for various WS cells at fixed baryonic density $n_b = 0.02$ fm^{-3}, but for the cases of weak and strong pairing. The ETFSI+pairing results have been obtained using a complete minimization of the total energy of the WS cell using the SLy4 functional. In the upper-left panel we show the nuclear contribution, referring to the ETF energy including proton-proton Coulomb interaction. The higher e with stronger pairing simply reflects the larger neutron number obtained. The higher the proportion of neutrons in the system, the more neutron pairing can occur, lowering the total energy. When we include also the electron-electron and proton-electron interactions, as shown in the lower-left panel, we see almost no difference between the weak and strong pairing cases. For strong pairing, the increase in the nuclear energy is offset by a decrease in the energy contribution from the electrons, a result of the larger WS cell.

In the upper-right panel of Fig. 4.3, we see that the contribution to e from neutron pairing is almost flat with respect to Z, for weak and strong. Note that the weak case has been multiplied by 10 in this panel. From Fig. 4.2, where the PNM gap is about three times higher for the strong interaction at $n_b = 0.02$ fm^{-3}, and Eq. (4.8), showing the quadratic dependence of e_{cond}

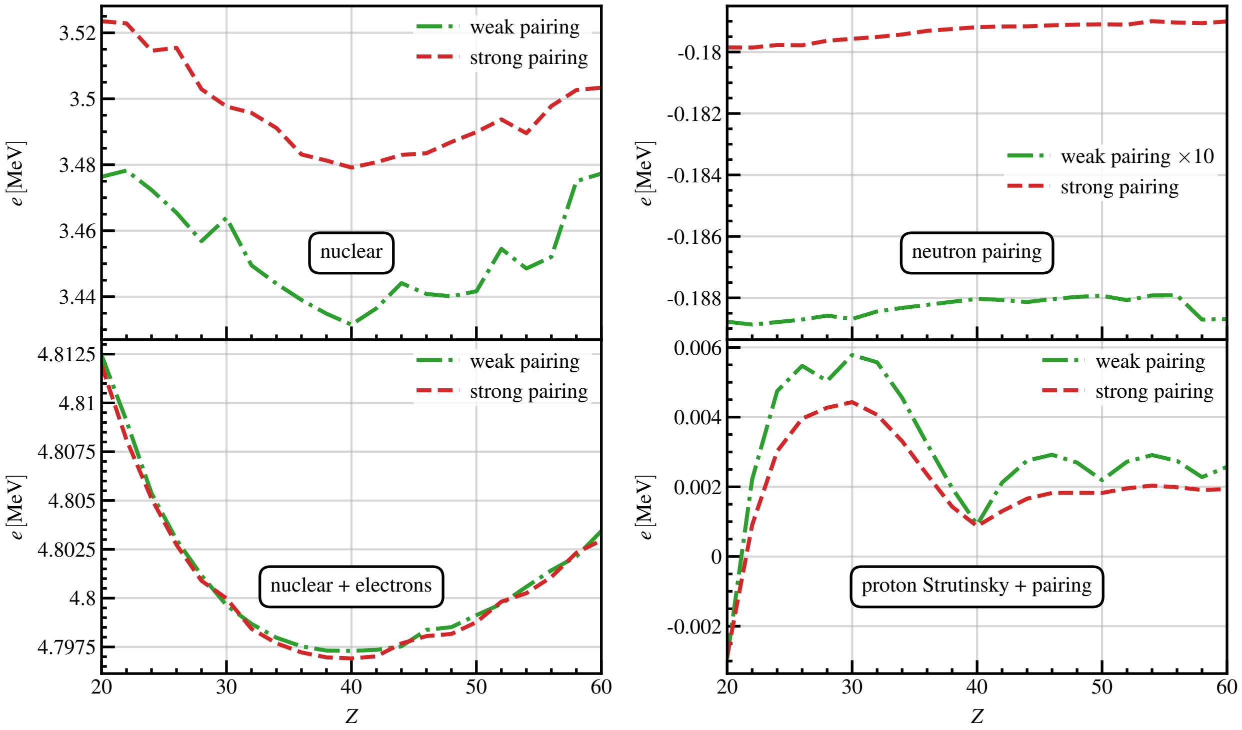

Figure 4.3: Individual contributions to energy per particle e for a WS cell with $n_b = 0.02$ fm^{-3}. Results are shown for the two pairing strengths used with the SLy4 functional (green dash-dotted line shows weak, red dashed line shows strong). The top left panel shows only $e_{\rm Sky}$, while the bottom left shows $e_{\rm Sky} + e_e$; see Eq. 2.2 and text for details. In the top right panel, which shows $e_{\rm cond}$ (Eq. 4.8), the weak result has been multiplied by 10 to make clear the variations for weak and strong on the same scale.

on the PNM gap, we see that the factor of nine increase in the neutron condensation energy was expected.

The energy per particle coming from the SI correction and proton pairing energy, as calculated in Ref. [Pea15], are shown in the lower-right panel of Fig. 4.3. The shell effects give rise to local minima at $Z = 20, 28, 40, 50, 58$ for both the weak and strong interactions. The effect of increasing the proton pairing strength is to partially smooth out these shell effects.

4.4 HFB vs. ETFSI+Pairing

In this section we compare the results obtained in WS cells from solving the HFB equations with those from the ETFSI method, with and without the additional correction for neutron pairing correlations.

In Fig. 4.4, we show the results obtained with ETFSI, ETFSI+pairing and HFB, for the

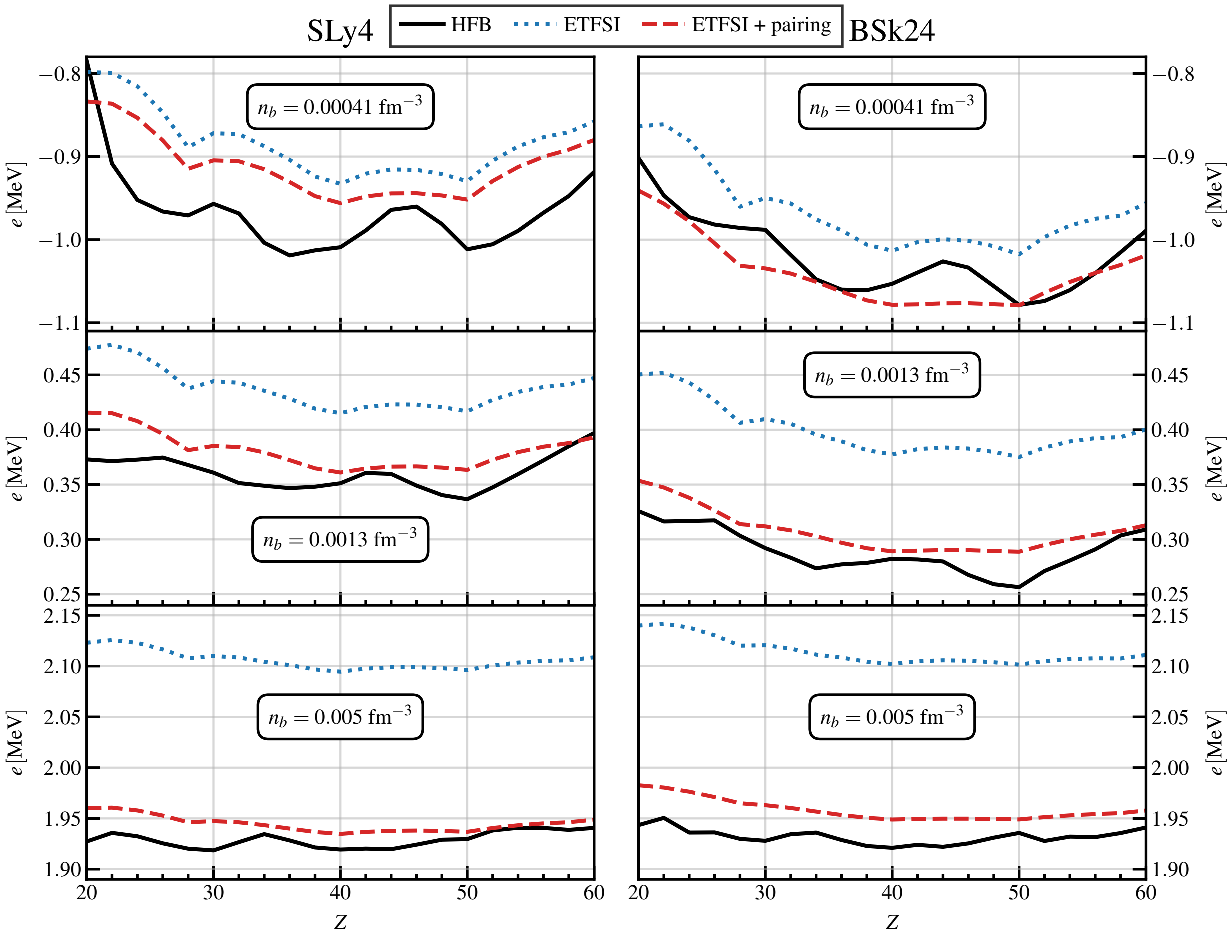

Figure 4.4: Selected slices of the energy surface at fixed baryonic densities n_b, showing the variation of e with Z. Black solid lines show the HFB results, blue dotted lines the ETFSI results and the red dashed lines the results for ETFSI with neutron and proton pairing included. Results with the SLy4 functional (with strong pairing) are shown in the left column, and those with BSk24 are shown in the right column. The HFB calculations use the optimum values of R_{WS} found with the ETFSI+pairing method.

WS cells at a few selected n_b, using the functionals SLy4 and BSk24. For the SLy4 functional, the strong pairing was used. The results obtained with BSk21 were almost identical to BSk24, so we do not show them in the figure. For each WS cell, the energy minimization is performed using the full ETFSI method, with or without pairing. The parameters of the resulting WS cells $(n_b, Z, R_{\mathrm{WS}})$ were used to perform HFB calculations using the same functionals. We have previously performed fully self-consistent HFB calculations [Pas17] using the SLy4 functional and the strong pairing interaction given in Equation 4.9, not using the ETFSI cell parameters. We found that, while this leads to slightly different minima, they all still lie within the error bars estimated in that work.

The energy dependence as a function of Z for a full ETF calculation would be a smooth parabola, but due to the Strutinsky integral correction, we clearly observe a modification to the total energy resulting from shell structure. By comparing the ETFSI calculations with and without pairing, we observe that the positions of the minima do not change, but we observe a general reduction in the relative energy difference between the shell or sub-shell closure values and between the other WS cells. As discussed in Ref. [Pea15], this is mainly the effect of proton pairing. The neutron pairing acts to globally shift the total energy as shown in Fig. 4.3.

The HFB results are remarkably close to the ETFSI+pairing ones: near the drip density, $n_b = 0.00041$ fm^{-3}, there is a larger discrepancy between HFB and ETFSI+pairing. This energy difference is of the order of ≈ 100 keV per particle. At these low densities, the energy from the cluster is greater than that from the neutron gas, and so the different density profiles of the ETFSI and HFB methods, seen in Fig. 3.3, are more important. The correction for neutron pairing is also less accurate at these very low densities.

For both SLy4 and BSk24, we find the two local minima at $Z = 40$ and $Z = 50$ for ETFSI+pairing, as also found by other works [Pea12; Pea15; Pea18]. However, the minima found with HFB take several values between $Z = 36$ and $Z = 50$. The small discrepancy could be related to the role of neutron shell effects of the cluster that are not taken into account within the ETFSI method. From $n_b = 0.0013$ fm^{-3}, when the neutron gas contribution starts to become more important, there is a remarkable agreement between the full HFB calculation and the ETFSI+pairing. This result confirms our previous hypothesis concerning the discrepancy observed between the two methods in Chapter 3. At this density, the total energy difference between the two methods is less than 10 keV per particle. The energy minimum obtained with HFB is at $Z = 50$, while the one with ETFSI+pairing is at $Z = 40$. As discussed in Ref. [Pas17], the accuracy of our HFB code is $\approx$ 4–5 keV per particle. Inspecting the figure, we notice that the relative energy difference between the HFB configuration at $Z = 40$ and $Z = 50$ is ≈ 2 keV per particle, clearly within the error of our calculations.

At a higher baryonic density $n_b = 0.005$ fm^{-3}, the agreement between the HFB and ETFSI+pairing remains, although the energy minima obtained by the two calculations do not agree. However they are still compatible due to the error we estimate for the HFB calculations. From this figure, we conclude that the inclusion of neutron pairing correlations in the ETFSI method leads to a very good agreement in the total energy per particle with the more involved HFB calculation.

4.5 Results for the inner crust

Having demonstrated the compatibility between the ETFSI+pairing and HFB methods, it is now possible to use ETFSI+pairing for systematic calculations of the inner crust. We first tested our method, without neutron pairing, against previous work. We used BSk21 and SLy4, as in Ref. [Pea12], and BSk24, as in Ref. [Pea18]. For all of these functionals, we found that the energy minimum occurs at $Z = 40$ in the range $0.00025\ \text{fm}^{-3} \leq n_b \leq 0.048\ \text{fm}^{-3}$ (as in the previous work), except for at very low densities, less than $\approx 0.01\ \text{fm}^{-3}$, where we find $Z = 50$. As noted in [Pea12], the two local minima corresponding to $Z = 40$ and 50 are very close in energy at low densities. This result is independent of whether or not we add the energy correction from neutron pairing correlations.

We attribute the discrepancy in our results to our treatment of the 4th-order ETF contributions to the energy (explained in Sec. 3.2). The smaller clusters found at these lower densities have less diffuse surfaces. Therefore, using the full 4th-order expressions with its higher-order derivatives is more vulnerable to numerical inaccuracies. A possible source of error is the way the total energy is calculated. These small numerical discrepancies are related to the method of numerical integration and we have seen that they are sufficient to explain the different minima observed at very low density, as discussed in Ref. [Pea12].

In Fig. 4.5, we present the equation of state obtained with a full ETFSI minimization, using SLy4. ETFSI results are shown with blue dotted lines, and ETFSI+pairing results (with strong pairing) with red dashed lines. As expected, the inclusion of neutron pairing effects in the system decreases the energy per particle, as shown in Fig. 4.5, but it does not affect the global trend.

In Fig. 4.6, we compare other properties of the WS cells obtained using SLy4 with and without pairing. In panel a of Fig. 4.6, we observe a larger total nucleon number A is the case of ETFSI+pairing. This reflects in a small reduction of the proton fraction $Y_p = Z/A$ as shown in panel b, and a small increase of the WS cell radius R_{WS}, shown in panel c. This adds to the reliability of the ETFSI method, whose semiclassical Wigner–Kirkwood expansion is exact in the limit of PNM ($Y_p \to 0$).

The pressure, defined as

$$P = -\left(\frac{\partial E}{\partial V}\right)_{T,N,Z}, \tag{4.10}$$

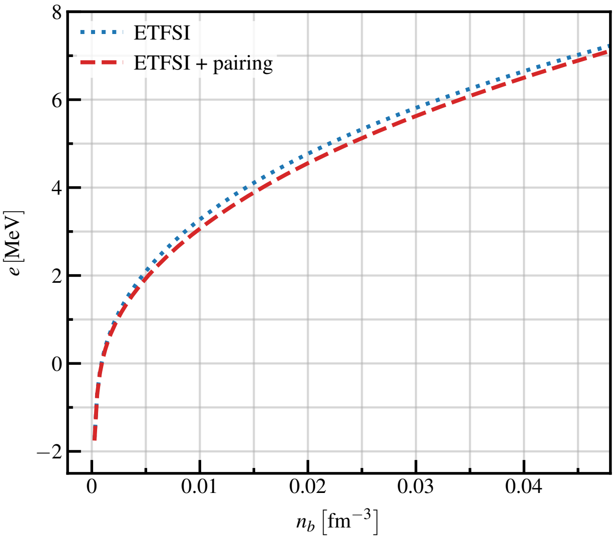

Figure 4.5: Energy per particle e in the inner crust using the SLy4 functional. The ETFSI result is shown by the blue dotted line, and the ETFSI+pairing (using the strong pairing) result by the red dashed line.

is calculated as the sum of three contributions: the nucleon pressure P_{nuc}, the electron gas pressure P_e, and the Coulomb exchange contribution $P_{\text{Coul,ex}}$. P_{nuc} is given by

$$P_{\text{nuc}} = \frac{\hbar^2}{3M}\tau_n + \sum_{q=0,1}\left[\left(\rho^{\text{gas}}\right)^2 C_q^{\rho} + \frac{5}{3}\rho^{\text{gas}}\tau_n C_q^{\tau} + \left(\rho^{\text{gas}}\right)^3 \frac{\partial C_q^{\rho}}{\partial \rho^{\text{gas}}} + \left(\rho^{\text{gas}}\right)^2 \tau_n \frac{\partial C_q^{\tau}}{\partial \rho^{\text{gas}}}\right], \tag{4.11}$$

where $\tau_n = \frac{3}{5}(3\pi^2)^{2/3} n_n(R)^{5/3}$, and the coupling constants $C_q^{\rho,\tau}(\rho)$ (defined in Appendix A) are all evaluated at $\rho = \rho^{\text{gas}}$. Since we assume here a constant electron density n_e, the pressure contributions arising from the electrons have an analytical form. P_e is given by

$$P_e = n_e m_e c^2 \frac{3}{8x^3}\left[x\left(\frac{2x^2}{3} - 1\right)\sqrt{1+x^2}\right] + \sinh^{-1} x, \tag{4.12}$$

where

$$x = \frac{\hbar c}{m_e c^2}\left(3\pi^2 n_e\right)^{1/3}. \tag{4.13}$$

$P_{\text{Coul,ex}}$ is given by

$$P_{\text{Coul,ex}} = \frac{e^2}{8}\left(\frac{3}{\pi}\right)^{1/3} n_e^{4/3}. \tag{4.14}$$

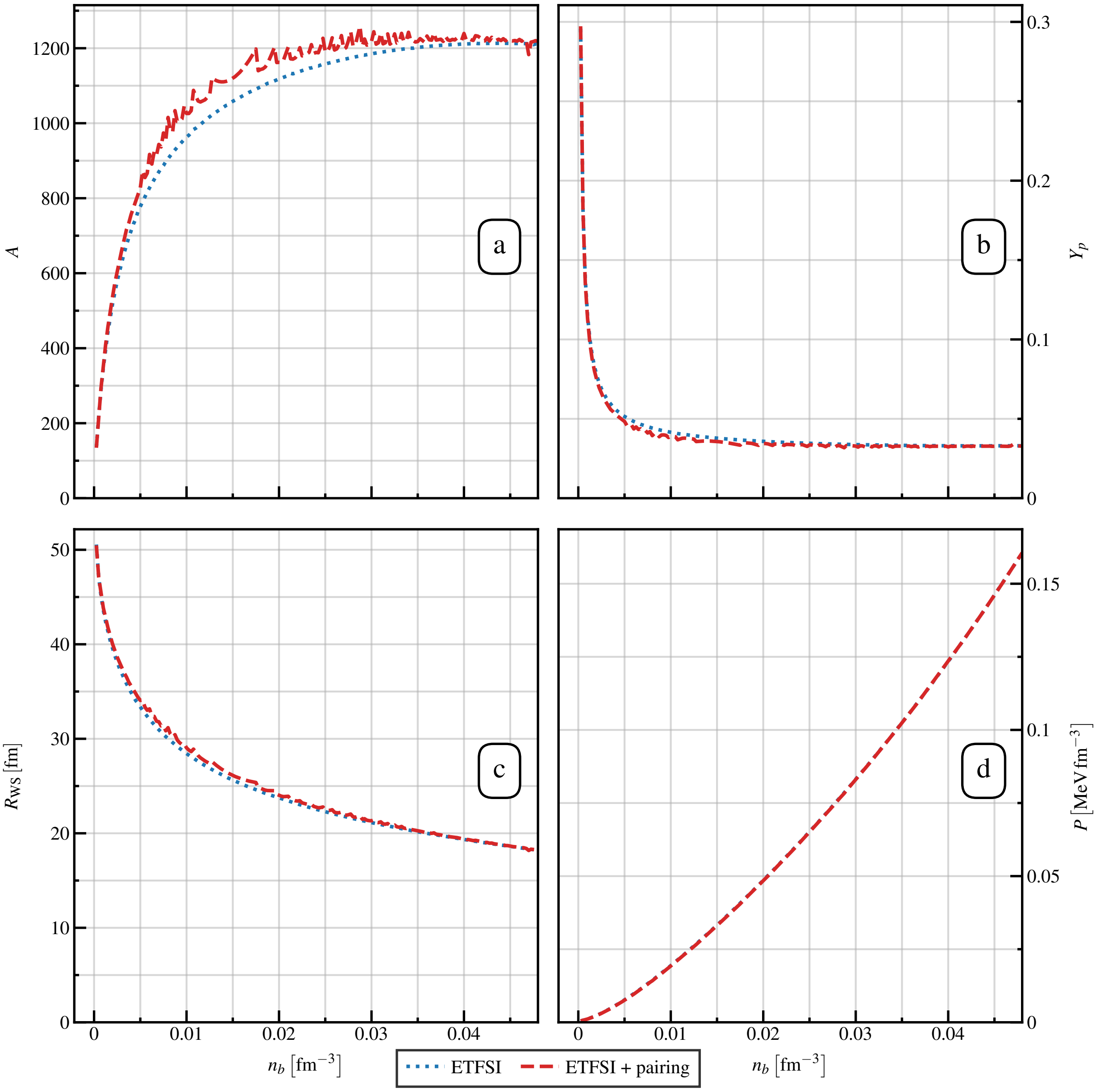

Figure 4.6: The variation through the inner crust of: the total nucleon number A (panel a), proton fraction Y_p (panel b), WS cell radius R_{WS} (panel c) and pressure P (panel d). ETFSI results are shown with blue dotted lines, and ETFSI+pairing results with red dashed lines.

A full derivation of each contribution is provided in Appendix B of Ref. [Pea12]; since we assume here that there is no proton gas, the expressions shown above are simplified slightly compared with those given in this reference.

In the presence of neutron pairing the pressure of the cell decreases but, as panel *d* of Fig. 4.6 shows, this difference is negligible, and is certainly far smaller than the difference that would arise from using different functionals.

All of these observed differences are at their greatest around $n_b = 0.015$ fm^{-3}. This is near the densities where the PNM pairing gaps, shown in Fig. 4.2, are at their maximum. The small bumps for the ETFSI+pairing case in Fig. 4.6, most notably in panel *a*, can be attributed to the inclusion of the SI correction and pairing in the second minimization step, when the total nucleon number A is determined (see Sec. 3.2.1).

We find that, for all functionals and densities tested, the inclusion of neutron pairing does not change the optimum Z. This is easily understood by looking at panel *b* of Fig. 4.3, where the contribution to e from neutron pairing is almost constant with respect to Z.

4.6 Summary

We have presented a systematic comparison between solving the HFB equations and using the ETFSI method, using exactly the same numerical conditions. We have observed that the inclusion of neutron pairing correlations in ETFSI using a simple LDA approximation leads to a remarkable reduction in the discrepancy between the two methods, showing the success of using ETFSI+pairing for the determination of the properties of WS cells in the inner crust.

After neutron pairing is included in the modeling of the inner crust, we find no change in the prediction of the optimum proton number Z at a given baryonic density n_b, for any of the functionals SLy4, BSk21 and BSk24. The location of the minimum of the nuclear contribution, dictated by the choice of functional, has a much bigger influence on the optimum Z.

The additional neutron pairing energy contribution leads to a general energy reduction in the Wigner–Seitz cell across the range $20 \leq Z \leq 60$ investigated. The most interesting effect of neutron pairing is the increase in the radius of the WS cells and the number of neutrons per cell, which means a small decrease in the proton fraction is observed. The pressure is also slightly decreased, but the change is not significant.

We conclude that ETFSI+pairing method is capable of giving a very accurate description of the structure of the inner crust. The results obtained are of the same quality as more advanced HFB calculations done under the same numerical conditions. We recall that given the proximity in energy of the minima, small numerical inaccuracies may lead to different minima, thereby explaining the apparent discrepancy of results within the scientific literature.

The reliability of the ETFSI+pairing method calls for a *hybrid* approach to inner crust calculations: HFB would be still be used at lower densities, where it has a superior quality, and at higher densities up to the crust-core transition, ETFSI+pairing would be used.

Chapter 5

The effect of functional choice on inner crust structure

In Chapter 4, we developed the ETFSI+pairing method, and validated its ability to reproduce HFB results. We now use it to investigate the role played by the particular Skyrme interaction chosen to study the inner crust.

The HFB and ETFSI methods have typically yielded different results for the structure of the inner crust. In particular, we observed that by adding to ETFSI the effects of neutron pairing correlations under a simple local density approximation, the resulting energy per particle agrees well with that obtained using the HFB method, apart from the very low density region where the outer-inner crust transition takes place.

Having quantified the agreement of this ETFSI+pairing method with HFB, we can now address an interesting question, namely, why Zirconium isotopes (i.e. clusters with $Z = 40$) are consistently predicted throughout the inner crust [Pea12; Pea18; Pea19; PCP20; Mon20]. To answer this, we perform systematic calculations of the inner crust EoS, selecting several Skyrme functionals whose various infinite nuclear matter (INM) properties [Dut12] cover reasonable ranges. By investigating possible relationships between the INM properties of Skyrme functionals and the proton content and pressure of the WS cells, we aim at providing a better understanding of previous investigations of the structure of the inner crust.

5.1 INM properties of Skyrme functionals

According to Ref. [Dut12], more than 240 Skyrme functionals have been published in the literature. Typically, their parameters are adjusted to reproduce the binding energy of some (or all) atomic nuclei, and also some INM properties. There is no standard parameter fitting protocol; various (pseudo)-observables are used in fitting, with widely varying uncertainties. As a consequence, it is difficult to assess the quality of functionals.

The neutron gas in the WS cell is similar to an infinite nuclear system, and comprises the majority of the baryonic matter in the inner crust. We therefore focus on four INM properties of the functionals: the saturation density n_0, and then the energy per particle at saturation E_0, the symmetry coefficient J, and the slope of the symmetry energy at saturation L. These quantities depend exactly on the EoS of INM [PC09], and so one can expect that variations in the EoS lead to modifications in the energy per particle of the neutron gas, thus changing the relative energy contributions from baryons and electrons in the WS cell, and ultimately affecting the chemical composition and pressure in the inner crust.

The EoS of symmetric nuclear matter (SNM) at density n is given by

$$e_{\mathrm{SNM}}(n) = \frac{3\hbar^2}{10M}k_{\mathrm{F}}^2(n) + \frac{3}{8}t_0 n + \frac{3}{80}\left[3t_1 + t_2(5+4x_2)\right] n k_{\mathrm{F}}^2(n) + \frac{1}{16}t_3 n^{\sigma+1}, \tag{5.1}$$

where $k_{\mathrm{F}}(n) = (3\pi^2 n/2)^{1/3}$. E_0 is then defined as $e_{\mathrm{SNM}}(n_0)$. The symmetry energy at a given density n in symmetric nuclear matter is

$$\begin{aligned}\mathcal{S}(n) = {} & \frac{\hbar^2}{6M}k_{\mathrm{F}}^2(n) - \frac{1}{8}t_0(2x_0+1)n \\ & + \frac{1}{24}\left[-3t_1x_1 + t_2(4+5x_2)\right] n k_{\mathrm{F}}^2(n) - \frac{1}{48}t_3(1+2x_3)n^{\sigma+1}.\end{aligned} \tag{5.2}$$

J is then defined as $\mathcal{S}(n_0)$. The slope of the symmetry energy at saturation is given by

$$\begin{aligned}L = 3n_0\left(\frac{\partial\mathcal{S}}{\partial n}\right)_{n=n_0} = {} & \frac{\hbar^2}{3M}k_{\mathrm{F0}}^2 - \frac{3}{8}t_0(2x_0+1)n_0 \\ & + \frac{5}{24}\left[-3t_1x_1 + t_2(4+5x_2)\right] n_0 k_{\mathrm{F0}}^2 - \frac{\sigma+1}{16}t_3(1+2x_3)n_0^{\sigma+1},\end{aligned} \tag{5.3}$$

where $k_{\mathrm{F0}} = (3\pi^2 n_0/2)^{1/3}$.

e_{SNM}, $\mathcal{S}$, and L each have extra terms for the BSk forces (BSk18 and newer), which are provided in Appendix A.

In Fig. 5.1, we show as histograms the distributions of n_0, E_0, J, and L, for all the functionals in Ref. [Dut12]. Not all functionals given in Ref. [Dut12] are shown in the lower two panels (J and L). In our selection process, we imposed two additional constraints on J and L, namely $30 \leq J \leq 35$ MeV and $L = 58 \pm 18$ MeV. These ranges of values are the ones suggested in Ref. [Dut12]. These constraints are to some extent arbitrary, as there is no consensus on

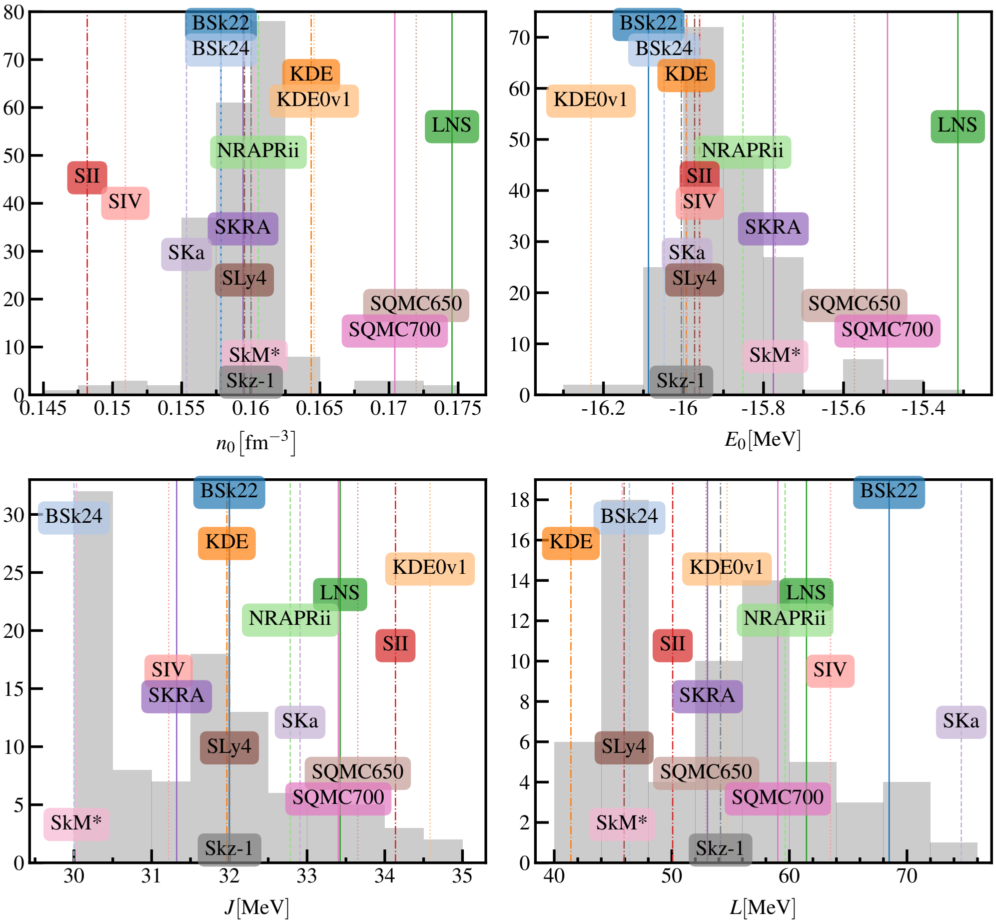

Figure 5.1: Each panel shows the distribution of the Skyrme functionals given in Ref. [Dut12] for four INM properties. Starting from the top left panel and going clockwise we show n_0, E_0, L and J. The values of each quantity for the fifteen functionals selected in this work are shown as labelled vertical lines.

what constitutes reasonable ranges of values for J and L, but they are consistent with the findings of recent analyses [Tsa12b; Che10; Vid09; Roc11; Li14], and with results and associated uncertainties from new chiral EFT calculations [DHS19; Dri20].

From this group, we selected fifteen functionals which cover a wide range of values for each of n_0, E_0, J, and L: BSk22 and BSk24 [GCP13], KDE [ASA05], KDE0v1 [ASA05], LNS [Cao06], NRAPRii [Ste13] (NRAPR [Ste05] with the spin-orbit strengthened), SII [VB72], SIV [Bei75], SKRA [Ras00], SKA [Köh76], SLy4 [Cha98], SQMC650 and SQMC700 [Gui06], SkM* [KTB80; Bar82], and Skz-1 [MNV02]. Their INM properties are labelled in Fig. 5.1. Five of them — **KDE0v1**, **LNS**, **NRAPRii**, **SKRA** and **SQMC700** — are consistent with all the INM constraints presented in Ref. [Dut12], and are named in that reference and hereafter as the CSkP* set.

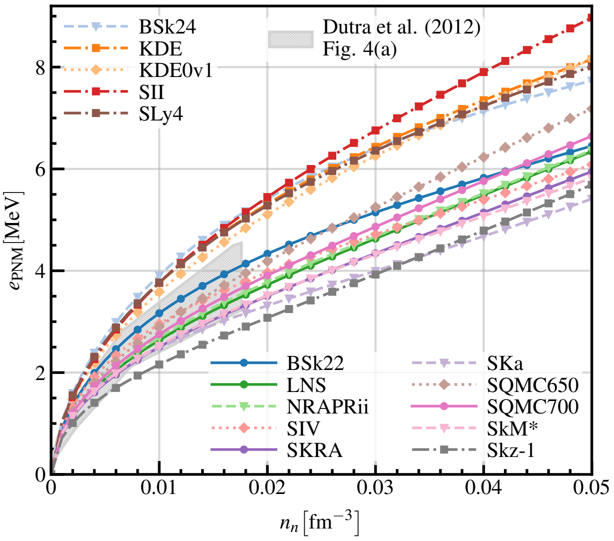

Figure 5.2: The EoS of PNM as a function of the neutron density n_n for the 15 functionals selected in this work. The shaded area gives the constraint given in Fig. 4(a) of Ref. [Dut12]. The functionals labelled in the upper left are the Stiff set, and those in the lower right the Soft set.

For our functional selection, we also show energy per particle e_{PNM} in pure neutron matter (PNM) in Fig. 5.2, for the density range relevant for spherical inner crust calculations. e_{PNM} at neutron density n_n is given by

$$\begin{aligned} e_{\mathrm{PNM}}(n_n) = &\frac{3\hbar^2}{10M_n}k_{\mathrm{F}n}^2(n_n) + \frac{1}{4}t_0(1-x_0)n_n + \frac{3}{40}t_1(1-x_1)n_n k_{\mathrm{F}n}^2(n_n) \\ &+ \frac{9}{40}t_2(1+x_2)n_n k_{\mathrm{F}n}^2(n_n) + \frac{1}{24}t_3(1-x_3)n_n^{\sigma+1}. \end{aligned} \tag{5.4}$$

where $k_{\mathrm{F}n}(n_n) = (3\pi^2 n_n)^{1/3}$. e_{PNM} contains extra terms for the BSk forces (BSk18 and newer), which are provided in Appendix A.

The functionals clearly fall into two distinct families: the set BSk24, KDE, KDE0v1, SII, and SLy4, with a stiff EoS at these low densities (hereafter the *Stiff* set), and the set BSk22, LNS, NRAPRii, SIV, SKRA, SKa, SQMC650, SQMC700, SkM*, and Skz-1, with a very soft EoS (hereafter the *Soft* set). On the same figure, we have added a shaded area which corresponds to the range spanned by several *ab-initio* calculations used to derive the EoS in PNM, and which is discussed in Fig. 4(a) of Ref. [Dut12].

The Stiff set, including SLy4 and BSk24 which have been widely used for NS calculations, are in disagreement with the *ab-initio* calculations at these densities. In contrast, the majority

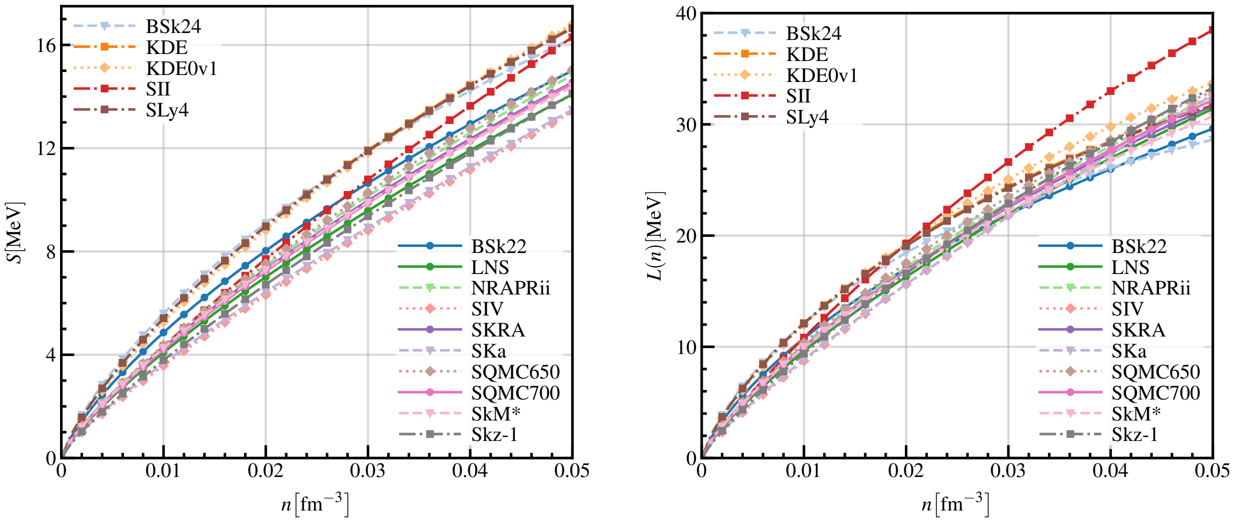

Figure 5.3: Left: the symmetry energy S as a function of density n for the 15 functionals selected in this work. Right: the slope of the symmetry energy, L, as a function of density n for the 15 functionals selected in this work. The functionals labelled in the upper left of each plot are the Stiff set, and those in the lower right the Soft set.

of the Soft set are in reasonable agreement, apart from Skz-1 which is very soft. However, the *ab-initio* calculations selected in Ref. [Dut12] do not represent the entire range available in the literature. As shown in Ref. [GCP13], BSk24 and SLy4 are compatible with the error bars provided by chiral effective field theory calculations from Ref. [Tew13].

The inner crust does not only comprise neutrons, but also has a significant proton fraction, and so it is interesting to observe the behaviour of S in the relevant density region and not only at n_0. This is shown in the left panel of Fig. 5.3, where we again observe a similar grouping into the Stiff and Soft sets as shown in Fig. 5.2. The reason is quite simple and can be understood from Fig. 5.1: the vast majority of the functionals have values of n_0 and E_0 in a very narrow range. This means that all these functionals have a very similar EoS in SNM in the low density region, as shown in Fig. 5.4. Since S is just the difference between the EoS in PNM and SNM (within the parabolic approximation [DPN16]), it follows that the pattern observed in PNM repeats here in a very similar way. The exceptions to this simple rule are SII and SIV. They have extremely low values of n_0, shown in Fig. 5.1, and so a significantly different EoS in SNM compared to the other functionals. LNS, SQMC650, and SQMC700 also show a slightly different behaviour in SNM approaching n_0, which is easily understood from their unusually high values for n_0 and E_0, as shown in Fig. 5.1.

Finally, in the right panel of Fig. 5.3, we show how the the slope of the symmetry energy, L (Eq. 5.3), evolves at subnuclear densities. We see a similar behaviour to S, where there is a

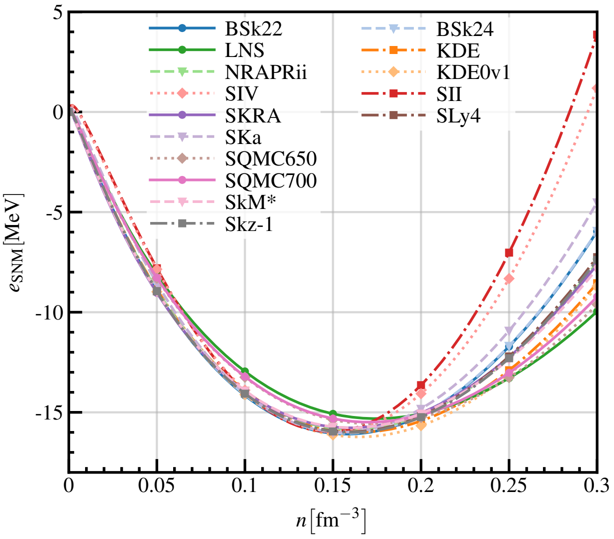

Figure 5.4: The EoS of SNM e_{SNM} as a function of density n for the 15 functionals selected in this work. The functionals labelled in the upper left are the Soft set, and those in the upper right the Stiff set.

small separation between the Stiff and Soft sets, but only at the very lowest densities.

5.2 Inner crust composition

To calculate the EoS and determine the chemical composition of the inner crust, we minimise the total energy per particle e in the WS cell, given in Eq. 2.2, using the method explained in Chapters 3 and 4. The pairing strength v_{0q} for each functional was chosen with the same procedure as for the strong interaction for SLy4 in Chapter 4, such that the maximum pairing gap in PNM is $\approx$ 3 MeV. The functionals have different effective masses m^*, which have an impact on the pairing gap, and so v_{0q} must be adjusted accordingly to reproduce a similar gap. We cover the range of baryonic densities $n_b \in [0.00025, 0.05]$ fm^{-3}, above which non-spherical pasta phases are expected to appear [PCP20], and the range of proton numbers $Z \in [16, 60]$.

5.2.1 Selected baryonic densities

We first show results for a few selected baryonic densities $n_b = 0.01, 0.02$ and 0.03 fm^{-3}, for a smaller group of functionals. Fig. 5.5 illustrates the energy per particle as a function of Z. We show a re-scaled energy per particle, e_s, defined as

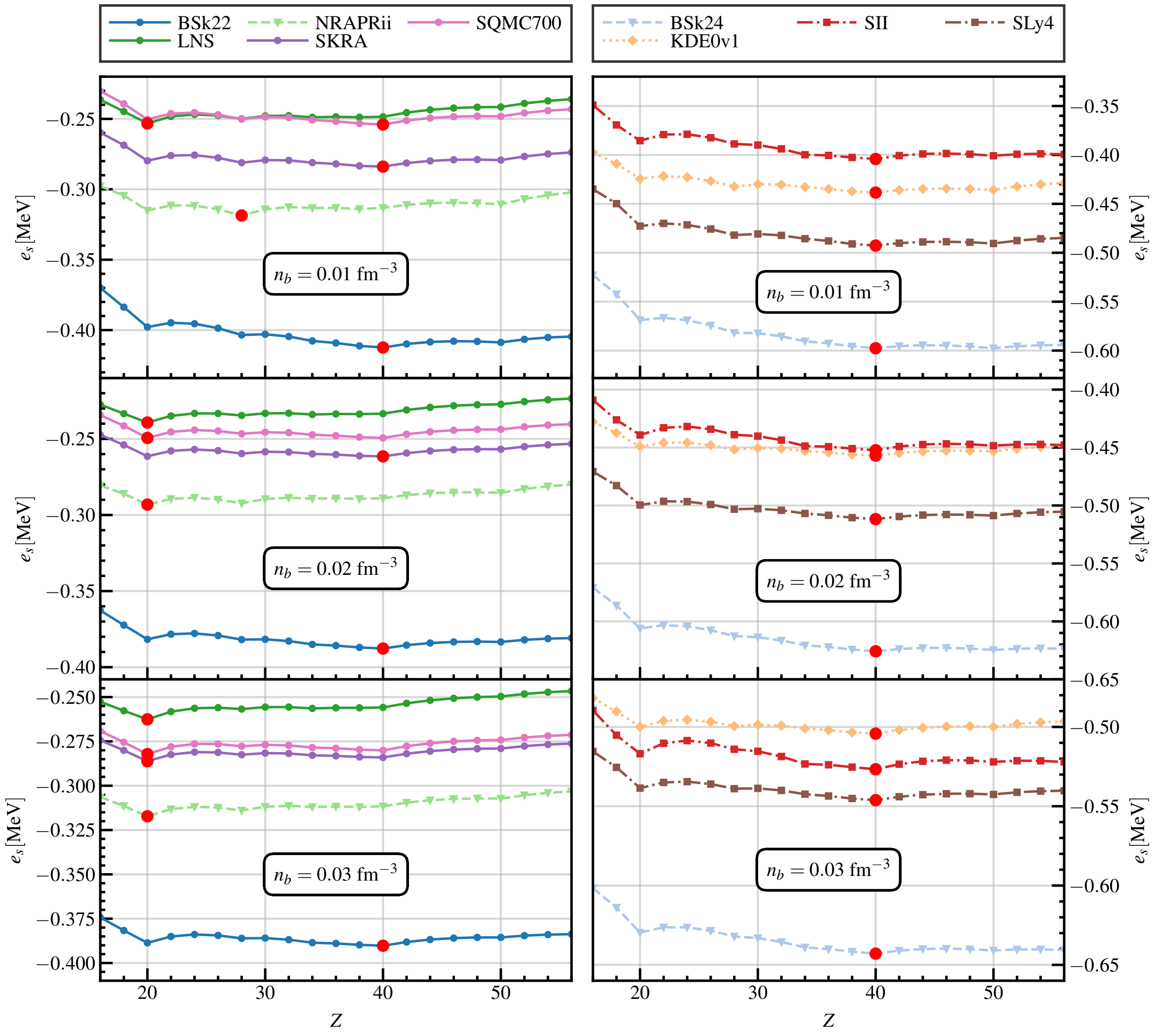

Figure 5.5: The re-scaled energy per particle e_s, defined in Eq. 5.5, for selected functionals from the Soft (left column) and Stiff (right column) sets, at three values of baryonic density n_b. The large dot on each curve represents the position of the energy minimum.

$$e_s(n_b) = e(n_b) - e_{\mathrm{PNM}}(n_b) - e_{n,\mathrm{pair}}(n_b), \tag{5.5}$$

where $e_{n,\mathrm{pair}}$ is the neutron pairing energy per particle. This is purely for visual reasons, so that all values lie within a similar energy range. Since e_{PNM} is independent of Z, and $e_{n,\mathrm{pair}}$ is roughly constant with respect to Z (demonstrated in Chapter 4), this results in a simple shift in e for a given functional. In the left column are five from the Soft set: **BSk22**, **LNS**, **NRAPRii**, **SKRA**, and **SQMC700**; in the right column are four functionals from the Stiff set: **BSk24**, **KDE0v1**, **SII**, and **SLy4**, as explained in Sec. 5.1.

In this figure, we clearly see the different behaviour of the Soft and Stiff sets. The Stiff set has a persistent minimum at $Z = 40$, while the Soft set has minima that favour lower Z, or that shift towards lower Z as n_b increases, with all favouring $Z = 20$ at $n_b = 0.03$ fm^{-3}. The exception in the Soft set is BSk22, which transitions to $Z = 20$ just above $n_b = 0.03$ fm^{-3}, and which has one of the stiffest PNM EoS in this set. NRAPRii is unique among all the functionals investigated, in that it favours $Z = 28$ at $n_b = 0.01$ fm^{-3}. This is likely related to an issue involving the spin-orbit parameter W_0. See the discussion in Ref. [Ste13] for more details. Below $n_b = 0.01$ fm^{-3}, nearer the transition region between the outer and inner crust, other finite-size effects not considered in our ETFSI+pairing method may become significant, changing the results. The HFB method is preferable in this very low density range.

To better understand the origin of the different minima, we plot in Fig. 5.6 the *smooth* part of the total energy per particle e_{smooth}, defined as

$$e_{\mathrm{smooth}} = e - e_{n,\mathrm{pair}} - (e_p^{\mathrm{SI}} + e_{p,\mathrm{pair}}), \tag{5.6}$$

where the last term is the sum of the SI correction with BCS pairing for protons, and the proton pairing energy, as explained in Ref. [Pea15]. This results in a smooth parabola-like shape, with a single minimum. We select two representative functionals **SQMC700** and **BSk24**, from the Soft and Stiff sets respectively. The parabola shifts significantly in Z going between the two functionals. Furthermore, as n_b increases, we observe that for SQMC700 the minimum moves from $Z = 32$ to $Z = 28$, while for BSk24 it stays at $Z = 46$.

When the SI correction is included, as in Fig. 5.5, each functional at each density displays local minima at (semi-)magic Z values between 20 and 50. However, Fig. 5.6 shows how the global minimum in each case is governed more by the stiffness of the PNM EoS. In this work, we strictly consider no temperature effects. Since the various energy minima are quite close to each other, the inclusion of such effects may change this picture. See discussion in Ref. [Bur15]

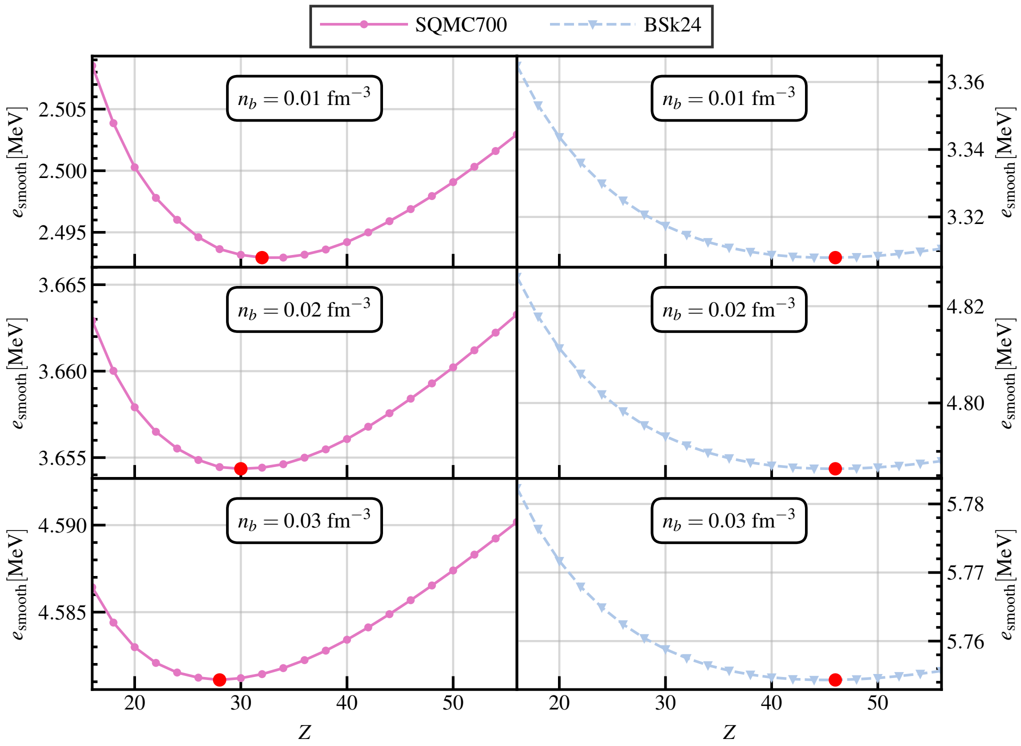

Figure 5.6: Total energy per particle, $e_{\rm smooth}$, obtained without using shell or pairing corrections, for two functionals at three representative baryonic densities n_b.

for more details.

5.2.2 Results for the full baryonic density range

A more systematic study of the evolution of the proton content of the clusters in the inner crust is illustrated in Fig. 5.7, for all functionals in the Soft and Stiff sets. For clarity, small vertical offsets have been added to each line, and the Soft and Stiff sets in are shown in separate panels. At very low n_b several values of Z are observed, but above $n_b = 0.02$ fm^{-3} only two minima are observed: $Z = 20$ and $Z = 40$. The minimum at $Z = 40$ seems to be favoured by most functionals at around $n_b = 0.01$ fm^{-3}, but at $n_b = 0.03$ fm^{-3} the majority of the Soft set have transitioned to the $Z = 20$ configuration. The only exception to this rough classification is SQMC650, whose $e_{\rm PNM}$ is the highest out of the Soft set, as seen in Fig. 5.2, and it maintains a $Z = 40$ minimum up to quite a high baryonic density of $n_b \approx 0.04$ fm^{-3}.

It is interesting to note that $Z = 20$ is favoured by functionals whose PNM EoS is compatible with *ab-initio* calculations. This result is also in good agreement with the findings of Ref. [Bal05]. Although further analysis is necessary, our results suggest that a better understanding of the EoS in low-density PNM may help to clarify the chemical composition of the

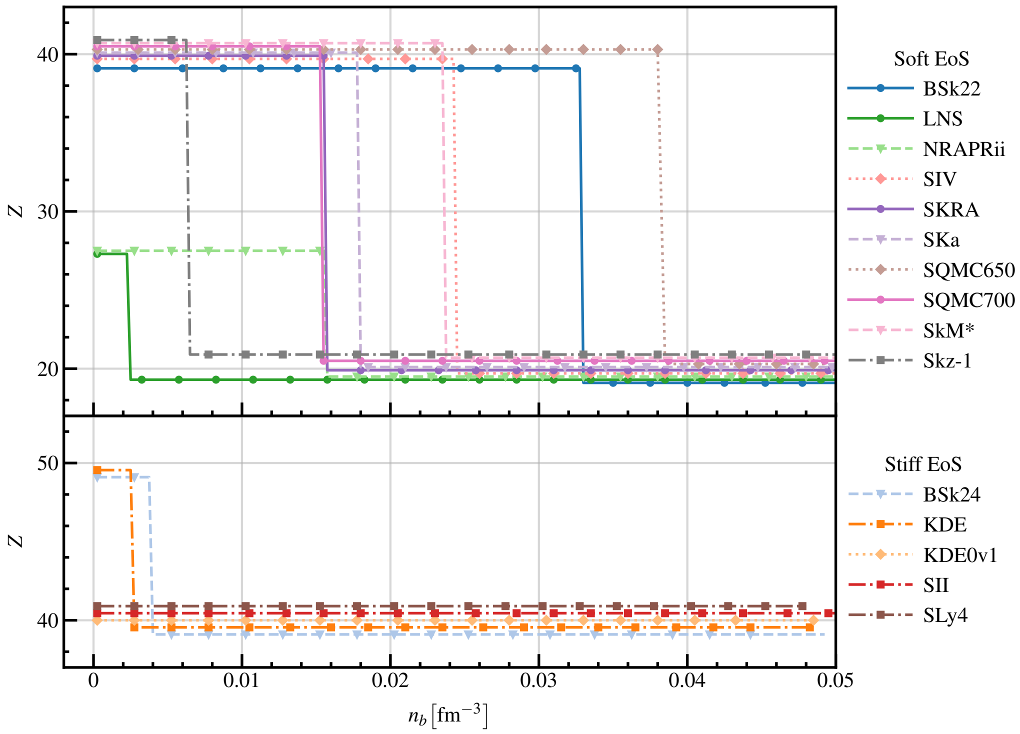

Figure 5.7: Proton content of WS cells in the inner crust as a function of the baryonic density n_b, for all functionals in the Soft and Stiff sets. A small vertical offset has been added to each line to make them more visible; all lines only take values from one of $Z = 20, 28, 40, 50$.

inner crust.

Having calculated the chemical composition of the inner crust, we now study its general properties with the different functionals. In Fig. 5.8, we show the total energy per particle e (Eq. 2.2) for the WS cells in the inner crust, obtained through the energy minimisation, as a function of the baryonic density n_b. The pattern formed by the various Soft and Stiff functionals is almost identical to that seen for e_{PNM}, shown in Fig. 5.2. This further supports the PNM EoS being the major driver of the inner crust EoS.

Another relevant astrophysical quantity is the proton fraction in the inner crust, $Y_p = Z/A$. It plays a role in the transport properties of a NS and in the determination of the neutrino mean free path in the stellar medium [IP82]. In Fig. 5.9, we report Y_p as a function of n_b for the same smaller selection of functionals shown in Fig. 5.5. The same feature already observed in Fig. 5.7 is clear: the Soft functionals predict WS cells with fewer protons, and have a lower Y_p, while the contrary is true for the Stiff functionals. At around $n_b = 0.02$ fm^{-3}, Y_p varies by up to a factor of 2 between the two sets. When Z in a WS cell changes, the baryon content of each WS cell follows this change quite closely. As a consequence, the factor of 2 observed

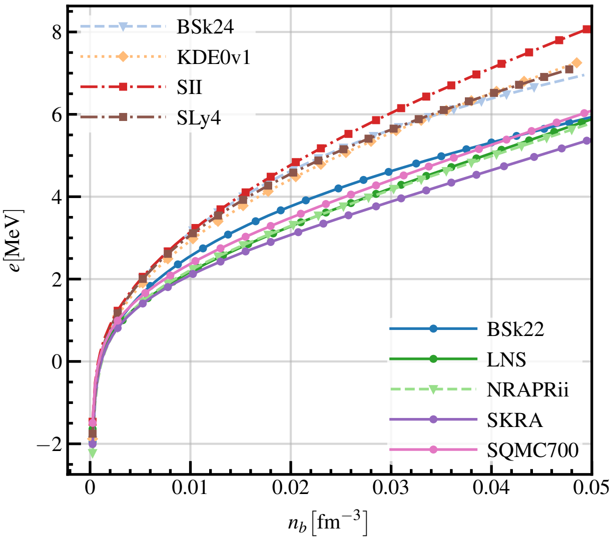

Figure 5.8: The energy per particle e in the inner crust, as a function of the baryonic density n_b. Four functionals from the Stiff set are shown, labelled in the upper left, and five from the Soft set, labelled in the lower right.

between the two dominant minima in Fig. 5.7 ($Z = 20, 40$) is conserved here.

It is worth commenting on the case of BSk24, a functional specifically created to be able to provide a unified description of the NS EoS. This was adjusted under many constraints, including the requirement that it reproduce the LS2 equation of state [LS08] in PNM, which was calculated using the microscopic Brueckner-Hartree-Fock method. The authors note in Ref. [GCP13] that they focused on supernuclear densities when constraining BSk24 to the LS2 EoS. As a result, the BSk24 PNM EoS is significantly stiffer than LS2 at inner crust densities. Around $n_b = 0.04$ fm^{-3}, LS2 is better approximated by SQMC650, SQMC700, and NRAPRii, than by BSk24.

In Refs. [Pea18; Pea19], the authors claim that the constraining PNM EoS has little effect on Y_p in the inner crust, and show that J is an important INM quantity. However, by inspecting carefully Figs. 5.2 and 5.9, we see that BSk24 (J = 30 MeV), SLy4 (J = 32 MeV), and KDE0v1 (J = 34.6 MeV) have a Y_p largely in the range $0.03 - 0.04$. The functionals with a softer PNM EoS — BSk22, LNS, NRAPRii, SKRA, and SQMC700 — have a Y_p mostly in the range $0.02 - 0.025$, despite having J ranging from 31.3 to 33.4 MeV. We therefore conclude that J is not the driving factor leading to large variations of Y_p, but it is the equation of state of PNM at low density, or equivalently S at low density as shown in the left panel of Fig. 5.3 and discussed in Sec. 5.1.

The softest functional investigated in Ref. [Pea18; Pea19], BSk22, which more closely fol-

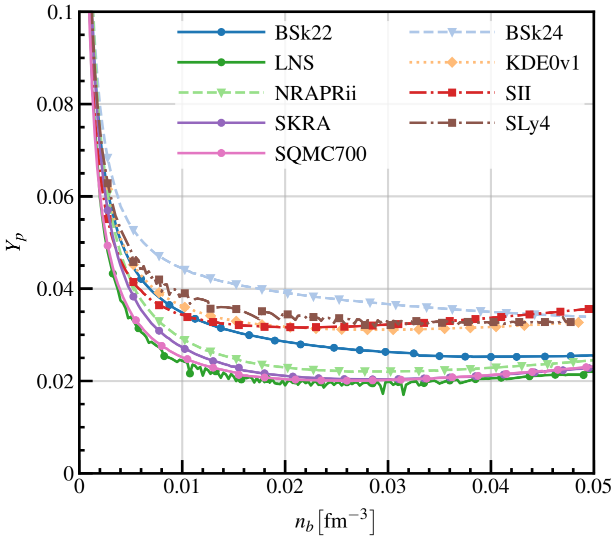

Figure 5.9: Proton fraction Y_p in the inner crust, as a function of the baryonic density n_b. Four functionals from the Stiff set are shown, labelled in the upper right, and five from the Soft set, labelled in the upper left.

lows LS2 at inner crust densities, gives results favouring an energy minimum at $Z = 20$ at intermediate inner crust densities, and lower values for Y_p, e, and P. This means that the results presented here are consistent with those in Refs. [Pea18; Pea19], but given the small variations in the properties of the functionals used, the authors were not able to observe such an interesting correlation.

It is also interesting to note from Fig. 5.9 that almost all of the CSkP* set, selected in Ref. [Dut12] according to several criteria based on INM properties, tend to favour a very small Y_p within the crust. The only exception is KDE0v1, from the Stiff set.

In Fig. 5.10, we show the surface energy coefficient $a_{\mathrm{surf}}^{\mathrm{MTF}}$ as calculated using the MTF approximation, introduced in Ref. [Jod16], which approximates very well the surface energy coefficient calculated in a full HF calculation. In the recent work of Carreau et al. [Car20], where they adopt a compressible liquid drop picture, it is claimed that the surface properties of the functional are the most important in the inner crust. However, by looking at Fig. 5.10, we see that there is no clear correlation between a_{surf} and the EoS, shown in Fig. 5.7. Neither the Soft or Stiff set show a consistently higher or lower value of $a_{\mathrm{surf}}^{\mathrm{MTF}}$.

In Fig. 5.11, we illustrate the evolution of the radius of the Wigner-Seitz cell, R_{WS}, as a function of the baryonic density, again for the smaller selection of functionals. While in the low density region, $n_b \in [0.00025, 0.015]$ fm^{-3}, we observe significant variations in the sizes of the cells, at higher baryonic densities, we notice that the size of the cell is almost independent

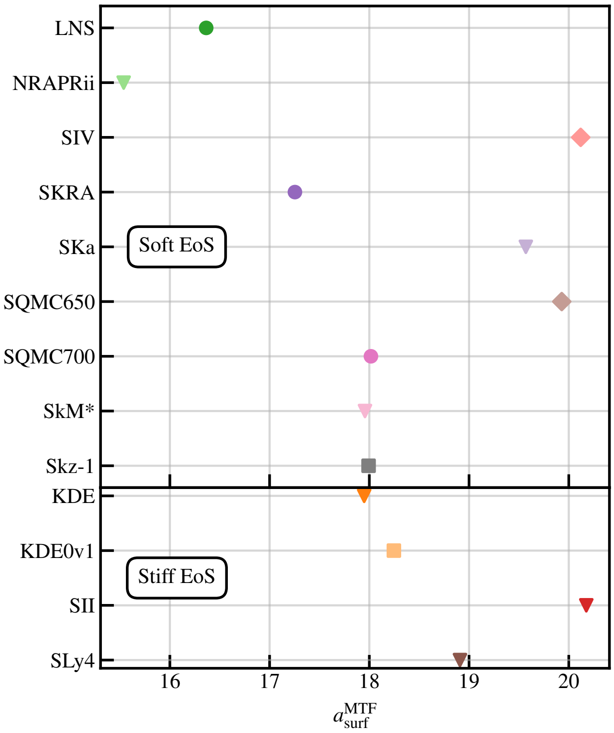

Figure 5.10: The surface energy coefficient $a_{\mathrm{surf}}^{\mathrm{MTF}}$ as calculated using the MTF approximation, introduced in Ref. [Jod16], for the various functionals investigated in this chapter.

of the functional. In particular, we clearly identify again the Stiff set and the Soft set, giving values of R_{WS} very close to each other. The sudden jumps shown in this figure correspond to abrupt changes in the chemical composition of the crust, as seen in Fig. 5.7.

Finally, in Fig. 5.12, we illustrate the evolution of the pressure P as a function of the baryonic density n_b, for the same eight functionals already discussed in Figs. 5.8 and 5.9. In this case, the separation into the Stiff and Soft sets is only visible up to around $n_b = 0.025$ fm^{-3}. We recall that the pressure depends on the derivatives of the EoS, rather than its value.

5.3 Summary

In this chapter we have performed a systematic analysis of the structure of the inner crust of a non-accreting NS, using the ETFSI+pairing method. By selecting 15 different functionals with different infinite nuclear matter properties, we have illustrated a possible correlation between the a functional's PNM EoS at low density, and the proton content and pressure of the Wigner-Seitz cells. In particular, we have shown that functionals with a *soft* PNM EoS at low densities tend to favour the $Z = 20$ minimum, as well as a lower proton fraction, and a lower pressure

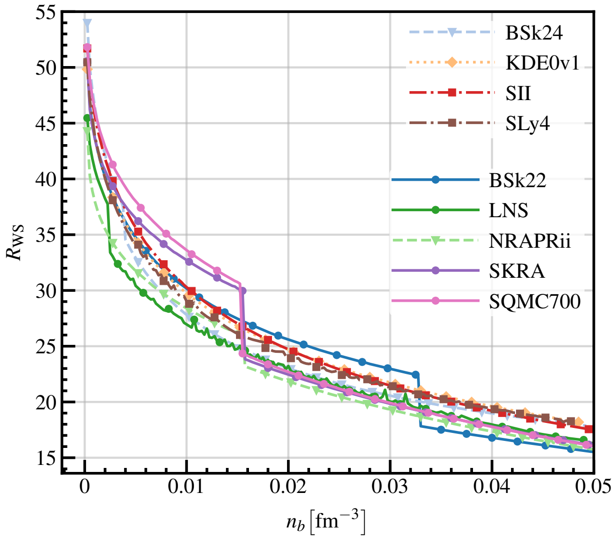

Figure 5.11: Radius of WS cells R_{WS} in the inner crust, as a function of the baryonic density n_b. Four functionals from the Stiff set are shown, labelled in the upper right, and five from the Soft set, labelled just below on the right.

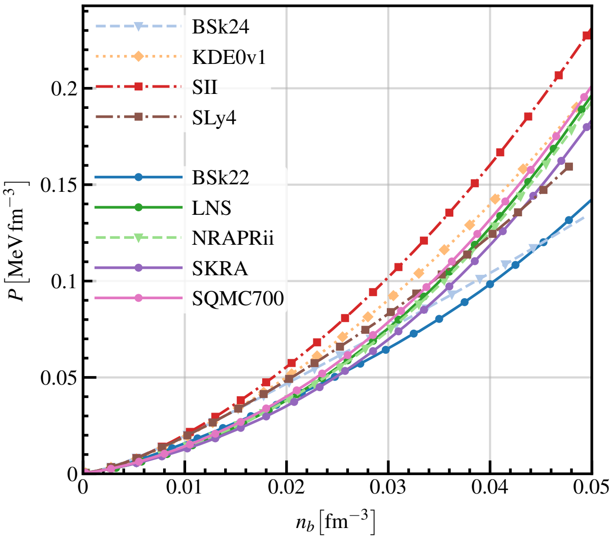

Figure 5.12: Pressure P in the inner crust, as a function of the baryonic density n_b. Four functionals from the Stiff set are shown, labelled in the upper left, and five from the Soft set, labelled just below on the left.

up to around $n_b = 0.025$ fm^{-3}, while functionals with a *stiff* PNM EoS show the opposite behaviour, and favour instead the $Z = 40$ minimum. This result clearly shows the importance of the constraining the PNM EoS more tightly at subnuclear densities in the adjustment protocol of Skyrme functionals used to study NS. This is not the *standard* procedure, since authors tend to focus more on the high density trend of the EoS; indeed, this is necessary to prevent the collapse of the NS, and to reproduce its global properties such as the maximum mass and radius [ZFH17]. More stringent constraints on functionals obtained by more recent *ab-initio* calculations at low density should pave the way toward a more reliable unified EoS for neutron star matter.

Chapter 6

The outer crust

As discussed in Refs. [RHS06; Cha20], at β-equilibrium the composition of each layer of the outer crust at a given pressure P is obtained by minimising the Gibbs free energy per nucleon. The latter is the sum of three main contributions: the *nuclear*, *electronic* and *lattice*. There has been some investigation into the possibility of the coexistence of multiple isotopes (in binary or ternary compounds) at a given density [CF16], but it was found that the effect on the EoS is very small. The effects of considering the system at a finite temperature have been presented in Ref. [Fan20]. Since a large fraction of nuclei present in the outer crust are extremely neutron-rich, their binding energies are not known experimentally, and consequently one has to rely on a nuclear mass model. We refer the reader to Ref. [Oer17] for a review of the properties of various equation of state (EoS) used to describe dense stellar matter.

Several models are available within the scientific literature with a typical accuracy, i.e., the root mean square (RMS) deviation of the residuals, of 500 keV [SLP18]. In recent years, some of these mass models have been equipped with additional algorithms such as kernel ridge regression [WZ20] or radial basis function interpolation [WL11; Niu18], thus reducing the typical RMS to $\approx$ 200–300 keV. Although such an RMS is remarkably low compared to the typical binding energy of a nucleus, the discrepancies between various models are still important, especially when used to predict the composition of the outer crust of a NS [Wol13].

Analysis of the residuals of various mass models shows that they do not show chaotic behaviour [Bar05], thus it should be possible to further improve their accuracy, at least up to the level of Garvey-Kelson relations [GK66], by adding additional terms to account for the missing physics. This may be a very complex task, but machine learning methods can provide major support in achieving this goal.

In recent years, several authors have tried to reduce the discrepancy between theory and experiment by supplementing various mass models with neural networks (NNs) [Cla99; Ath04;

Ath05; UPP16; Neu18; Pas20], where the NN learns the behaviour of the residuals. NNs are excellent interpolators [Les93], but they should be used with great care for extrapolation. The major problem is the presence of an unwanted trend related to the particular choice of the activation function. See Refs. [Xu21; PC20] for a more detailed discussion on the topic.

A possible alternative to NNs has been discussed in Ref. [Neu18], and it is based on Gaussian processes (GPs) [BO09; Pas17; She19]. This GP method assumes that the residuals originate from some multivariate Gaussian distribution, whose covariance matrix contains some parameters to be adjusted in order to maximise the likelihood for the GP's fit to the residuals. The main advantage of a GP over a NN is that its predictions do not contain unwanted trends in extrapolation, but instead will always return to 0 after a predictable extrapolation distance. Moreover, GP predictions come equipped naturally with error bars. This is not the case for a standard NN (only Bayesian neural networks are equipped with posterior distributions that can be interpreted as error bars [Nea12]), and a more involved procedure is required to obtain an estimate [PC20]. We have previously tested the use of Gaussian processes as *emulators*, firstly of the energy per particle in the inner crust [Pas17], and secondly of the χ^2 surface in the fitting of nuclear models with Bayesian optimisation [She19].

In this chapter, we present a new mass table, made by combining the predictions of a Duflo-Zucker [DZ95] mass model with a GP, in order to further reduce the RMS of the residuals. We use the resulting model to analyse the composition of the outer crust of a NS. As previously done in Ref. [Pas20], we perform a full error analysis of the mass model and we use a Monte-Carlo procedure to propagate these statistical uncertainties through to the final EoS.

6.1 Gaussian process regression

We now introduce Gaussian processes, and their use as a regression tool. A Jupyter notebook is available as supplementary material; it was used to create Figs. 6.1 and 6.2, and contains additional plots which give a step-by-step introduction.

A Gaussian process (GP) is an infinite-dimensional Gaussian distribution. Similar to how a one dimensional (1D) Gaussian distribution has a mean μ and variance σ^2, a GP has a mean function $\mu(\mathbf{x})$, and a covariance function $k(\mathbf{x}, \mathbf{x}')$, also known as the kernel. In principle, $\mathbf{x}$ can be a vector of length d representing a point in a d-dimensional input space, but for now we will just consider the case $d = 1$, i.e., where x is a single number. Just as we can draw random samples (numbers) from a 1D Gaussian distribution, we can also draw random samples from a GP, which are functions $f(x)$. The kernel $k(x, x')$ tells us the typical correlation between the value of f at any two inputs x and x', and entirely determines the behaviour of the GP (relative to the mean function). In our work here, we use here a constant mean function of 0. The purpose of the GP is to capture any fluctuations around this mean function. In our application later to a nuclear mass model, the trend of the data is given by the nuclear model, and the GP describes anything not described well by the model.

GPs can be used for regression of data if the underlying process generating the data is smooth and continuous. See Ref. [RW06] for a thorough introduction to GPs for regression and machine learning. Many software packages are available for GP regression; for this work we use the Python package *GPy* [GPy20]. For a set of data $\mathcal{Y}(x) = \{y_1(x_1), y_2(x_2), \ldots y_n(x_n)\}$, instead of assuming a fixed form for the interpolating function, we treat the data as originating from a Gaussian process $\mathcal{GP}$:

$$\mathcal{Y}(x) \sim \mathcal{GP}(\mu(x), k(x, x')). \tag{6.1}$$

We adopt the commonly used *RBF* (radial basis function) kernel, also known as the squared exponential or Gaussian. A variety of other kernels are available; however, the RBF is the simplest and most popular choice, and has easily interpretable parameters for our work. It yields very smooth samples $f(x)$, and has the form

$$k_{\mathrm{RBF}}(x, x') = \eta^2 \mathrm{exp}\left[-\frac{(x-x')^2}{2\ell^2}\right], \tag{6.2}$$

where η^2, ℓ are parameters to be optimised for a given $\mathcal{Y}$. Both have easily interpretable meanings: η gives the typical magnitude of the oscillations of $f(x)$, and ℓ the typical correlation length in x. When $|x - x'|$ is small, the correlation is large, and we expect $f(x)$ and $f(x')$ to have similar values. As $|x - x'|$ grows beyond a few correlation lengths ℓ, the correlation between $f(x)$ and $f(x')$ drops rapidly to 0.

A simple way to understand GPs is to make use of Bayes' theorem. Before doing the *experiments* we have a prior distribution for $f(x)$, characterised by the kernel given in Eq. 6.2. We can then draw sample functions from this prior, which are fully determined by the parameters η^2, ℓ. In Fig. 6.1, we show five sample draws of functions $f(x)$ from some priors, which have $\eta = 1$ and various choices of ℓ. We observe that by varying ℓ we can have very different shapes in the prior samples. On average, they all lie within the shaded area representing 1σ confidence interval 68% of the time.

In Fig. 6.2 we show a simple demonstration of GP regression, where the underlying true

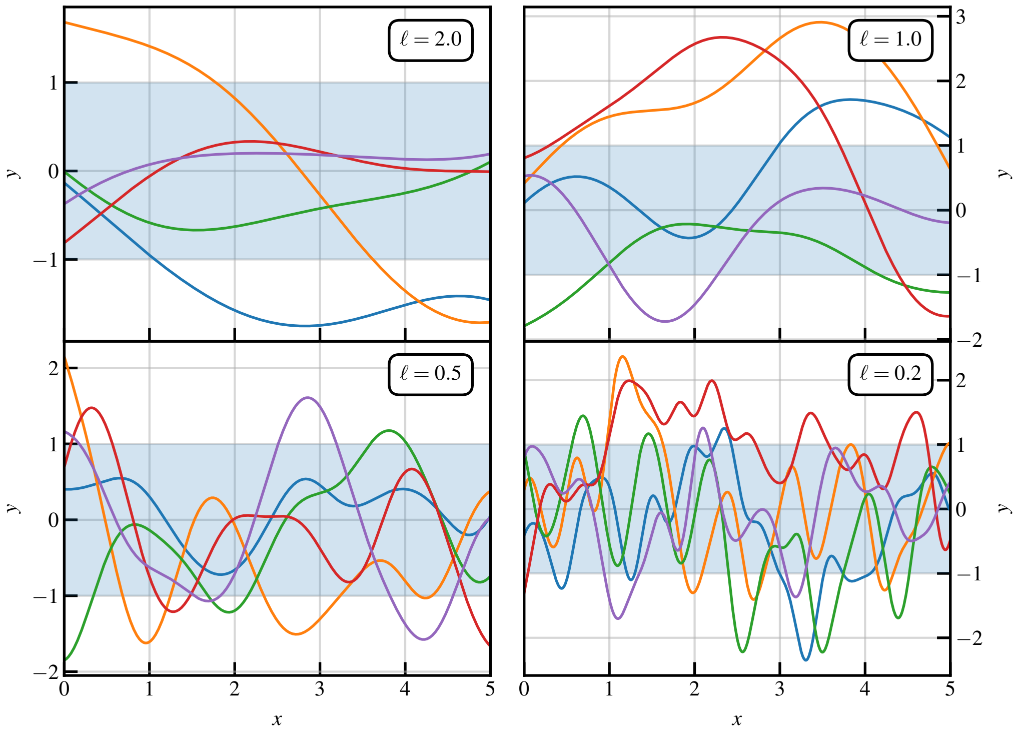

Figure 6.1: Colors online. Examples of the structure of *prior* functions for various choices of the ℓ parameter. The shaded area represents the 1σ confidence interval.

function generating the data (dotted line) is simply $y = \sin(x)$. We perform the *experiment* and we extract five data points, indicated by crosses on the figure, which are used to build the likelihood for $f(x)$; by combining this likelihood with the prior, we then obtain a *posterior* distribution of $f(x)$. The *GP mean* (solid line) here represents the average of all possible samples from the posterior distribution of $f(x)$ passing through the data $\mathcal{Y}$ (crosses), i.e. the average prediction. Since both the likelihood and the prior are Gaussian, so is the posterior. The GP mean is smooth, and interpolates all data points exactly. Outside the input domain, it approaches 0. As we would expect, the quality of the regression is greatest where there is more data available, in this case $0 \leq x \leq 4$.

Also shown in Fig. 6.2 are confidence intervals, here representing 2σ ($\approx 95\%$). The confidence intervals are 0 at each data point, and grow in between data points, more rapidly so when data are further apart. At the edges of the input domain, they also grow rapidly, representing the uncertainty in extrapolation, until reaching a maximum of 2η. A very important aspect of the GP is the confidence intervals: in this case, we see that the *true* function does not always match the GP mean, but $\approx 95\%$ of the true function falls within the 2σ interval.

The GP is fully characterised by the two kernel parameters; clearly some sets of these

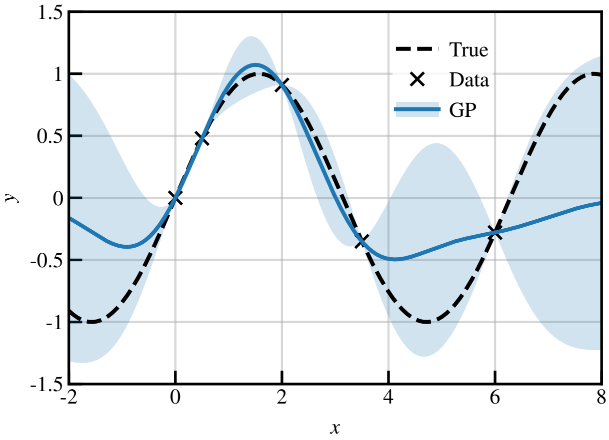

Figure 6.2: Demonstration of Gaussian process regression. The true function is $y = \sin(x)$, and the data points are at $x = \{0, 0.5, 2, 3.5, 6\}$. The solid line represents the GP mean, and the shaded areas give the 2σ confidence intervals. The optimised kernel parameters are $\eta^2 = 0.602$, $\ell = 1.063$. See text for details.

parameters lead to better regression. For example, if ℓ is smaller than the typical data spacing, the GP mean will approach 0 in between data points, making it useless for interpolation (overfitting); if η^2 is too large, the size of the confidence intervals will be overestimated. These parameters are determined using likelihood maximisation as discussed in Ref. [GW19].

6.2 Nuclear masses

Nuclear mass models are used to reproduce the nuclear binding energies of all known nuclei, ≈ 3200 [Wan17]. Within the mass database we distinguish two types of data: nuclear masses that have been directly measured (≈ 2400) and the extrapolated ones (≈ 750). The latter are obtained by indirect mass measurements and we will use them to benchmark our extrapolations.

For this investigation, we use the Duflo-Zucker mass model[DZ95]; it consists of 10 terms (DZ10 model), and is able to reproduce all known masses with a root mean square deviation of $\sigma_{\text{RMS}} \approx 0.6$ MeV [Pas20]. The details of the model are not relevant for our work here; DZ10 was chosen since it is commonly used, and because it is not very CPU intensive. We refer the reader to Refs. [Zuk11; Qi15] for a detailed discussion on the different terms in the model.

The parameters of the DZ10 model have been adjusted in Ref. [Pas20] using the block-bootstrap (BB) method [Pas19], yielding the optimal parameter set $\mathbf{a}^0$. The reason for using BB is that it provides robust error bars on the parameters that take into account correlations between them [Lah99; BB17].

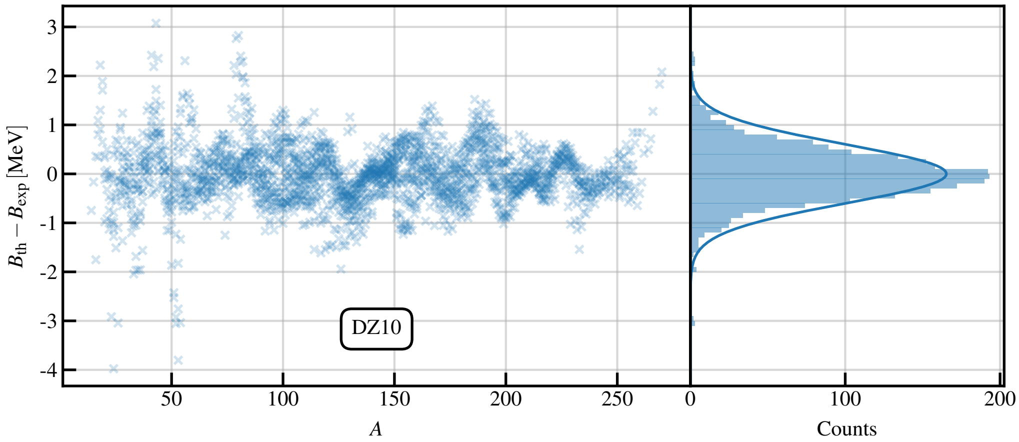

Figure 6.3: Left panel: residuals as a function of nucleon number A for the DZ10 model, for measured masses. In the right panel are the same residuals shown as a histogram, with a Gaussian fit overlaid (for which the mean is fixed to 0, and the standard deviation to that of the residuals). See text for details.

The assumption used to fit DZ10, as with any other mass model, is that the experimental binding energies $B_{\mathrm{exp}}(N, Z)$ are equal to the theoretical ones $B_{\mathrm{th}}(N, Z|\mathbf{a}^0)$ up to a Gaussian error $\varepsilon(N, Z)$:

$$B_{\mathrm{exp}}(N, Z) = B_{\mathrm{th}}(N, Z|\mathbf{a}^0) + \varepsilon(N, Z), \tag{6.3}$$

where $B_{\mathrm{th}}(N, Z)$ is the binding energy calculated using DZ10. In Fig. 6.3, we illustrate the residuals for DZ10 as a function of the nucleon number $A = N + Z$. One clearly sees that these residuals show structure, thus indicating the presence of some missing *physics* that is not properly accounted for by the model. In the right panel of the same figure, we plot the same residuals as a histogram, and we draw a Gaussian with mean 0 and width fixed to the RMS of the residuals. The height of the Gaussian is fitted on the residuals.

A more detailed statistical test can be performed on these residuals to verify that they do not follow a regular Gaussian distribution — see for example Refs. [CP20; Pas20] for more details — but for the current discussion a qualitative analysis is sufficient.

Having identified that there is room to improve the accuracy of the model, the most natural option to take is to add new terms [Qi15]. For example, a version of the Duflo-Zucker model with 33 parameters is available. Although the RMS reduces to ≈ 300 keV, the extra terms appear poorly constrained [Qi15], and therefore the model is unsuitable for extrapolation. We refer the reader to Ref. [NV16] for a detailed discussion on poorly constrained parameters.

Instead of explicitly *creating* new terms for a given mass model, we can take advantage of machine learning methods. For example, in Refs. [UPP16; Pas20], the authors have adjusted a NN on the residuals of the DZ10 model in order to reduce the discrepancy between theory and experiment. The NN is able to reduce this discrepancy to a typical RMS of ≈ 350 keV [Pas20].

NNs are often very complex models, with several hundred free parameters. As discussed in [Neu18], a Gaussian process represents a valid alternative to a NN; the main advantages are the very small number of adjustable parameters, as discussed in Sec. 6.1, and the superior performance on the database of nuclear masses when compared with a NN [Neu18]. Moreover, the procedure using GPs outlined in this thesis can be easily generalised to any other mass model that has non-Gaussian-distributed residuals. We leave this for a future extension of this work.

6.2.1 Augmenting the DZ10 model with a GP

Having introduced the GP in Sec. 6.1, we now apply it to the case of nuclear masses. As done in Ref. [Neu18], we consider the same kernel given in Eq. 6.1, but now in the 2D case, meaning there are now three adjustable parameters. We also use a fourth parameter σ_n, named the *nugget*. The use of the nugget carries several advantages, including numerical stability [Nea97], and improved predictions [GL12]. Its use is standard where the data have statistical error bars, as is the case with nuclear masses. The kernel we use is then given by

$$k_{\mathrm{RBF}}(x,x') = \eta^2 \exp\left[-\frac{(N-N')^2}{2\rho_N^2} - \frac{(Z-Z')^2}{2\rho_Z^2}\right] + \sigma_n^2 \delta_{xx'}, \tag{6.4}$$

where in the present case $x = (N, Z)$, and η^2, ρ_Z, ρ_N are the adjustable parameters. Following Ref. [Neu18], ρ_N and ρ_Z are interpreted as correlation lengths in the neutron and proton directions, while η^2 gives the strength of the correlation between neighbouring nuclei.

The addition of the nugget means that the GP mean now does not necessarily pass directly through each data point, and that the 1σ confidence intervals only shrink to a minimum of σ_n. After performing preliminary investigation using a full minimisation with all four parameters, we have found that the optimal value is $\sigma_n = 0.2$ MeV. We have decided to fix this value, in order to simplify the analysis of the posterior distribution.

The main role of the nugget is to avoid over-fitting, which manifests itself via a correlation length smaller than the typical separation of the data. For example, setting $\sigma_n = 0$ MeV would lead to a perfect reproduction of the data, but the resulting model would be totally useless;

it would not be able to perform any kind of prediction, since the correlation lengths would be smaller than one (i.e., the separation the nuclear mass data). The nugget gives us an extra flexibility in identifying the residual correlations between the data as discussed in Ref. [PC20]. For a more detailed discussion on GP and the role of the nugget we refer to Ref. [Neu18].

As discussed previously, we adjust the parameters of the GP on the residuals of the DZ10 model (shown in Fig. 6.3). The parameters η, ρ_N, ρ_Z are determined through maximising the likelihood for the GP. See Ref. [GW19] for details. In Fig. 6.4, we illustrate the posterior distribution of the parameters in the form of a corner plot. The distributions were obtained with Markov chain Monte-Carlo (MCMC) sampling [Gey92]. We used the *emcee* [For13] Python package, which makes use of an *affine-invariant ensemble sampler* [GW10], using 32 chains of 2000 samples each. This incurred a significant computational cost — almost 40 hours on a 32-core compute node — as well as having a large memory requirement of ≈ 0.8 TB). The main computational bottleneck is the repeated inversion of a correlation matrix during the optimisation of the GP parameters; this optimisation procedure takes place at every MCMC step. The matrix contains n^2 elements, where $n \approx 2400$ is the number of measured nuclei. We have therefore implemented a Python code to run the sampling on a computing cluster.

Fig. 6.4 illustrates the shapes of the distributions around the optimal parameter set, and it provides us with the error bars for the parameters and information about their correlations. In this case we see that all parameters are very well determined by the residuals data, and a weak correlation is observed between η and ρ_N, and between η and ρ_Z.

A very interesting result is that the two correlation lengths $\rho_{N,Z}$ are as large as, or greater than, 2. This means that, if we know the residual for a nucleus with mass number A, we can infer properties of the nucleus with $A \pm 2$. This result is in agreement with the analysis done in Ref. [Pas20], which was based on the auto-correlation coefficients.

We now construct our new model for B_{th} (appearing in Eq. 6.3) as $B_{\text{th}} = B_{\text{DZ10}} - GP$, which we name *DZ10-GP*. In Fig. 6.5 we compare the residual distributions for the DZ10 and DZ10-GP models for measured masses. We see that the RMS of the DZ10 model has been greatly reduced. The RMS of the DZ10-GP model is $\sigma = 178$ keV, which at the moment is probably among the lowest values ever obtained using a mass model fitted on all the available masses, with a total of $10 + 4 = 14$ adjustable parameters.

In Fig. 6.6, we illustrate the residuals obtained from the DZ10-GP model as a function of mass number A. We clearly see that the GP has been able to capture the missing physics of the DZ10 model, in particular smoothing out the spikes observed in Fig. 6.3. We observe that the maximum discrepancy between theory and experiment is now always lower than 1 MeV, and the structure observed in Fig. 6.3 has now disappeared, with the new residuals exhibiting behaviour

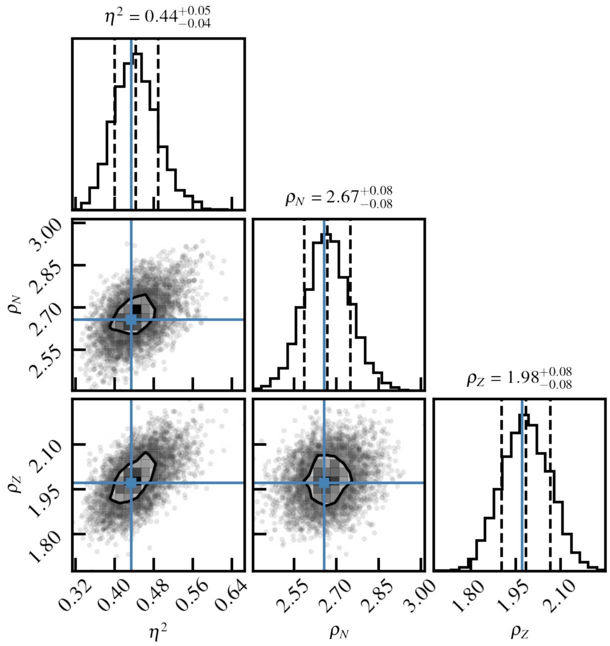

Figure 6.4: Posterior distributions of GP parameters obtained through MCMC sampling. The horizontal and vertical solid lines indicate the optimal parameter values obtained by maximising the likelihood. The vertical dotted lines on each 1D histogram indicate the mean and 1σ confidence intervals obtained through the MCMC sampling. See text for details.

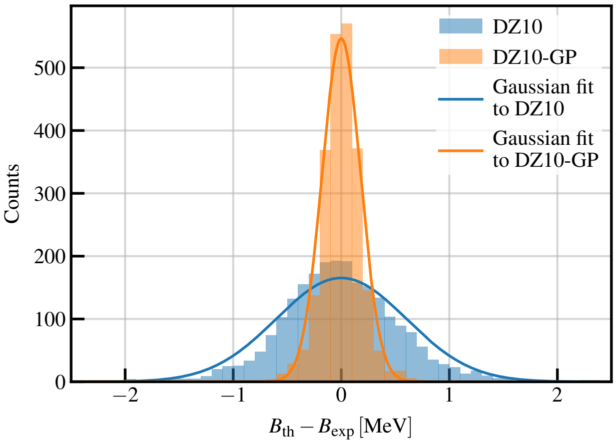

Figure 6.5: Distributions of the residuals for the DZ10 and DZ10-GP models, for measured masses. Gaussian fits to the residuals are also shown, with the mean fixed to 0, and the standard deviation to that of the residuals. See text for details.

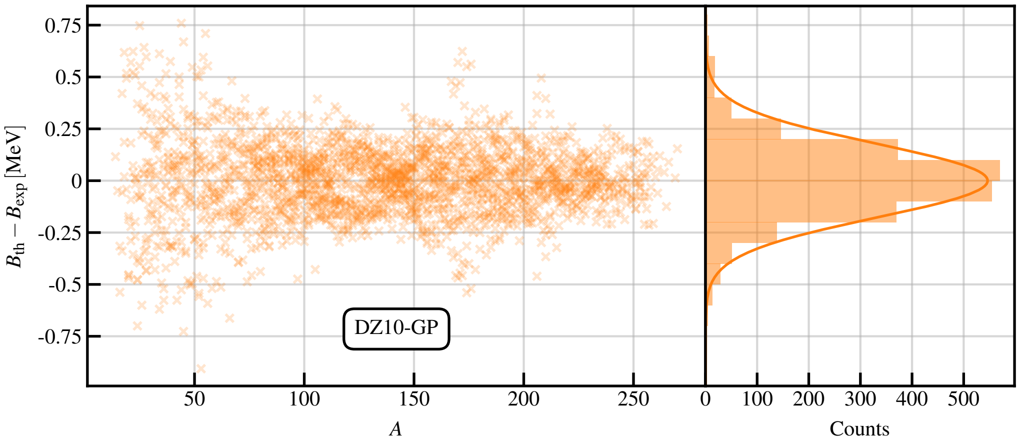

Figure 6.6: The same as Fig. 6.3, but for the DZ10-GP model. See text for details.

close to white noise. The presence or not of white noise in the model may represent a lower bound on the accuracy one can achieve with a theoretical model, as discussed in Ref. [Bar05]; we leave such an interesting analysis for a future investigation.

6.2.2 Extrapolation using the DZ10-GP model

Having created the DZ10-GP model, we now benchmark its extrapolations on the set of ≈ 750 nuclear masses obtained via indirect measurements [Wan17]. The results are presented in Fig. 6.7. The original DZ10 model gives an RMS of 1.426 MeV; the inclusion of GP corrections reduces the RMS to 1.100 MeV. It is worth noting that some outliers are still present. We have checked that the six nuclei with a residual larger than 6 MeV are all in the region of super-heavy nuclei with $Z \geq 108$.

Since the main goal of this chapter is the study of the outer crust of a neutron star, in Fig. 6.8 we illustrate in great detail the evolution of the residuals for two isotopic chains — copper and nickel — that play a very important role in determining the composition of the outer crust [Wol13].

We observe that the original DZ10 model reproduces fairly well the data in the middle of the isotopic chains, and that it tends to give large discrepancies at the edges. Even the inclusion of the statistical error bars of DZ10 are not enough to explain such a discrepancy. We refer the reader to Ref. [Pas20] for a detailed discussion on how these error bars have been obtained. On the contrary, the use of the GP helps to flatten out the discrepancies, and produces predictions very close to the data in the extrapolated region. By considering the experimental and the theoretical error bars, we observe that our DZ10-GP model reproduces these data reasonably

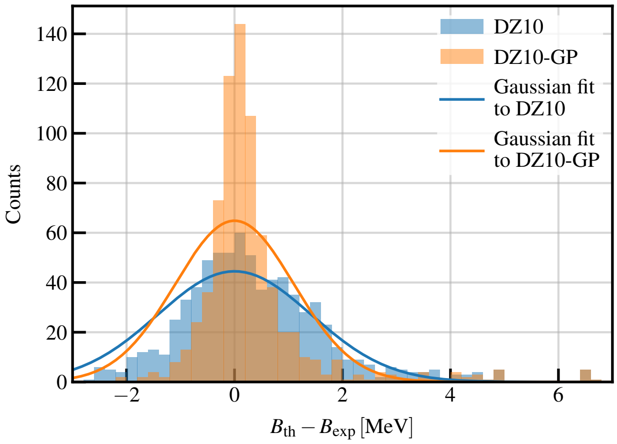

Figure 6.7: Same as Fig. 6.5, but for extrapolated masses. See text for details.

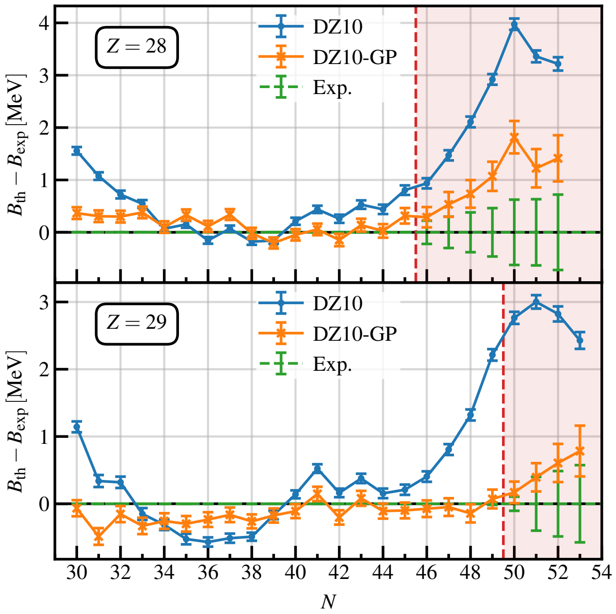

Figure 6.8: Residuals for the DZ10 and DZ10-GP models, for the $Z = 28$ and $Z = 29$ isotopic chains. The vertical dashed lines represent the transition from nuclei used for training to nuclei for which predictions are made. See text for details.

	1σ	2σ	3σ
Full chart	61%	88.8%	96.2%
$50 \leq A \leq 150$	59.2%	89.1%	97.3%
$20 \leq Z \leq 50$	54.4%	84.1%	95.5%

Table 6.1: Percentage of nuclei included in the total error bars for the DZ10-GP model for three different sectors of the nuclear chart

well. The error bars of the DZ-GP model have been obtained using a *näive* approach, i.e., summing in quadrature the statistical error bars of the original DZ model and the confidence intervals of the GP model.

As done in Ref. [Pas20], we validate the error bars by comparing with experimental masses. In particular, we expect that 68% of known masses differ from the model prediction no more than $\sigma = \sigma_{\text{th}} + \sigma_{\text{exp}}$, where σ_{th} is the theoretical error bar of the DZ10-GP model and σ_{exp} is the experimental error bar. By increasing the error bar by a factor of 2 and 3 we should obtain 95% and 99.7% of experimental binding energies falling into the interval.

From Table 6.1, we observe that most of the nuclei fall within these error bars as expected, although we still underestimate in some relevant regions of the chart, such as $20 \leq Z \leq 50$ which is important for outer crust calculations. This discrepancy may be a sign of other contributions to the error bar that were not taken into account here, for example correlations between the DZ10 and GP error bars.

In Fig. 6.9, we show the evolution, along two isotopic chains, of the GP's contribution to binding energy. We see that these contributions drop to 0 as the neutron-rich region is approached. On the same figure, we also report the evolution of a 1σ error bar provided by the GP. As discussed previously, we notice that the error bars grow towards the neutron drip-line, where we have little or no available data to constrain the GP.

From Fig. 6.9, we observe that the confidence interval provided by the GP model at large values of N becomes constant and equal to η. This means that at very large extrapolations, the GP error bar is most likely underestimating. In this case, the model error bar should become larger and be the dominant source of error. See for example [Gao13].

This behaviour can be understood from the value of the GP's correlation length for neutrons, $\rho_N = 2.67$: by construction the GP predictions tend to the mean of the data, in this case 0, after $\approx$ 2-3 times ρ_N. This means that the GP will be effective in describing extrapolated neutron-rich nuclei with at most $\approx$ 8-10 neutrons more than the last nucleus in our training set. This is clearly only a rule of thumb, but it is enough to cover most of the extrapolated nuclei that are present in the outer crust [PGC11] of a neutron star. For nuclei further away

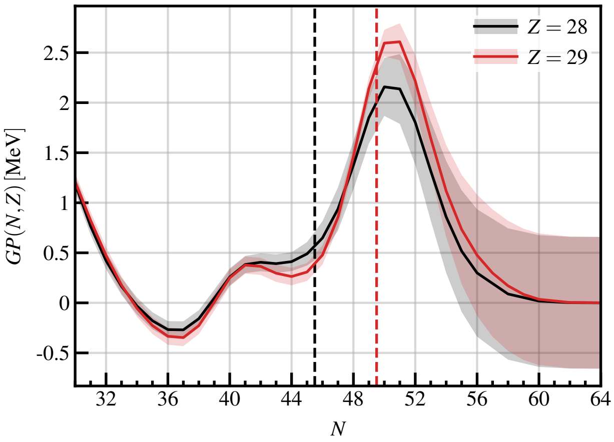

Figure 6.9: GP correction for $Z = 28$ and $Z = 29$. The vertical dashed lines represent the transition from nuclei used for training to nuclei for which predictions are made. The shaded ares represent the GP 1σ error bars. See text for details.

from the known data-set, the extrapolation is governed by the underlying nuclear mass model, i.e., the DZ10 model. This is not the case for other approaches, for example with NNs that can introduce an additional trend on top of the model. Such a trend is difficult to predict *a priori*, and it may be strongly biased by the training method. See Ref. [PC20] for a more detailed discussion. In the recent work of Neufcourt et al. [Neu19], extrapolation to the neutron drip line was carried out using a combination of GPs with Bayesian model averaging, to avoid model dependence. This would be an interesting avenue to explore in future work.

6.2.3 Comparison with AME2020

Having trained and developed the DZ10-GP model on the AME2016 database [Wan17], we now benchmark the predictions against the newly published AME2020 database [Hua21]. Between the 2016 and 2020 database, we have 74 new isotopes.

In Fig. 6.10, we report the distribution of the residuals for the new isotopes presented in AME2020 database, apart from the Cu measurements already published in Ref. [Wel17]. We observe that the RMS of the original DZ10 model for these new data is $\sigma_{\text{DZ10}} = 701$ keV, while for the DZ10-GP model it is $\sigma_{\text{DZ10-GP}} = 299$ keV. Notice that in this case we do not re-adjust the GP model over the new data. This test clearly proves that the GP is not over-fitting the data, but it was really able to grasp a signal in the residuals and is therefore capable of performing extrapolations in regions in the proximity of the data set used for the training. We also observed that 50% of the new isotopes fall within the error bars of the original DZ10-GP model. This value is slightly lower than what is reported in Table 6.1, but still reasonable

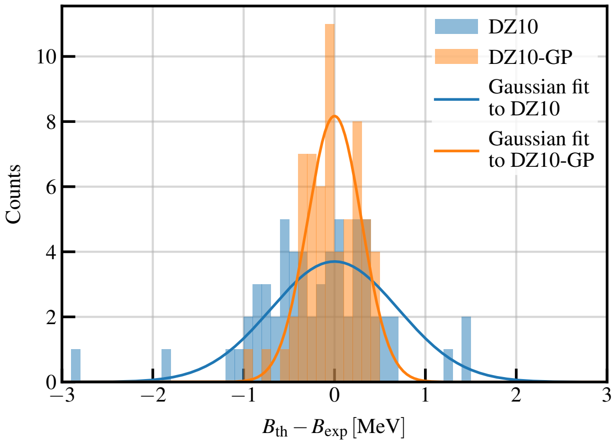

Figure 6.10: Distributions of the residuals for the DZ10 and DZ10-GP models, for new masses presented in AME2020 [Hua21]. Gaussian fits to the residuals are also shown, with the mean fixed to 0, and the standard deviation to that of the residuals. See text for details.

compared to the expected 68%.

6.3 Outer crust composition

To determine the chemical composition of the outer crust, we minimise the Gibbs free energy per particle, which is defined as [BPS71]

$$g = \mathcal{E}_{\rm nuc}(N,Z) + \mathcal{E}_e(A,Z) + \mathcal{E}_l(A,Z) + \frac{P}{\rho_b}\,, \tag{6.5}$$

where ρ_b is the baryonic density. The three terms $\mathcal{E}_{\rm nuc}, \mathcal{E}_e, \mathcal{E}_l$ are the *nuclear*, *electronic* and *lattice* energies per nucleon respectively [Bas15]. The pressure P arises only from lattice and electron contributions as $P = P_L + P_e$. For more details, we refer to Ref. [BPS71], where the entire formalism has been discussed in great detail.

The novelty of the current approach is in the treatment of the nuclear term, which takes the form

$$\mathcal{E}_{\rm nuc}(N,Z) = \frac{Zm_p + Nm_n}{A} - \frac{\mathcal{B}(N,Z)}{A} \tag{6.6}$$

where $m_{p(n)}$ is the mass of the proton (neutron) and $\mathcal{B}$ is the nuclear binding energy given by the mass model. In this work, we use the mass model DZ10-GP as discussed in Sec. 6.1. The

DZ10			DZ10-GP		
P_{max} [MeV fm^{-3}]	N	Z	P_{max} [MeV fm^{-3}]	N	Z
$3.30 \cdot 10^{-10}$	30	26	$3.30 \cdot 10^{-10}$	30	26
$4.36 \cdot 10^{-8}$	34	28	$4.36 \cdot 10^{-8}$	34	28
$3.56 \cdot 10^{-7}$	36	28	$3.56 \cdot 10^{-7}$	36	28
$4.02 \cdot 10^{-7}$	38	28	$4.02 \cdot 10^{-7}$	38	28
$1.03 \cdot 10^{-6}$	50	36	$1.03 \cdot 10^{-6}$	50	36
$5.59 \cdot 10^{-6}$	50	34	$5.59 \cdot 10^{-6}$	50	34
$1.76 \cdot 10^{-5}$	50	32	$5.59 \cdot 10^{-6}$	50	32
			$1.77 \cdot 10^{-5}$	50	30
$1.58 \cdot 10^{-4}$	50	28	$3.22 \cdot 10^{-5}$	50	28
$1.82 \cdot 10^{-4}$	82	42	$1.21 \cdot 10^{-4}$	82	42
$3.31 \cdot 10^{-4}$	82	40	$1.81 \cdot 10^{-4}$	82	40
$4.83 \cdot 10^{-4}$	82	38	$3.31 \cdot 10^{-4}$	82	38
$4.86 \cdot 10^{-4}$	82	36	$4.84 \cdot 10^{-4}$	82	36

Table 6.2: Composition of the outer crust of a NS using the DZ10 and DZ10-GP mass models. In the first and fourth columns we report the maximum value of pressure at which the nucleus is found using the minimisation procedure. The horizontal line separates the measured and extrapolated masses reported in AME2016 [Wan17].

composition predicted by the mass models is given in Table 6.2. By comparing the DZ10-GP results with those obtained using only the DZ10 model, we observe some discrepancies in the extrapolated region at low P. In particular, we notice that the improved mass model (DZ10-GP) predicts the existence of ^{80}Zn, that is not considered in the original DZ10 model. At higher P, the two mass models give very similar results. This is simple to understand since, as discussed in Sec. 6.1, the GP correction tends to 0 for large extrapolations, as seen in Fig. 6.9.

Since our goal is to obtain the statistical uncertainties of the equation of state, we perform a simple Monte-Carlo sampling of the error bars of our DZ10-GP model (under a Gaussian assumption). We generate 10^4 new mass tables, and we use them to calculate the composition of the outer crust.

Using a *frequentist* approach [Bar89], we define the existence probability of each nucleus as the ratio of the number of times a given nucleus appears in the various EoS at a given pressure, divided by the total number of mass tables. See Ref. [Pas20] for more details.

In Fig. 6.11, we show the evolution of the existence probability for each nucleus in the

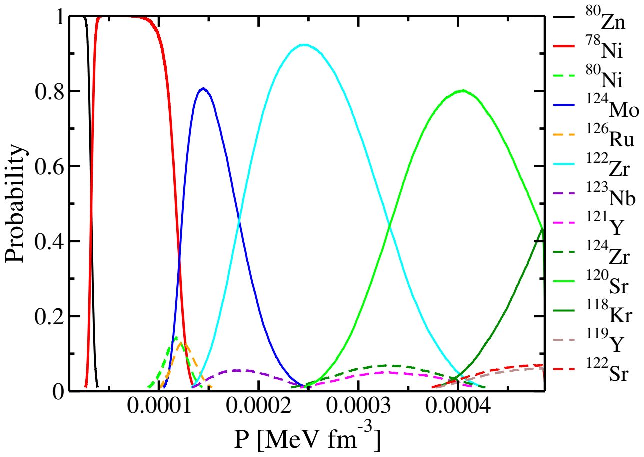

Figure 6.11: Colors online. Existence probability of a given nucleus within the outer crust as a function of the pressure, obtained via a Monte-Carlo sampling using the DZ10-GP mass table. See text for details.

outer crust as a function of the pressure of the star. We notice that, as confirmed by other authors [PGC11], the favourable configurations are those close to the neutron shell closures at N = 50 and N = 82. However, due to the large error bars, there is a non-negligible probability for several nuclei to be present within the outer crust.

It is interesting to compare the composition obtained with DZ10-GP with the predictions of other mass models, since different mass models may yield different extrapolations. We have selected two popular mass models currently used in astrophysics: BSk20 [PGC11] and BPS [Sha15]. The results are reported in Fig. 6.12. The shaded area on the figure represents all the possible EoS obtained using the Monte-Carlo procedure detailed above using a 1% cut-off on the existence probability. We observe that the results obtained with the different procedure are in good agreement with the DZ10-GP model once the error bars are properly taken into account. It is important to notice that the transition region between the outer and inner crust is mainly governed by the mass model and not by the GP correction. As a consequence, we may expect different results using various models as shown in Fig. 6.12.

Using the same data set, we also define a statistical uncertainty for the EoS: by counting the 10^4 EoS built before, we define the 68%, 95%, and 99% quantiles of the counts, i.e., 1σ, 2σ and 3σ deviations, under the assumption that the errors follow a Gaussian distribution. The results are presented in Fig. 6.13. We observe that the largest uncertainties are located close to the transition from N=50 to N=82 at $P \approx 1.2 \times 10^{-4}$MeV fm^{-3} and approaching the transition to the inner crust at $P \approx 5 \times 10^{-4}$MeV fm^{-3}.

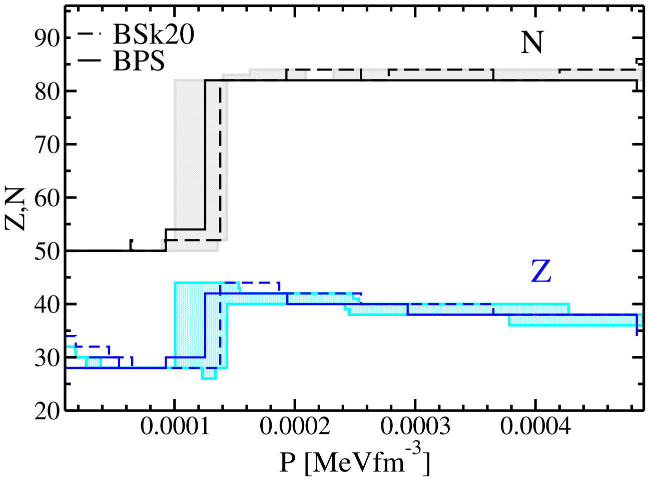

Figure 6.12: Variations of Z and N with pressure in the outer crust for the BSk20 and BPS models. The shaded area represent the regions covered by the Monte-Carlo procedure detailed in the text and obtained using the DZ10-GP model. See text for details.

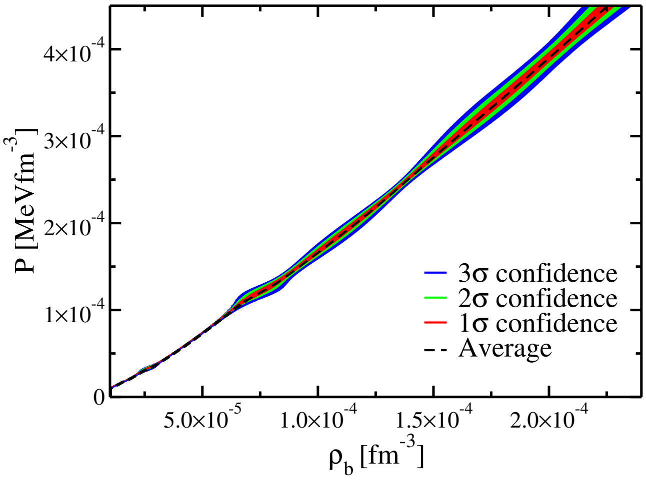

Figure 6.13: Equation of state, including statistical uncertainties, of the outer crust of a NS, calculated using the DZ10-GP mass model. See text for details.

6.4 Summary

By using a Gaussian process fitted to the residuals of the Duflo-Zucker mass model, we have been able to create a mass model with a global RMS of less than 200 keV. The resulting DZ10-GP model has the major advantage of having a very limited amount of parameters (ten in the original DZ model plus four for the GP), but it is also one of the very few mass models equipped with error bars [GC14; Qi15].

We have then applied the resulting mass model to study the composition of the outer crust of a neutron star, paying particular attention to the role of statistical errors and how they propagate to the final EoS. Following the methodology presented in Ref. [Pas20], we have defined an existence probability of a nucleus within the crust. Such a quantity helps us to identify the possible accuracy problems related to our model, and it may help in prioritising future experimental proposals to further improve our knowledge of the crust of a neutron star.

Chapter 7

Conclusions and perspectives

Despite neutron stars first having been predicted almost a century ago, we still lack a unified equation of state that can accurately describe all layers of the star. Regarding the crust, the Skyrme functionals typically used are not very varied, and so many aspects of the outer and inner crust compositions are far form being determined. In the case of the neutron-rich inner crust, there had previously been no conclusive link between a Skyrme functional's properties and its predictions in this system. For the outer crust, calculations have historically almost always been carried out using mass models with no associated uncertainties.

In this PhD project, we have offered several improvements to the models used to describe both the inner and outer crusts of neutron stars, while also identifying key deficiencies in previously used models.

After outlining the various energy contributions to an inner crust WS cell in Chapter 2, we carried out the first direct comparison between the ETFSI and HFB methods in Chapter 3 in the inner crust. We found that the densities and fields from ETFSI calculations can reproduce the HFB densities and fields very well, but that there is a significant energy discrepancy. We identified this as coming from a lack of neutron pairing in the ETFSI formalism.

In Chapter 4, we introduced for the first time a method to include neutron pairing correlations in an inner crust calculation. The resulting ETFSI+pairing model was remarkably successful at closing the gap observed in Chapter 3 between previous ETFSI work (which only included proton pairing) and HFB calculations (where all pairing correlations are included naturally).

In Chapter 5, we performed a systematic investigation of the inner crust, with the new ETFSI+pairing model, in order to shed light on the persistence of nuclear clusters with $Z = 40$. We demonstrated clearly that, when using a Skyrme functional to model the inner crust, the results are largely influenced by PNM EoS of the particular functional. This has a simple explanation, in that a large fraction of the inner crust matter is well-approximated by a uniform neutron gas. We concluded that, if one wishes to have a unified EoS that accurately describes the inner crust, it must have an accurate PNM EoS at sub-nuclear densities, i.e. well constrained by ab-initio calculations.

In the modelling of the outer crust, it is necessary to have use a nuclear mass model which can be relied upon in extrapolation beyond the region of measured nuclei. In Chapter 6, presented a novel data-driven Bayesian approach to augmenting existing mass models. Using Gaussian process (GP) regression, we developed a new mass model — DZ10-GP — which has a very low RMS error on measured nuclei of less than 200 keV, and the ability to extrapolate robustly several isotopes beyond the neutron drip line. It also produced modified predictions of the sequence of nuclei predicted to lie in the outer crust. Crucially, DZ10-GP is one of the few existing nuclear mass models to come equipped with error bars, which are necessary to quantify our degree of belief about the presence of an isotope in the outer crust.

There are a number of paths along which the research from this project could continue. For the inner crust, there is now a need to include the effects of finite temperature in this new framework that accounts for neutron pairing, to have a complete model for (non-accreting) NSs. This adds a third dimension to the parameter space to be explored; GPs also provide an promising opportunity to be used as emulators [Pas17; She19], to make this investigation computationally tractable. There is also a clear need to even more rigorously determine how the properties of Skyrme functionals affect the predictions in the inner crust. In particular, the relative importance of properties such as the PNM EoS, the symmetry energy coefficient J, the slope of the symmetry energy L, and even the surface energy, should be analysed quantitatively.

For the outer crust, several other statistical and machine learning techniques have been proposed to augment existing mass models. It would be very insightful to compare them directly, and assess which are most suited to extrapolation, and whether they can provide meaningful errors as GP regression can do.

Appendix A

BSk functionals

Here we give extra details for the BSk family of forces, which have extra terms and parameters (BSk18 and newer) when compared to standard Skyrme forces, and which have their own prescription for treating pairing correlations (BSk16 and newer).

A.1 The generalised Skyrme interaction for BSk forces

The generalised Skyrme interaction with new extra terms was introduced in Ref. [CGP09] as a means to model neutrons stars so that they are stable against polarisation and collapse. These terms come with six new parameters: $t4, x4, \beta, t5, x5, \gamma$. The full interaction is given by

$$\begin{aligned}
v_{i,j} = {} & t_0(1+x_0P_\sigma)\delta(\vec{r}_{ij}) \\
& + \frac{1}{2}t_1(1+x_1P_\sigma)\frac{1}{\hbar^2}\left[p_{ij}^2\delta(\vec{r}_{ij}) + \delta(\vec{r}_{ij})p_{ij}^2\right] \\
& + t_2(1+x_2P_\sigma)\frac{1}{\hbar^2}\vec{p}_{ij}\cdot\delta(\vec{r}_{ij})\vec{p}_{ij} \\
& + \frac{1}{6}t_3(1+x_3P_\sigma)\rho(\vec{r})^\sigma\delta(\vec{r}_{ij}) \\
& + \frac{i}{\hbar^2}W_0(\sigma_\mathbf{i}+\sigma_\mathbf{j})\cdot\vec{p}_{ij}\times\delta(\vec{r}_{ij})\vec{p}_{ij} \\
& + \frac{1}{2}t_4(1+x_4P_\sigma)\frac{1}{\hbar^2}\left[p_{ij}^2\rho(\vec{r})^\beta\delta(\vec{r}_{ij}) + \delta(\vec{r}_{ij})\rho(\vec{r})^\beta p_{ij}^2\right] \qquad \text{extra terms} \\
& + t_5(1+x_5P_\sigma)\frac{1}{\hbar^2}\vec{p}_{ij}\cdot\rho(\vec{r})^\gamma\delta(\vec{r}_{ij})\vec{p}_{ij}, \qquad \text{extra terms}
\end{aligned} \tag{A.1}$$

where the displacement between two particles i and j is $\vec{r}_{ij} = \vec{r}_i - \vec{r}_j$, $\vec{r} = (\vec{r}_i + \vec{r}_j)/2$, their relative momentum $\vec{p}_{ij} = -i\hbar(\vec{\nabla}_i - \vec{\nabla}_j)/2$, P_σ is the spin exchange operator, and $\rho(\vec{r}) = \rho_n(\vec{r}) + \rho_p(\vec{r})$ is the total density, where $\rho_n(\vec{r})$ and $\rho_p(\vec{r})$ are the neutron and proton densities.

The full energy density functional is then

$$
\begin{aligned}
\mathcal{E}_{\text{Sky}} = {} & \sum_{q=n,p} \frac{\hbar^2}{2M_q}\tau_q + \frac{1}{2}t_0\left[\left(1+\frac{1}{2}x_0\right)\rho^2 - \left(\frac{1}{2}+x_0\right)\sum_{q=n,p}\rho_q^2\right] \\
& + \frac{1}{4}t_1\Bigg[\left(1+\frac{1}{2}x_1\right)\left(\rho\tau+\frac{3}{4}(\nabla\rho)^2\right) \\
& \qquad - \left(\frac{1}{2}+x_1\right)\sum_{q=n,p}\left(\rho_q\tau_q+\frac{3}{4}(\nabla\rho_q)^2\right)\Bigg] \\
& + \frac{1}{4}t_2\Bigg[\left(1+\frac{1}{2}x_2\right)\left(\rho\tau-\frac{1}{4}(\nabla\rho)^2\right) \\
& \qquad + \left(\frac{1}{2}+x_2\right)\sum_{q=n,p}\left(\rho_q\tau_q-\frac{1}{4}(\nabla\rho_q)^2\right)\Bigg] \\
& + \frac{1}{12}t_3\rho^\sigma\left[\left(1+\frac{1}{2}x_3\right)\rho^2 - \left(\frac{1}{2}+x_3\right)\sum_{q=n,p}\rho_q^2\right] \\
& + \frac{1}{4}t_4\Bigg[\left(1+\frac{1}{2}x_4\right)\left(\rho\tau+\frac{3}{4}(\nabla\rho)^2\right) && \text{extra terms} \\
& \qquad - \left(\frac{1}{2}+x_4\right)\sum_{q=n,p}\left(\rho_q\tau_q+\frac{3}{4}(\nabla\rho_q)^2\right)\Bigg]\rho^\beta && \text{extra terms} \\
& + \frac{\beta}{8}t_4\Bigg[\left(1+\frac{1}{2}x_4\right)\rho(\nabla\rho)^2 && \text{extra terms} \\
& \qquad - \left(\frac{1}{2}+x_4\right)\vec{\nabla}\rho\cdot\sum_{q=n,p}\rho_q\vec{\nabla}\rho_q\Bigg]\rho^{\beta-1} && \text{extra terms} \\
& + \frac{1}{4}t_5\Bigg[\left(1+\frac{1}{2}x_5\right)\left(\rho\tau-\frac{1}{4}(\nabla\rho)^2\right) && \text{extra terms} \\
& \qquad + \left(\frac{1}{2}+x_5\right)\sum_{q=n,p}\left(\rho_q\tau_q-\frac{1}{4}(\nabla\rho_q)^2\right)\Bigg]\rho^\gamma && \text{extra terms} \\
& + \frac{1}{2}W_0\left(\vec{J}\cdot\vec{\nabla}\rho + \sum_{q=n,p}\vec{J}_q\cdot\vec{\nabla}\rho_q\right).
\end{aligned}
\tag{A.2}
$$

Note that we exclude J^2 terms in all work in this thesis project.

A.2 Fields

Here we given the fields for the extended BSk Skyrme forces. The central field U_q is

$$
\begin{aligned}
U_q = {} & t_0 \left[\left(1+\frac{1}{2}x_0\right)\rho-\left(\frac{1}{2}+x_0\right)\rho_q\right] \\
& +\frac{1}{4}t_1\left[\left(1+\frac{1}{2}x_1\right)\left(\tau-\frac{3}{2}\nabla^2\rho\right)-\left(\frac{1}{2}+x_1\right)\left(\tau_q-\frac{3}{2}\nabla^2\rho_q\right)\right] \\
& +\frac{1}{4}t_2\left[\left(1+\frac{1}{2}x_2\right)\left(\tau+\frac{1}{2}\nabla^2\rho\right)+\left(\frac{1}{2}+x_2\right)\left(\tau_q+\frac{1}{2}\nabla^2\rho_q\right)\right] \\
& +\frac{1}{12}t_3\Bigg[\left(1+\frac{1}{2}x_3\right)(2+\sigma)\rho^{\sigma+1} \\
& \qquad -\left(\frac{1}{2}+x_3\right)\left(2\rho^\sigma\rho_q+\sigma\rho^{\sigma-1}\sum_{q'=n,p}\rho_{q'}^2\right)\Bigg] \\
& +\frac{1}{8}t_4\Bigg[\left(1+\frac{1}{2}x_4\right)\rho^{\beta-1}\Big\{2(1+\beta)\rho\tau && \text{extra terms} \\
& \qquad -(2\beta+3)\Big(\frac{1}{2}\beta(\nabla\rho)^2+\rho\nabla^2\rho\Big)\Big\} && \text{extra terms} \\
& \qquad +\left(\frac{1}{2}+x_4\right)\rho^{\beta-2}\Big\{3\beta\rho\vec{\nabla}\rho\cdot\vec{\nabla}\rho_q+3\rho^2\nabla^2\rho_q && \text{extra terms} \\
& \qquad -2\rho^2\tau_q+\beta(\beta-1)\rho_q(\nabla\rho)^2+\beta\rho\rho_q\nabla^2\rho && \text{extra terms} \\
& \qquad -\frac{1}{2}\beta\rho\sum_{q'=n,p}\Big[(\nabla\rho_{q'})^2+4\rho_{q'}\tau_{q'}-2\rho_{q'}\nabla^2\rho_{q'}\Big]\Big\}\Bigg] && \text{extra terms} \\
& +\frac{1}{4}t_5\Bigg[\left(1+\frac{1}{2}x_5\right)\left\{(1+\gamma)\rho\tau+\frac{1}{4}\gamma(\nabla\rho)^2+\frac{1}{2}\rho\nabla^2\rho\right\} && \text{extra terms} \\
& \qquad +\left(\frac{1}{2}+x_5\right)\Big\{\rho\tau_q+\frac{1}{2}\rho\nabla^2\rho_q && \text{extra terms} \\
& \qquad +\gamma\sum_{q'=n,p}\left\{\rho_{q'}\tau_{q'}-\frac{1}{4}(\nabla\rho_{q'})^2\right\}+\frac{1}{2}\gamma\vec{\nabla}\rho\cdot\vec{\nabla}\rho_q\Big\}\Bigg]\rho^{\gamma-1} && \text{extra terms} \\
& -\frac{W_0}{2}\left(\nabla\vec{J}+\nabla\vec{J}_q\right)+\delta_{q,p}\left(V_{\text{Coul}}+V_{\text{Coul,pe}}\right).
\end{aligned}
\tag{A.3}
$$

The spin-orbit field W_q remains unchanged from the standard form (Eq. 2.6). The effective mass M_q^* is given by

$$
\begin{aligned}
\frac{\hbar^2}{2M_q^*} = \frac{\hbar^2}{2M_q} &+ \frac{1}{4}t_1\left[\left(1+\frac{1}{2}x_1\right)\rho - \left(\frac{1}{2}+x_1\right)\rho_q\right] \\
&+ \frac{1}{4}t_2\left[\left(1+\frac{1}{2}x_2\right)\rho + \left(\frac{1}{2}+x_2\right)\rho_q\right] \\
&+ \frac{1}{4}t_4\left[\left(1+\frac{1}{2}x_4\right)\rho - \left(\frac{1}{2}+x_4\right)\rho_q\right]\rho^\beta \qquad \text{extra terms} \\
&+ \frac{1}{4}t_5\left[\left(1+\frac{1}{2}x_5\right)\rho + \left(\frac{1}{2}+x_5\right)\rho_q\right]\rho^\gamma . \qquad \text{extra terms}
\end{aligned}
\tag{A.4}
$$

A.3 Coupling constants

Here we give the Skyrme coupling constants $C_q^{\rho,\tau}$, needed to calculate the pressure in the inner crust. Note that the expression for C_1^ρ was given with a typo in Eq. A30b of Ref. [CGP09] and in Eq. B30b of Ref. [Pea12].

$$
C_0^\rho(\rho) = \frac{3}{8}t_0 + \frac{3}{48}t_3\rho^\sigma \tag{A.5a}
$$

$$
C_1^\rho(\rho) = -\frac{1}{4}t_0\left(\frac{1}{2}+x_0\right) - \frac{1}{24}t_3(\frac{1}{2}+x_3)\rho^\sigma \tag{A.5b}
$$

$$
\begin{aligned}
C_0^\tau(\rho) = &\frac{3}{16}t_1 + \frac{1}{4}t_2\left(\frac{5}{4}+x_2\right) \\
&+ \frac{3}{16}t_4\rho^\beta + \frac{1}{4}t_5\left(\frac{5}{4}+x_5\right)\rho^\gamma \qquad \text{extra terms}
\end{aligned}
\tag{A.5c}
$$

$$
\begin{aligned}
C_1^\tau(\rho) = &-\frac{1}{8}t_1\left(\frac{1}{2}+x_1\right) + \frac{1}{8}t_2\left(\frac{1}{2}+x_2\right) \\
&- \frac{1}{8}t_4\rho^\beta\left(\frac{1}{2}+x_4\right) + \frac{1}{8}t_5\rho^\gamma\left(\frac{1}{2}+x_5\right) \qquad \text{extra terms}
\end{aligned}
\tag{A.5d}
$$

A.4 PNM quantities

Here we give expressions for various PNM quantities for the full extended Skyrme interaction. As in the previous section, all terms containing t_4, t_5 etc. are the new extra terms.

The energy per particle in pure neutron matter with neutron density n_n is

$$\begin{aligned}
e_{\mathrm{PNM}}(n_n) = {} & \frac{3\hbar^2}{10M_n}k_{\mathrm{F}n}^2(n_n)^2 + \frac{1}{4}t_0(1-x_0)n_n + \frac{3}{40}t_1(1-x_1)n_n k_{\mathrm{F}n}^2(n_n)^2 \\
& + \frac{9}{40}t_2(1+x_2)n_n k_{\mathrm{F}n}^2(n_n)^2 + \frac{1}{24}t_3(1-x_3)n_n^{\sigma+1} \\
& + \frac{3}{40}t_4(1-x_4)n_n^{\beta+1}k_{\mathrm{F}n}^2(n_n)^2 + \frac{9}{40}t_5(1+x_5)n_n^{\gamma+1}k_{\mathrm{F}n}^2(n_n)^2,
\end{aligned} \tag{A.6}$$

where $k_{\mathrm{F}n}^2(n_n) = (3\pi^2 n_n)^{1/3}$. The energy per particle in symmetric nuclear matter with density n is

$$\begin{aligned}
e_{\mathrm{SNM}}(n) = {} & \frac{3\hbar^2}{10M}k_{\mathrm{F}}^2(n) + \frac{3}{8}t_0 n + \frac{3}{80}\left[3t_1 + t_2(5+4x_2)\right] n k_{\mathrm{F}}^2(n) + \frac{1}{16}t_3 n^{\sigma+1} \\
& + \frac{9}{80}t_4\rho^{\beta+1}k_{\mathrm{F}}^2(n) + \frac{3}{80}t_5(5+4x_5)\rho^{\gamma+1}k_{\mathrm{F}}^2(n),
\end{aligned} \tag{A.7}$$

where $k_{\mathrm{F}}(n) = (3\pi^2 n/2)^{1/3}$. The symmetry energy is

$$\begin{aligned}
\mathcal{S}(n) = {} & \frac{\hbar^2}{6M}k_{\mathrm{F}}^2(n) - \frac{1}{8}t_0(2x_0+1)n \\
& + \frac{1}{24}\left[-3t_1x_1 + t_2(4+5x_2)\right] n k_{\mathrm{F}}^2(n) - \frac{1}{48}t_3(1+2x_3)n^{\sigma+1} \\
& - \frac{1}{8}t_4x_4 n^{\beta+1}k_{\mathrm{F}}^2(n) + \frac{1}{24}t_5(4+5x_5)n^{\gamma+1}k_{\mathrm{F}}^2(n),
\end{aligned} \tag{A.8}$$

where here n denotes the density of symmetric nuclear matter, and M is defined as

$$\frac{2}{M} = \frac{1}{M_n} + \frac{1}{M_p}. \tag{A.9}$$

The symmetry coefficient J is given by $\mathcal{S}(n_0)$. Finally, the slope of the symmetry energy at saturation is

$$\begin{aligned}
L = {} & \frac{\hbar^2}{3M}k_{F0}^2 - \frac{3}{8}t_0(2x_0+1)n_0 \\
& + \frac{5}{24}\left[-3t_1x_1 + t_2(4+5x_2)\right] n_0 k_{F0}^2 - \frac{\sigma+1}{16}t_3(1+2x_3)n_0^{\sigma+1} \\
& - \frac{5+3\beta}{8}t_4x_4 n_0^{\beta+1}k_{F0}^2 + \frac{5+3\gamma}{24}t_5(4+5x_5)n_0^{\gamma+1}k_{F0}^2,
\end{aligned} \tag{A.10}$$

where $k_{\mathrm{F}0} = (3\pi^2 n_0/2)^{1/3}$.

A.5 Pairing formalism

The BSk forces BSk16 and newer use an effective contact pairing interaction. The pairing gap Δ_q at a given asymmetry is given by

$$\Delta_q(\rho_n,\rho_p) = \Delta_{\rm SM}(\rho)(1-|\eta|) \pm \Delta_{\rm NM}(\rho_q)\eta\frac{\rho_q}{\rho}, \tag{A.11}$$

i.e., an interpolation between the gap in symmetric nuclear matter $\Delta_{\rm SM}$ and in pure neutron matter $\Delta_{\rm NM}$. The asymmetry parameter $\eta = (\rho_n - \rho_p)/\rho$, and the upper (lower) sign is for $q = n(p)$. These gaps have parametric forms, given by

$$\Delta_{\rm SM}(\rho) = \theta(k_{\rm m} - k_{\rm F})\,\Delta_0 \frac{k_{\rm F}^3}{k_{\rm F}^2 + k_1^2}\frac{(k_{\rm F} - k_2)^2}{(k_{\rm F} - k_2)^2 + k_3^2}, \tag{A.12a}$$

$$\Delta_{\rm NM}(\rho_n) = \theta(k_{\rm m} - k_{{\rm F}n})\,\Delta_0 \frac{k_{{\rm F}n}^2}{k_{{\rm F}n}^2 + k_1^2}\frac{(k_{{\rm F}n} - k_2)^2}{(k_{{\rm F}n} - k_2)^2 + k_3^2}, \tag{A.12b}$$

where θ is the Heaviside unit step function, and the various parameters are summarised in Table A.1. Note that for BSk16 [CGP08], a simpler ansatz was used for Δ_q, that it just takes the form of Eq. A.12b, with the parameters given in Table A.2.

	Δ_0	k_1	k_2	k_3	$k_{\rm m}$
SM	133.779	0.943146	1.52786	2.11577	1.51
NM	14.9003	1.18847	1.51854	0.639489	1.52

Table A.1: Parameters of the analytical pairing gaps for symmetric nuclear matter and pure neutron matter (Eq. A.12), for BSk17 onwards.

	Δ_0	k_1	k_2	k_3	$k_{\rm m}$
NM	910.603	1.38297	1.57068	0.905237	1.57

Table A.2: Parameters of the analytical pairing gap for BSk16 (Eq. A.12b).

In infinite nuclear matter, the pairing interaction strength is [Cha10],

$$v^{\pi q}[\rho_n,\rho_p] = -\frac{8\pi^2}{I_q(\rho_n,\rho_p)}\left(\frac{\hbar^2}{2M_q^*(\rho_n,\rho_p)}\right)^{3/2}, \tag{A.13}$$

where

$$I_q(\rho_n, \rho_p) = \int_0^{\mu_q+\varepsilon_\Lambda} \mathrm{d}\xi \frac{\sqrt{\xi}}{\sqrt{(\xi-\mu_q)^2 + \Delta_q(\rho_n,\rho_p)^2}}, \tag{A.14}$$

where ε_Λ is the pairing cutoff parameter. In Eq. A.14, $\mu_q = \lambda_q - U_q$ is the reduced chemical potential. However, I_q has an analytical form, derived in Ref. [Cha10], given by

$$I_q = \sqrt{\varepsilon_{\mathrm{F}q}} \left[2\log\left(\frac{2\varepsilon_{\mathrm{F}q}}{\Delta_q}\right) + \Lambda\left(\frac{\varepsilon_\Lambda}{\varepsilon_{\mathrm{F}q}}\right)\right], \tag{A.15}$$

where

$$\Lambda(x) = \log(16x) + 2\sqrt{1+x} - 2\log\left(1+\sqrt{1+x}\right) - 4. \tag{A.16}$$

For very low densities, it is necessary to use the low-density limiting form for Eq. A.14 of $2\sqrt{\varepsilon_\Lambda}$.

When performing BCS calculations for protons, it is necessary to use Eqs. A.13 and A.15, and the parametric form of Δ_q given in Eq. A.11. It is also necessary to multiply by the BSk pairing parameter f_p^+ for an even number of protons, and f_p^- for an odd number.

For treating neutron pairing in the LDA approximation, we only need the pairing gap in infinite nuclear matter, given by

$$\Delta_q = \Delta_q^{(0)} \exp\left(\frac{1}{2}\Lambda(y)\right) y^{-1/2}, \tag{A.17}$$

where $y = \varepsilon_\Lambda / \varepsilon_{\mathrm{F}q}$, and $\Delta_q^{(0)}$ is given by

$$\Delta_q^{(0)} = 2\sqrt{\varepsilon_{\mathrm{F}q}\varepsilon_\Lambda} \exp\left(\frac{2\pi^2\hbar^2}{\upsilon^{\pi\, q} M_q^* k_{\mathrm{F}q}}\right) \tag{A.18}$$

N.B. In Eqs. A.13 and A.18 BSk16 uses the effective mass, but it is set to 1 for BSk17 onwards [GCP09a].

Appendix B

Extended Thomas-Fermi densities

Here we give the remainder of the full expressions for the contributions to the kinetic and spin current densities, in the case of spherical symmetry, in the extended Thomas-Fermi method at 4th-order. Instead of using these explicit forms for the densities and integrating them numerically to obtain their energy contributions, it is also possible to use integrated forms of these expressions which only contain derivatives up to 2nd-order, as discussed in Ref. [Pea12] (the expressions are provided in Appendix A of Ref. [BGH85]). Using instead the explicit forms, as done in this work, only incurs a tiny discrepancy in energy, which is most significant at the very lowest densities, as shown in Chapters 3 and 4.

B.1 Kinetic densities

In order to make benchmarks with previous ETF calculations (see Appendix C), it is useful to separate out the contributions to the kinetic density τ_q at 4th-order that do and do not arise from the spin-orbit interaction [BB02]. The 4th-order contribution to the kinetic density, containing no spin-dependence, is given by

$$
\begin{aligned}
\tau_q^{(4)}[\rho] = {} & (3\pi^2)^{-2/3}\frac{\rho_q^{1/3}}{4320}\left\{\frac{24}{\rho_q}\left[\rho_q^{(4)} + \frac{4}{r}\rho_q^{'''}\right] - \frac{8}{\rho_q^2}\left[11\rho_q^{'''}\rho_q^{'} + 7(\rho_q^{''})^2 + \frac{36}{r}\rho_q^{''}\rho_q^{'} - \frac{1}{r^2}(\rho_q^{'})^2\right]\right. \\
& + \frac{8}{3\rho_q^3}\left[81\rho_q^{''}(\rho_q^{'})^2 + \frac{70}{r}(\rho_q^{'})^3\right] - \frac{96}{\rho_q^4}(\rho_q^{'})^4 - \frac{36}{f_q}\left[f_q^{(4)} + \frac{4}{r}f_q^{'''}\right] + \frac{18}{f_q^2}\left[4f_q^{'''}f_q^{'} + \right. \\
& \left. + 3(f_q^{''})^2 + \frac{4}{r}f_q^{''}f_q^{'} - \frac{4}{r^2}(f_q^{'})^2\right] - \frac{144}{f_q^3}f_q^{''}(f_q^{'})^2 + \frac{54}{f_q^4}(f_q^{'})^4 + \frac{12}{f_q\rho_q}\left[3f_q^{'}\rho_q^{'''} + 2f_q^{''}\rho_q^{''}\right. \\
& \left. - 2f_q^{'''}\rho_q^{'} + \frac{6}{r}f_q^{'}\rho_q^{''} - \frac{4}{r}f_q^{''}\rho_q^{'} + \frac{2}{r^2}f_q^{'}\rho_q^{'}\right] + \frac{12}{f_q^2\rho_q}\left[f_q^{'}f_q^{''}\rho_q^{'} - 2(f_q^{'})^2\rho_q^{''} - \frac{2}{r}(f_q^{'})^2\rho_q^{'}\right] \\
& \left. - \frac{4}{f_q\rho_q^2}\left[11f_q^{''}(\rho_q^{'})^2 + 32f_q^{'}\rho_q^{'}\rho_q^{''} + \frac{26}{r}f_q^{'}(\rho_q^{'})^2\right] + \frac{30}{f_q^2\rho_q^2}(f_q^{'})^2(\rho_q^{'})^2 + \frac{260}{3f_q\rho_q^3}f_q^{'}(\rho_q^{'})^3\right\}, \qquad \text{(B.1)}
\end{aligned}
$$

where a prime represents the derivative with respect to r.

The spin-dependent part is given by

$$
\begin{aligned}
\tau_q^{(4)\mathrm{so}}[\rho] = {} & (3\pi^2)^{-2/3}\left(\frac{mW_0}{\hbar^2}\right)^2\frac{\rho_q^{1/3}}{4f_q^2}\left\{\frac{1}{2}\left[2A_q'A_q''' + (A_q'')^2 + \frac{6}{r}A_q'A_q'' - \frac{1}{r^2}(A_q')^2\right]\right. \\
& - \frac{A_q'}{f_q}\left[f_q''A_q' + 2f_q'A_q'' + \frac{2}{r}f_q'A_q'\right] + \frac{3(A_q')^2}{4f_q^2}\left[2(f_q')^2 - (\frac{mW_0}{\hbar^2})^2(A_q')^2\right] \\
& \left. + \frac{\rho_q'A_q'}{3f_q\rho_q}\left[f_q(A_q'' + \frac{1}{r}A_q') - f_q'A_q'\right]\right\}, \qquad \text{(B.2)}
\end{aligned}
$$

where $A_q = \rho + \rho_q$.

B.2 Spin current densities

The 4th-order contribution to the spin current density is given by

$$
\begin{aligned}
\vec{J}_q^{(4)}[\rho] = {} & (3\pi^2)^{-2/3}\frac{mW_0}{\hbar^2}\frac{\rho_q^{1/3}}{4f_q}\left\{-\left[A_q''' + \frac{2}{r}A_q'' - \frac{2}{r^2}A_q'\right] + \frac{1}{f_q}\left[f_q''A_q' + f_q'A_q'' + \frac{1}{r}f_q'A_q'\right]\right. \\
& \left. - \frac{A_q'}{f_q^2}\left[(f_q')^2 - (\frac{mW_0}{\hbar^2})^2(A_q')^2\right] - \frac{\rho_q'}{3f_q\rho_q}\left[f_q(A_q'' + \frac{1}{r}A_q') - f_q'A_q'\right]\right\}. \qquad \text{(B.3)}
\end{aligned}
$$

Below we give the contributions to the divergence of the spin current density div$\vec{J}_q[\rho]$, which is needed for the central potentials U_q. The 2nd-order contribution is

$$\mathrm{div}\vec{J}_q^{(2)} = -\frac{2m}{\hbar^2}\frac{1}{f_q}\left[\rho_q \mathrm{div}\vec{W}_q + (\vec{\nabla}\rho_q \cdot \vec{W}_q) - \frac{\rho_q}{f_q}(\vec{\nabla} f_q \cdot \vec{W}_q)\right], \tag{B.4}$$

where $\mathrm{div}\vec{W}_q$ is equivalent to $\frac{W_0}{2}\left(\frac{2}{r}A'_q + A''_q\right)$. The 4th-order contribution is

$$\begin{aligned}
\mathrm{div}\vec{J}_q^{(4)}[\rho] = {} & (3\pi^2)^{-2/3}\frac{mW_0}{\hbar^2}\frac{\rho_q^{1/3}}{4f_q}\Bigg\{-(A_q^{(4)} + \frac{4}{r}A'''_q) + \frac{1}{f_q}\left[f'''_q A'_q + 2f''_q A''_q + 2f'_q A'''_q\right. \\
& \left. + \frac{5}{r}f'_q A''_q + \frac{3}{r}f''_q A'_q - \frac{1}{r}f'_q A'_q\right] - \frac{1}{f_q^2}\left[3(f'_q)^2 A''_q + 4f'_q f''_q A'_q + \frac{4}{r}(f'_q)^2 A'_q\right. \\
& \left. -(\frac{mW_0}{\hbar^2})^2 (A'_q)^2\left(3A''_q + \frac{2}{r}A'_q\right)\right] + \frac{3}{f_q^3}f'_q A'_q\left[(f'_q)^2 - (\frac{mW_0}{\hbar^2})^2 (A'_q)^2\right] \\
& -\frac{1}{3\rho_q}\left[2\rho'_q A'''_q + \rho''_q A''_q + \frac{1}{r}\rho''_q A'_q + \frac{5}{r}\rho'_q A''_q + \frac{1}{r^2}\rho'_q A'_q\right] + \frac{1}{3f_q\rho_q}\left[3f'_q\rho'_q A''_q\right. \\
& \left. + f'_q\rho''_q A'_q + 2f''_q\rho'_q A'_q + \frac{4}{r}f'_q\rho'_q A'_q\right] - \frac{1}{3f_q^2\rho_q}\rho'_q A'_q\left[3(f'_q)^2 - (\frac{mW_0}{\hbar^2})^2 (A'_q)^2\right] \\
& + \frac{2}{9\rho_q^2}(\rho'_q)^2\left(A''_q + \frac{1}{r}A'_q\right) - \frac{2}{9f_q\rho_q^2}f'_q(\rho'_q)^2 A'_q\Bigg\}.
\end{aligned} \tag{B.5}$$

Appendix C

Benchmarks for ETF calculations

Here we make comparisons with results of the detailed investigation of the ETF method carried out by Bartel and Bencheikh [BB02]. All calculations were performed for a ^{208}Pb nucleus, using the Skyrme force SkM* [KTB80; Bar82], using the matter densities ρ_q extracted from Fig. 1 in Ref. [BB02]. The 2nd-order expressions for kinetic and spin current densities are given in Chapter 3, and all 4th-order expressions in Appendix B.

In Fig. C.1, we show the order-by-order contributions to the kinetic density for neutrons τ_n, as shown in Fig. 2 (a) of Ref. [BB02]. For the sake of visibility, the 4th-order contributions are multiplied by 10.

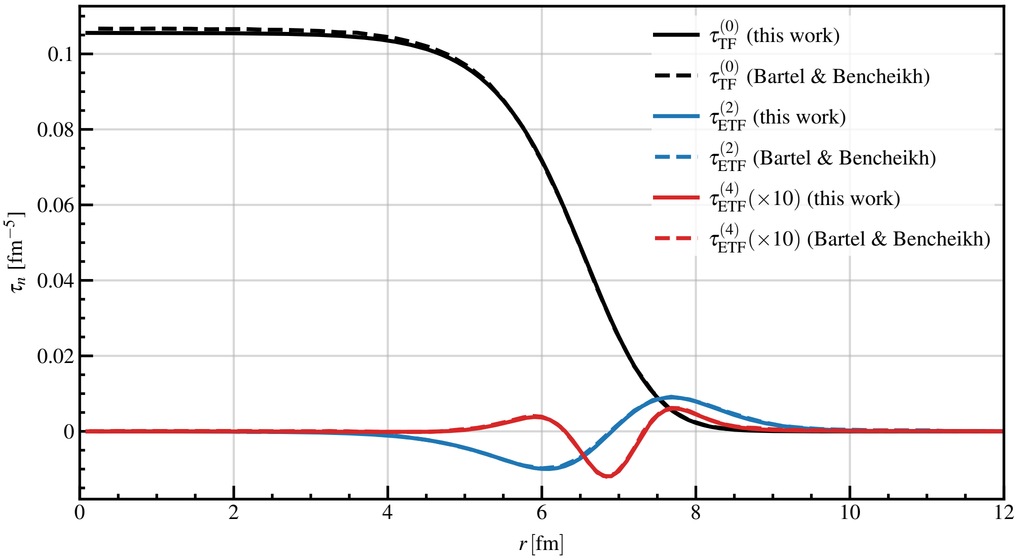

Figure C.1: Comparison between the kinetic density contributions for neutrons from our work and from Fig. 2 (a) of Ref. [BB02], for ^{208}Pb using SkM*.

In Fig. C.2, we show the different components of τ_n at 2nd-order, as shown in Fig. 2 (b) of Ref. [BB02]. The discrepancy observed for the terms with gradients of f is likely due to a plotting error in Ref. [BB02].

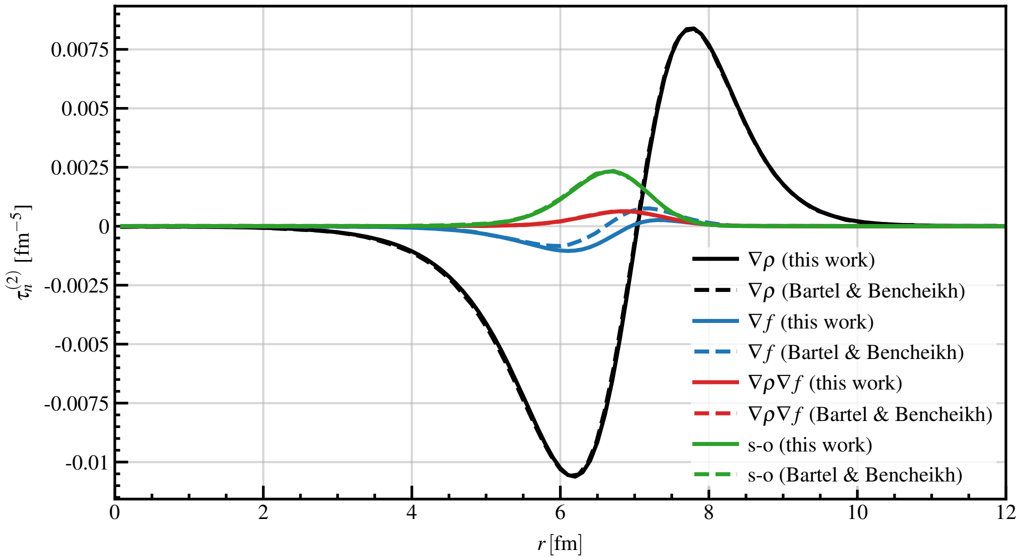

Figure C.2: Comparison between the 2nd-order kinetic density components for neutrons τ_n from our work and from Fig. 2 (b) of Ref. [BB02], for ^{208}Pb using SkM*. Black lines represent terms containing gradients of ρ, blue lines for terms with gradients of f, red lines for terms containing gradients of both ρ and f, and green lines for spin-orbit terms.

In Fig. C.3, we show the different components of τ_n at 4th-order, as shown in Fig. 2 (c) of Ref. [BB02].

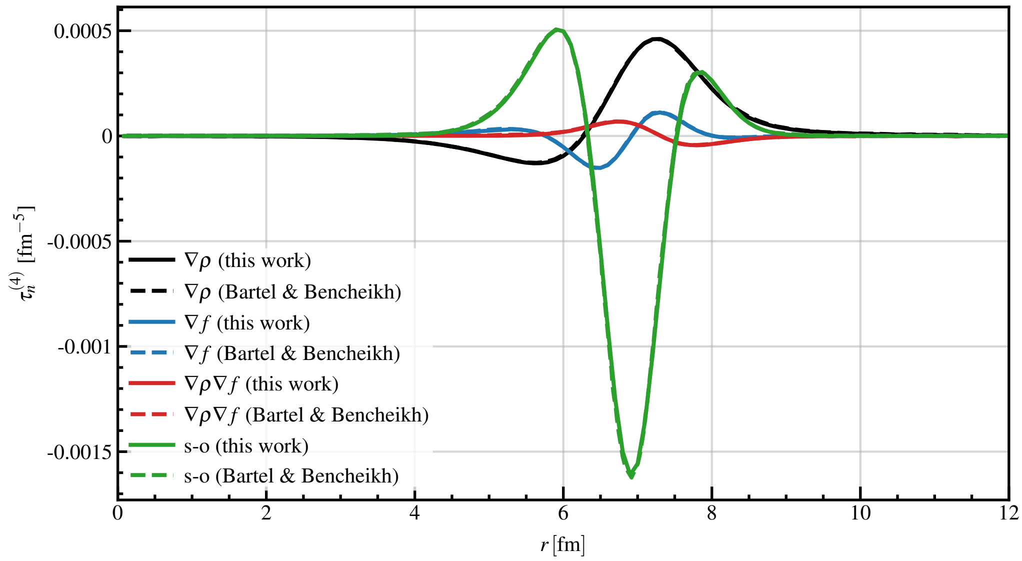

Figure C.3: Same as Fig. C.2, but for 4th-order contributions, where the comparison is made with Fig. 2 (c) of Ref. [BB02].

In Fig. C.4, we show the order-by-order contributions to the spin current density for neutrons $\vec{J}_n$, as shown in Fig. 3 of Ref. [BB02].

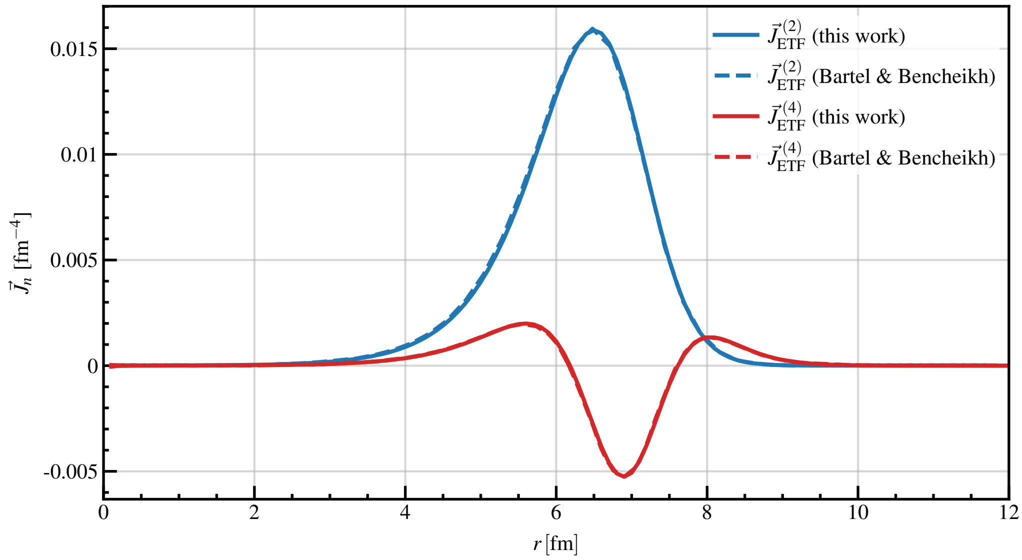

Figure C.4: Comparison between the spin current density contributions for neutrons $\vec{J}_n$ from our work and from Fig. 3 of Ref. [BB02], for ^{208}Pb using SkM*.

Appendix D

Neutron condensation energy

We derive here the expression for the pairing condensation energy per particle for PNM, given in Eq. 4.8. For simplicity we set $\hbar = m = 1$. Since we use a contact pairing interaction, the pairing gap in PNM is momentum-independent. The single-particle energy, relative to the effective chemical potential, is given by

$$\xi_k = \frac{k^2}{2} + U - \mu, \tag{D.1}$$

where μ is the effective chemical potential, i.e., scaled respect to the HF mean field, and k is the particle momentum. The quasi-particle energy is then given by

$$E_k = \sqrt{\xi_k^2 + \Delta^2}, \tag{D.2}$$

where Δ is the pairing gap. We write the energy per unit volume of a superfluid system as

$$E(\mu, \Delta) = \int_0^\Lambda \frac{k^2}{2\pi^2} \left[\frac{-\Delta^2}{2E_k} + \frac{k^2}{2} \left(1 - \frac{\xi_k}{E_k} \right) \right] dk, \tag{D.3}$$

where Λ is the cut-off momentum. After integration, the first term of the integrand of Eq. D.3 yields the pairing energy density, and the second term the kinetic energy density corrected by the depletion of the occupation factors [RS80]. The kinetic energy density per unit volume of a non-superfluid system with the same density is

$$E_0 = \frac{k_\mathrm{F}^5}{10\pi^2}. \tag{D.4}$$

In a superfluid system with a given μ, the density can be calculated as

$$\rho(\mu, \Delta) = \int_0^\Lambda \frac{k^2}{2\pi^2} \left(1 - \frac{\xi_k}{E_k} \right) dk. \tag{D.5}$$

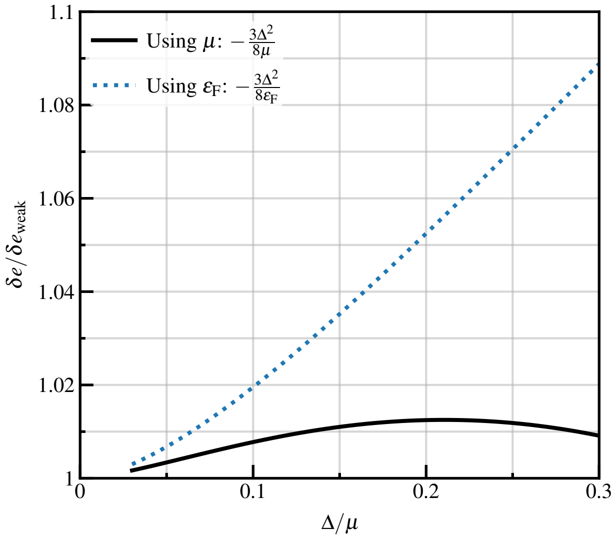

Figure D.1: Solid black line shows the ratio of the weak-coupling approximation for $\delta\epsilon$ (Eq. D.7) to the exact result (Eq. D.6). The blue dotted line shows the same, but with μ in Eq. D.7 replaced by ε_F.

We now estimate the true energy gain per particle, in terms of the quantities expressed in Eqs. D.3–D.5 as

$$\delta\epsilon = \left(\frac{E - E_0}{\rho}\right). \tag{D.6}$$

The previous equation can be simplified in the weak coupling limit, where $\Delta \ll \mu$. In this case, the change in the kinetic energy density and in the density of the system is negligible, so Eq. D.6 reduces to

$$\delta\epsilon_\mathrm{weak} = -\frac{3\Delta^2}{8\mu}. \tag{D.7}$$

This expression is in agreement with the one given in Ref. [PVB97]. Eq. D.7 can be further simplified by approximating the chemical potential μ with the Fermi energy $\varepsilon_\mathrm{F} = (3\pi^2\rho)^{2/3}/2$.

In Fig. D.1, we compare the validity of the weak coupling limit by comparing the result exact result given by Eq. D.6 and the two different approximations. It shows the ratio of Eq. D.6 to Eq. D.7, using either μ or ε_F in the denominator of Eq. D.7. We vary the ratio Δ/μ over the range 0.03–0.3.

We observe that the weak coupling limit gives a very nice reproduction of the total energy correction with an error of $\approx$1% over relevant range of variation. In the regions of the star where $\Delta \ll \mu$, the use of ε_F instead of μ is then fully justified. The weak coupling approximation with ε_{F} tends to give a larger error especially in the low-density region of the star, but such an error is still less than 10%, and is probably less important than other approximations in the ETFSI method [CGM19].

Bibliography

[Abb17] BP Abbott et al. “GW170817: observation of gravitational waves from a binary neutron star inspiral”. In: *Physical Review Letters* 119.16 (2017), p. 161101.

[Alf07] M Alford et al. “Quark matter in compact stars?” In: *Nature* 445.7125 (2007), E7–E8.

[ASA05] BK Agrawal, S Shlomo, and VK Au. “Determination of the parameters of a Skyrme type effective interaction using the simulated annealing approach”. In: *Physical Review C* 72.1 (2005), p. 014310.

[Ath04] S Athanassopoulos et al. “Nuclear mass systematics using neural networks”. In: *Nuclear Physics A* 743.4 (2004), pp. 222–235.

[Ath05] S Athanassopoulos et al. *Nuclear mass systematics by complementing the Finite Range Droplet Model with neural networks.* Nov. 30, 2005. arXiv: `nucl-th/0511088`.

[Avo07] P Avogadro et al. “Quantum calculation of vortices in the inner crust of neutron stars”. In: *Physical Review C* 75.1 (2007), p. 012805.

[Bal05] M Baldo et al. “The role of superfluidity in the structure of the neutron star inner crust”. In: *Nuclear Physics A* 750.2-4 (2005), pp. 409–424.

[Bar05] J Barea et al. “Nuclear masses set bounds on quantum chaos”. In: *Physical Review Letters* 94.10 (2005), p. 102501.

[Bar82] J Bartel et al. “Towards a Better Parametrisation of Skyrme-like Effective Forces: A Critical Study of the SkM Force”. In: *Nuclear Physics A* 386.1 (Sept. 1982), pp. 79–100.

[Bar89] RJ Barlow. *A Guide to the Use of Statistical Methods in the Physical Sciences.* John Wiley, 1989.

[Bar97] F Barranco et al. “Role of finite nuclei on the pairing gap of the inner crust of neutron stars”. In: *Physics Letters B* 390.1-4 (1997), pp. 13–17.

[Bas15] D Basilico et al. "Outer crust of a cold non-accreting magnetar". In: *Physical Review C* 92.3 (2015), p. 035802.

[BB02] J Bartel and K Bencheikh. "Nuclear mean fields through self-consistent semiclassical calculations". In: *The European Physical Journal A-Hadrons and Nuclei* 14.2 (2002), pp. 179–190.

[BB17] GF Bertsch and D Bingham. "Estimating parameter uncertainty in binding-energy models by the frequency-domain bootstrap". In: *Physical Review Letters* 119.25 (2017), p. 252501.

[BC18] D Blaschke and N Chamel. "Phases of Dense Matter in Compact Stars". In: *The Physics and Astrophysics of Neutron Stars*. Ed. by L Rezzolla et al. Vol. 457. Astrophysics and Space Science Library. Cham: Springer International Publishing, 2018, pp. 337–400. arXiv: `1803.01836v2 [nucl-th]`.

[BE91] GF Bertsch and H Esbensen. "Pair correlations near the neutron drip line". In: *Annals of Physics* 209.2 (1991), pp. 327–363.

[Bei75] M Beiner et al. "Nuclear ground-state properties and self-consistent calculations with the Skyrme interaction:(I). Spherical description". In: *Nuclear Physics A* 238.1 (1975), pp. 29–69.

[BGH85] M Brack, C Guet, and HB Håkansson. "Selfconsistent Semiclassical Description of Average Nuclear Properties—a Link between Microscopic and Macroscopic Models". In: *Physics Reports* 123.5 (July 1985), pp. 275–364.

[BJC76] M Brack, BK Jennings, and YH Chu. "On the extended Thomas-Fermi approximation to the kinetic energy density". In: *Physics Letters B* 65.1 (1976), pp. 1–4.

[BK08] KH Bennemann and JB Ketterson. *Superconductivity: Volume 1: Conventional and Unconventional Superconductors Volume 2: Novel Superconductors*. Springer Science & Business Media, 2008.

[BO09] LS Bastos and A O'Hagan. "Diagnostics for Gaussian process emulators". In: *Technometrics* 51.4 (2009), pp. 425–438.

[BPS71] G Baym, C Pethick, and P Sutherland. "The ground state of matter at high densities: equation of state and stellar models". In: *The Astrophysical Journal* 170 (1971), p. 299.

[Bro00] EF Brown. “Nuclear heating and melted layers in the inner crust of an accreting neutron star”. In: *The Astrophysical Journal* 531.2 (2000), p. 988.

[BRT06] A Burrows, S Reddy, and TA Thompson. “Neutrino opacities in nuclear matter”. In: *Nuclear Physics A* 777 (2006), pp. 356–394.

[BST06] M Baldo, EE Saperstein, and SV Tolokonnikov. “The role of the boundary conditions in the Wigner–Seitz approximation applied to the neutron star inner crust”. In: *Nuclear Physics A* 775.3-4 (2006), pp. 235–244.

[Bur15] S Burrello et al. “Heat capacity of the neutron star inner crust within an extended nuclear statistical equilibrium model”. In: *Physical Review C* 92.5 (2015), p. 055804.

[BY02] A Bulgac and Y Yu. “Renormalization of the Hartree-Fock-Bogoliubov equations in the case of a zero range pairing interaction”. In: *Physical Review Letters* 88.4 (2002), p. 042504.

[BZ34] W Baade and F Zwicky. “Remarks on Super-Novae and Cosmic Rays”. In: *Physical Review* 46.1 (July 1934), pp. 76–77.

[Cao06] LG Cao et al. “From Brueckner approach to Skyrme-type energy density functional”. In: *Physical Review C* 73.1 (2006), p. 014313.

[Car20] T Carreau et al. “Crystallization of the Inner Crust of a Neutron Star and the Influence of Shell Effects”. In: *Astronomy & Astrophysics* 635 (Mar. 2020), A84.

[CF16] N Chamel and AF Fantina. “Binary and Ternary Ionic Compounds in the Outer Crust of a Cold Nonaccreting Neutron Star”. In: *Physical Review C* 94.6 (Dec. 2016).

[CGM19] T Carreau, F Gulminelli, and J Margueron. “Bayesian analysis of the crust-core transition with a compressible liquid-drop model”. In: *The European Physical Journal A* 55.10 (2019), p. 188.

[CGP08] N Chamel, S Goriely, and JM Pearson. “Further Explorations of Skyrme–Hartree–Fock–Bogoliu Mass Formulas. IX: Constraint of Pairing Force to 1S0 Neutron-Matter Gap”. In: *Nuclear Physics A* 812.1 (Nov. 2008), pp. 72–98.

[CGP09] N Chamel, S Goriely, and JM Pearson. “Further Explorations of Skyrme-Hartree-Fock-Bogoliubov Mass Formulas. XI. Stabilizing Neutron Stars against a Ferromagnetic Collapse”. In: *Physical Review C* 80.6 (Dec. 2009).

[CH08] N Chamel and P Haensel. “Physics of neutron star crusts”. In: *Living Reviews in relativity* 11.1 (2008), p. 10.

[Cha07] N Chamel et al. “Validity of the Wigner-Seitz approximation in neutron star crust”. In: *Physical Review C* 75.5 (2007), p. 055806.

[Cha10] N Chamel. “Effective Contact Pairing Forces from Realistic Calculations in Infinite Homogeneous Nuclear Matter”. In: *Physical Review C* 82.1 (July 2010), p. 014313.

[Cha12] N Chamel. “Neutron conduction in the inner crust of a neutron star in the framework of the band theory of solids”. In: *Physical Review C* 85.3 (2012), p. 035801.

[Cha13] N Chamel. “Crustal Entrainment and Pulsar Glitches”. In: *Physical Review Letters* 110.1 (Jan. 2013), p. 011101.

[Cha15] N Chamel et al. “Neutron drip transition in accreting and nonaccreting neutron star crusts”. In: *Physical Review C* 91.5 (2015), p. 055803.

[Cha20] N Chamel. “Analytical determination of the structure of the outer crust of a cold nonaccreted neutron star”. In: *Physical Review C* 101.3 (2020), p. 032801.

[Cha98] E Chabanat et al. “A Skyrme parametrization from subnuclear to neutron star densities Part II. Nuclei far from stabilities”. In: *Nuclear Physics A* 635.1-2 (1998), pp. 231–256.

[Che10] LW Chen et al. “Density slope of the nuclear symmetry energy from the neutron skin thickness of heavy nuclei”. In: *Physical Review C* 82.2 (2010), p. 024321.

[Cla99] JW Clark. “Neural networks: New tools for modelling and data analysis in science”. In: *Scientific applications of neural nets*. Springer, 1999, pp. 1–96.

[CLS06] LG Cao, U Lombardo, and P Schuck. “Screening effects in superfluid nuclear and neutron matter within Brueckner theory”. In: *Physical Review C* 74.6 (2006), p. 064301.

[CP20] M Carnini and A Pastore. “Trees and Forests in Nuclear Physics”. In: *Journal of Physics G: Nuclear and Particle Physics* (2020).

[CV16] D Chatterjee and I Vidaña. “Do hyperons exist in the interior of neutron stars?” In: *The European Physical Journal A* 52.2 (2016), p. 29.

[DH00] F Douchin and P Haensel. “Inner edge of neutron-star crust with SLy effective nucleon-nucleon interactions”. In: *Physics Letters B* 485.1-3 (2000), pp. 107–114.

[DH03] DJ Dean and M Hjorth-Jensen. “Pairing in nuclear systems: from neutron stars to finite nuclei”. In: *Reviews of Modern Physics* 75.2 (2003), p. 607.

[DHS19] C Drischler, K Hebeler, and A Schwenk. “Chiral Interactions up to Next-to-Next-to-Next-to-Leading Order and Nuclear Saturation”. In: *Physical Review Letters* 122.4 (Jan. 2019), p. 042501.

[DLL02] P Danielewicz, R Lacey, and WG Lynch. “Determination of the equation of state of dense matter”. In: *Science* 298.5598 (2002), pp. 1592–1596.

[DPN16] D Davesne, A Pastore, and J Navarro. “Extended Skyrme equation of state in asymmetric nuclear matter”. In: *Astronomy & Astrophysics* 585 (2016), A83.

[Dri20] C Drischler et al. “How Well Do We Know the Neutron-Matter Equation of State at the Densities Inside Neutron Stars? A Bayesian Approach with Correlated Uncertainties”. In: *Physical Review Letters* 125.20 (Nov. 2020), p. 202702.

[Dut12] M Dutra et al. “Skyrme interaction and nuclear matter constraints”. In: *Physical Review C* 85.3 (2012), p. 035201.

[DZ95] J Duflo and AP Zuker. “Microscopic mass formulas”. In: *Physical Review C* 52.1 (1995), R23.

[Fan18] AF Fantina et al. “Crustal Heating in Accreting Neutron Stars from the Nuclear Energy-Density Functional Theory: I. Proton Shell Effects and Neutron-Matter Constraint”. In: *Astronomy & Astrophysics* 620 (Dec. 2018), A105.

[Fan20] AF Fantina et al. “Crystallization of the outer crust of a non-accreting neutron star”. In: *Astronomy & Astrophysics* 633 (2020), A149.

[For13] D Foreman-Mackey et al. “emcee: The MCMC Hammer”. In: *Publications of the Astronomical Society of the Pacific* 125.925 (Mar. 2013), p. 306. arXiv: `1202.3665 [astro-ph.IM]`.

[FP20] M Ferreira and C Providência. “Effect of the Crust on Neutron Star Empirical Relations”. In: *Physical Review D* 102.10 (Nov. 2020), p. 103003.

[Gan08] S Gandolfi et al. “Equation of State of Superfluid Neutron Matter and the Calculation of the S 0 1 Pairing Gap”. In: *Physical Review Letters* 101.13 (2008), p. 132501.

[GAO12] KC Gendreau, Z Arzoumanian, and T Okajima. “The Neutron star Interior Composition ExploreR (NICER): an Explorer mission of opportunity for soft x-ray timing spectroscopy”. In: *Space Telescopes and Instrumentation 2012: Ultraviolet to Gamma Ray*. Vol. 8443. International Society for Optics and Photonics. 2012, p. 844313.

[Gao13] Y Gao et al. “Propagation of uncertainties in the Skyrme energy-density-functional model”. In: *Physical Review C* 87.3 (2013), p. 034324.

[GC14] S Goriely and R Capote. “Uncertainties of mass extrapolations in Hartree-Fock-Bogoliubov mass models”. In: *Physical Review C* 89.5 (2014), p. 054318.

[GCP09a] S Goriely, N Chamel, and JM Pearson. “Recent Breakthroughs in Skyrme-Hartree-Fock-Bogoliubov Mass Formulas”. In: *The European Physical Journal A* 42.3 (Dec. 2009), p. 547.

[GCP09b] S Goriely, N Chamel, and JM Pearson. “Skyrme-Hartree-Fock-Bogoliubov Nuclear Mass Formulas : Crossing the 0.6 MeV Accuracy Threshold with Microscopically Deduced Pairing”. In: *Physical Review Letters* 102 (2009), p. 152503.

[GCP13] S Goriely, N Chamel, and JM Pearson. “Further explorations of Skyrme-Hartree-Fock-Bogoliubov mass formulas. XIII. The 2012 atomic mass evaluation and the symmetry coefficient”. In: *Physical Review C* 88.2 (2013), p. 024308.

[Gey92] CJ Geyer. “Practical Markov chain Monte-Carlo”. In: *Statistical science* (1992), pp. 473–483.

[GK66] GT Garvey and I Kelson. “New nuclidic mass relationship”. In: *Physical Review Letters* 16.5 (1966), p. 197.

[GL12] RB Gramacy and HKH Lee. “Cases for the Nugget in Modeling Computer Experiments”. In: *Statistics and Computing* 22.3 (May 2012), pp. 713–722.

[GMS11] F Grill, J Margueron, and N Sandulescu. “Cluster structure of the inner crust of neutron stars in the Hartree-Fock-Bogoliubov approach”. In: *Physical Review C* 84.6 (2011), p. 065801.

[Gol68] T Gold. “Rotating Neutron Stars as the Origin of the Pulsating Radio Sources”. In: *Nature* 218.5143 (May 1968), pp. 731–732.

[GP08] S Goriely and JM Pearson. “Further Explorations of Skyrme-Hartree-Fock-Bogoliubov Mass Formulas. VIII. Role of Coulomb Exchange”. In: *Physical Review C* 77.3 (Mar. 2008), p. 031301.

[GPy20] GPy. *GPy: A Gaussian process framework in python*. `http://github.com/SheffieldML/GPy`. Version 1.9.9. Feb. 22, 2020.

[GR15] F Gulminelli and Ad R Raduta. “Unified Treatment of Subsaturation Stellar Matter at Zero and Finite Temperature”. In: *Physical Review C* 92.5 (Nov. 2015), p. 055803.

[Gre19] SK Greif et al. "Equation of state sensitivities when inferring neutron star and dense matter properties". In: *Monthly Notices of the Royal Astronomical Society* 485.4 (2019), pp. 5363–5376.

[Gui06] PAM Guichon et al. "Physical origin of density dependent forces of Skyrme type within the quark meson coupling model". In: *Nuclear Physics A* 772.1-2 (2006), pp. 1–19.

[GV79] B Grammaticos and A Voros. "Semiclassical approximations for nuclear hamiltonians. I. Spin-Independent Potentials". In: *Annals of Physics* 123 (1979), p. 359.

[GW10] J Goodman and J Weare. "Ensemble Samplers with Affine Invariance". In: *Communications in Applied Mathematics and Computational Science* 5.1 (Jan. 2010), pp. 65–80.

[GW19] A Gration and MI Wilkinson. "Dynamical modelling of dwarf spheroidal galaxies using Gaussian-process emulation". In: *Monthly Notices of the Royal Astronomical Society* 485.4 (2019), pp. 4878–4892.

[Hew68] A Hewish et al. "Observation of a Rapidly Pulsating Radio Source". In: *Nature* 217.5130 (Feb. 1968), pp. 709–713.

[Hua21] WJ Huang et al. "The AME 2020 atomic mass evaluation (I). Evaluation of input data, and adjustment procedures". In: *Chinese Physics C* 45.3 (2021), pp. 030002–030002.

[IP82] N Iwamoto and CJ Pethick. "Effects of nucleon-nucleon interactions on scattering of neutrinos in neutron matter". In: *Physical Review D* 25.2 (1982), p. 313.

[Jin17] S Jin et al. "Coordinate-space solver for superfluid many-fermion systems with the shifted conjugate-orthogonal conjugate-gradient method". In: *Physical Review C* 95.4 (2017), p. 044302.

[Jod16] R Jodon et al. "Constraining the Surface Properties of Effective Skyrme Interactions". In: *Physical Review C* 94.2 (Aug. 2016), p. 024335.

[Köh76] HS Köhler. "Skyrme force and the mass formula". In: *Nuclear Physics A* 258.2 (1976), pp. 301–316.

[Kor14] M Kortelainen et al. "Nuclear energy density optimization: Shell structure". In: *Physical Review C* 89.5 (2014), p. 054314.

[KTB80] H Krivine, J Treiner, and O Bohigas. "Derivation of a fluid-dynamical lagrangian and electric giant resonances". In: *Nuclear Physics A* 336.2 (1980), pp. 155–184.

[Lah99] SN Lahiri. "Theoretical comparisons of block bootstrap methods". In: *Annals of Statistics* (1999), pp. 386–404.

[Lan32] LD Landau. "On the theory of stars". In: *Phys. Z. Sowjetunion* 1 (1932), pp. 285–288.

[Lat19] James M Lattimer. "Neutron Star Mass and Radius Measurements". In: *Universe* 5.7 (July 2019), p. 159.

[Lat77] JM Lattimer et al. "The Decompression of Cold Neutron Star Matter". In: *The Astrophysical Journal* 213 (Apr. 1977), p. 225.

[LEL99] B Link, RI Epstein, and JM Lattimer. "Pulsar constraints on neutron star structure and equation of state". In: *Physical Review Letters* 83.17 (1999), p. 3362.

[Les93] M Leshno et al. "Multilayer feedforward networks with a nonpolynomial activation function can approximate any function". In: *Neural Networks* 6.6 (1993), pp. 861–867.

[LH17] Y Lim and JW Holt. "Structure of Neutron Star Crusts from New Skyrme Effective Interactions Constrained by Chiral Effective Field Theory". In: *Physical Review C* 95.6 (June 2017), p. 065805.

[Li14] BA Li et al. "Topical Issue on Nuclear Symmetry Energy". In: *The European Physical Journal A* 50.2 (Feb. 2014), p. 9.

[LP04] JM Lattimer and M Prakash. "The physics of neutron stars". In: *Science* 304.5670 (2004), pp. 536–542.

[LS08] ZH Li and HJ Schulze. "Neutron Star Structure with Modern Nucleonic Three-Body Forces". In: *Physical Review C* 78.2 (Aug. 2008), p. 028801.

[LSW18] JJ Li, A Sedrakian, and F Weber. "Competition between delta isobars and hyperons and properties of compact stars". In: *Physics Letters B* 783 (2018), pp. 234–240.

[Man20] A Mantziris et al. "Neutron star matter equation of state including d^*-hexaquark degrees of freedom". In: *Astronomy & Astrophysics* 638 (2020), A40.

[Mar16] N Martin. "Modes Collectifs et Hydrodynamique Dans La Croûte Interne Des Étoiles à Neutrons". PhD thesis. Université Paris-Saclay, Sept. 2016.

[MHF14] S Maurizio, JW Holt, and P Finelli. "Nuclear pairing from microscopic forces: Singlet channels and higher-partial waves". In: *Physical Review C* 90.4 (2014), p. 044003.

[MNV02] J Margueron, J Navarro, and N Van Giai. "Instabilities of infinite matter with effective Skyrme-type interactions". In: *Physical Review C* 66.1 (2002), p. 014303.

[Mon20] C Mondal et al. "Structure and Composition of the Inner Crust of Neutron Stars from Gogny Interactions". In: *Physical Review C* 102.1 (July 2020), p. 015802.

[Mos18] ER Most et al. "New constraints on radii and tidal deformabilities of neutron stars from GW170817". In: *Physical Review Letters* 120.26 (2018), p. 261103.

[MU15] N Martin and M Urban. "Liquid-Gas Coexistence versus Energy Minimization with Respect to the Density Profile in the Inhomogeneous Inner Crust of Neutron Stars". In: *Physical Review C* 92.1 (July 2015), p. 015803.

[MVS08] J Margueron, N Van Giai, and N Sandulescu. "Equation of State in the Inner Crust of Neutron Stars: Discussion of the Unbound Neutrons States". In: *Exotic States of Nuclear Matter*. Ed. by U Lombardo et al. World Scientific, Singapore, Feb. 2008, pp. 362–369. arXiv: `0711.0106 [nucl-th]`.

[Nea12] RM Neal. *Bayesian learning for neural networks*. Vol. 118. Springer Science & Business Media, 2012.

[Nea97] RM Neal. *Monte Carlo Implementation of Gaussian Process Models for Bayesian Regression and Classification*. Jan. 28, 1997. arXiv: `physics/9701026`.

[Neu18] L Neufcourt et al. "Bayesian approach to model-based extrapolation of nuclear observables". In: *Physical Review C* 98.3 (2018), p. 034318.

[Neu19] Léo Neufcourt et al. "Neutron Drip Line in the Ca Region from Bayesian Model Averaging". In: *Physical Review Letters* 122.6 (Feb. 2019), p. 062502.

[Niu18] Z Niu et al. "High precision nuclear mass predictions towards a hundred kilo-electron-volt accuracy". In: *Science Bulletin* 63.12 (2018), pp. 759–764.

[NV16] T Nikšić and D Vretenar. ""Sloppy" nuclear energy density functionals: Effective model reduction". In: *Physical Review C* 94.2 (2016), p. 024333.

[NV73] JW Negele and D Vautherin. "Neutron star matter at sub-nuclear densities". In: *Nuclear Physics A* 207.2 (1973), pp. 298–320.

[Oer17] M Oertel et al. "Equations of state for supernovae and compact stars". In: *Reviews of Modern Physics* 89 (1 Mar. 2017), p. 015007.

[Ons08] M Onsi et al. "Semi-classical equation of state and specific-heat expressions with proton shell corrections for the inner crust of a neutron star". In: *Physical Review C* 77.6 (2008), p. 065805.

[OPP97] M Onsi, H Przysiezniak, and JM Pearson. “Equation of State of Stellar Nuclear Matter in the Temperature-Dependent Extended Thomas-Fermi Formalism”. In: *Physical Review C* 55.6 (June 1997), pp. 3139–3148.

[OV39] JR Oppenheimer and GM Volkoff. “On Massive Neutron Cores”. In: *Physical Review* 55.4 (Feb. 1939), pp. 374–381.

[OY94] K Oyamatsu and M Yamada. “Shell energies of non-spherical nuclei in the inner crust of a neutron star”. In: *Nuclear Physics A* 578.1-2 (1994), pp. 181–203.

[Pas08] A Pastore et al. “Microscopic calculation and local approximation of the spatial dependence of the pairing field with bare and induced interactions”. In: *Physical Review C* 78.2 (2008), p. 024315.

[Pas12] A Pastore. “Superfluid properties of the inner crust of neutron stars. II. Wigner-Seitz cells at finite temperature”. In: *Physical Review C* 86.6 (2012), p. 065802.

[Pas13] A Pastore et al. “Pairing in exotic neutron-rich nuclei near the drip line and in the crust of neutron stars”. In: *Physical Review C* 88.3 (2013), p. 034314.

[Pas17] A Pastore et al. “A new statistical method for the structure of the inner crust of neutron stars”. In: *Journal of Physics G: Nuclear and Particle Physics* 44.9 (2017), p. 094003.

[Pas19] A Pastore. “An introduction to bootstrap for nuclear physics”. In: *Journal of Physics G: Nuclear and Particle Physics* 46.5 (2019), p. 052001.

[Pas20] A Pastore et al. “Impact of statistical uncertainties on the composition of the outer crust of a neutron star”. In: *Physical Review C* 101.3 (2020), p. 035804.

[PBL11] A Pastore, S Baroni, and C Losa. “Superfluid properties of the inner crust of neutron stars”. In: *Physical Review C* 84.6 (2011), p. 065807.

[PC09] J Piekarewicz and M Centelles. “Incompressibility of neutron-rich matter”. In: *Physical Review C* 79.5 (2009), p. 054311.

[PC20] A Pastore and M Carnini. *Extrapolating from neural network models: a cautionary tale*. Dec. 11, 2020. arXiv: `2012.06605 [nucl-th]`.

[PCP20] JM Pearson, N Chamel, and AY Potekhin. “Unified Equations of State for Cold Nonaccreting Neutron Stars with Brussels-Montreal Functionals. II. Pasta Phases in Semiclassical Approximation”. In: *Physical Review C* 101.1 (Jan. 2020), p. 015802.

[PCS20] L Perot, N Chamel, and A Sourie. “Role of the Crust in the Tidal Deformability of a Neutron Star within a Unified Treatment of Dense Matter”. In: *Physical Review C* 101.1 (Jan. 2020), p. 015806.

[Pea12] JM Pearson et al. “Inner Crust of Neutron Stars with Mass-Fitted Skyrme Functionals”. In: *Physical Review C* 85.6 (June 2012), p. 065803.

[Pea15] JM Pearson et al. “Role of proton pairing in a semimicroscopic treatment of the inner crust of neutron stars”. In: *Physical Review C* 91.1 (2015), p. 018801.

[Pea18] JM Pearson et al. “Unified Equations of State for Cold Non-Accreting Neutron Stars with Brussels–Montreal Functionals – I. Role of Symmetry Energy”. In: *Monthly Notices of the Royal Astronomical Society* 481.3 (Dec. 2018), pp. 2994–3026.

[Pea19] JM Pearson et al. “Erratum: Unified Equations of State for Cold Non-Accreting Neutron Stars with Brussels-Montreal Functionals. I. Role of Symmetry Energy”. In: *Monthly Notices of the Royal Astronomical Society* 486.1 (June 2019), pp. 768–768.

[Per04] E Perlińska et al. “Local density approximation for proton-neutron pairing correlations: Formalism”. In: *Physical Review C* 69.1 (2004), p. 014316.

[PF19] J Piekarewicz and FJ Fattoyev. “Impact of the Neutron Star Crust on the Tidal Polarizability”. In: *Physical Review C* 99.4 (Apr. 2019), p. 045802.

[PFH14] J Piekarewicz, FJ Fattoyev, and CJ Horowitz. “Pulsar Glitches: The Crust May Be Enough”. In: *Physical Review C* 90.1 (July 2014), p. 015803.

[PGC11] JM Pearson, S Goriely, and N Chamel. “Properties of the Outer Crust of Neutron Stars from Hartree-Fock-Bogoliubov Mass Models”. In: *Physical Review C* 83.6 (June 2011), p. 065810.

[PSD17] A Pastore, M Shelley, and CA Diget. “Impact Of Pairing Correlations On The Chemical Composition Of The Inner Crust Of A Neutron Star”. In: *Proceedings of The 26th International Nuclear Physics Conference — PoS(INPC2016)*. Adelaide, Australia: Sissa Medialab, May 2017, p. 145.

[PVB97] PM Pizzochero, L Viverit, and RA Broglia. “Vortex-Nucleus Interaction and Pinning Forces in Neutron Stars”. In: *Physical Review Letters* 79 (18 Nov. 1997), pp. 3347–3350.

[Qi15] C Qi. “Theoretical uncertainties of the Duflo–Zuker shell-model mass formulae”. In: *Journal of Physics G: Nuclear and Particle Physics* 42.4 (2015), p. 045104.

[Ras00] M Rashdan. “A Skyrme parametrization based on nuclear matter BHF calculations”. In: *Modern Physics Letters A* 15.20 (2000), pp. 1287–1299.

[RB04] PG Reinhard and M Bender. “Mean Field: Relativistic versus Non-relativistic”. In: *Lectures Notes in Physics: “Extended Density Functionals in Nuclear Structure Physics”*. Vol. 268. Springer, 2004, pp. 249–268.

[RHS06] SB Rüster, M Hempel, and J Schaffner-Bielich. “Outer crust of nonaccreting cold neutron stars”. In: *Physical Review C* 73.3 (2006), p. 035804.

[Roc11] X Roca-Maza et al. “Neutron skin of Pb 208, nuclear symmetry energy, and the parity radius experiment”. In: *Physical Review Letters* 106.25 (2011), p. 252501.

[RS80] P Ring and P Schuck. *The Nuclear Many-Body Problem*. Springer-Verlag, 1980.

[RW06] CE Rasmussen and CKI Williams. *Gaussian Processes for Machine Learning*. Adaptive Computation and Machine Learning. Cambridge, Mass: MIT Press, 2006.

[Sal61] EE Salpeter. “Energy and Pressure of a Zero-Temperature Plasma.” In: *The Astrophysical Journal* 134 (Nov. 1961), p. 669.

[Sch19] B Schuetrumpf et al. “Survey of Nuclear Pasta in the Intermediate-Density Regime: Shapes and Energies”. In: *Physical Review C* 100.4 (Oct. 2019), p. 045806.

[Sci20] SciPy 1.0 Contributors et al. “SciPy 1.0: Fundamental Algorithms for Scientific Computing in Python”. In: *Nature Methods* 17.3 (Mar. 2020), pp. 261–272.

[SG86] H Stoecker and W Greiner. “High energy heavy ion collisions—probing the equation of state of highly excited hardronic matter”. In: *Physics Reports* 137.5-6 (1986), pp. 277–392.

[Sha15] BK Sharma et al. “Unified Equation of State for Neutron Stars on a Microscopic Basis”. In: *Astronomy & Astrophysics* 584 (Dec. 2015), A103.

[She19] M. Shelley et al. “Advanced Statistical Methods to Fit Nuclear Models”. In: vol. 12. 3. 2019, p. 649.

[She21] M Shelley. *etf*. `http://github.com/mgeshelley/etfFinal`. Version 1.0. Apr. 2, 2021.

[Sky56] THR Skyrme. “CVII. The nuclear surface”. In: *Philosophical Magazine* 1.11 (1956), pp. 1043–1054.

[SLP18] A Sobiczewski, YA Litvinov, and M Palczewski. “Detailed illustration of the accuracy of currently used nuclear-mass models”. In: *Atomic Data and Nuclear Data Tables* 119 (2018), pp. 1–32.

[SP20] M Shelley and A Pastore. “How accurately can the extended Thomas-Fermi method describe the inner crust of a neutron star?” In: vol. 1668. 2020, p. 012037.

[SR14] R Sellahewa and A Rios. “Isovector Properties of the Gogny Interaction”. In: *Physical Review C* 90.5 (Nov. 2014), p. 054327.

[ST08] SL Shapiro and SA Teukolsky. *Black holes, white dwarfs, and neutron stars: The physics of compact objects.* John Wiley & Sons, 2008.

[Ste05] AW Steiner et al. “Isospin asymmetry in nuclei and neutron stars”. In: *Physics Reports* 411.6 (2005), pp. 325–375.

[Ste08] AW Steiner. “Neutron star inner crust : Nuclear physics input”. In: *Physical Review C* 77 (2008), p. 035805.

[Ste13] PD Stevenson et al. “Do Skyrme forces that fit nuclear matter work well in finite nuclei?” In: *AIP Conference Proceedings.* Vol. 1529. 1. American Institute of Physics. 2013, pp. 262–268.

[SVL04] N Sandulescu, N Van Giai, and RJ Liotta. “Superfluid properties of the inner crust of neutron stars”. In: *Physical Review C* 69.4 (2004), p. 045802.

[SW06] TE Strohmayer and AL Watts. “The 2004 Hyperflare from SGR 1806–20: Further Evidence for Global Torsional Vibrations”. In: *The Astrophysical Journal* 653.1 (2006), p. 593.

[TD95] C Thompson and RC Duncan. “The soft gamma repeaters as very strongly magnetized neutron stars-I. Radiative mechanism for outbursts”. In: *Monthly Notices of the Royal Astronomical Society* 275.2 (1995), pp. 255–300.

[Tew13] I Tews et al. “Neutron Matter at Next-to-Next-to-Next-to-Leading Order in Chiral Effective Field Theory”. In: *Physical Review Letters* 110 (3 Jan. 2013), p. 032504.

[Tol39] RC Tolman. “Static Solutions of Einstein’s Field Equations for Spheres of Fluid”. In: *Physical Review* 55.4 (Feb. 1939), pp. 364–373.

[Tsa12a] D Tsang et al. “Resonant Shattering of Neutron Star Crusts”. In: *Physical Review Letters* 108.1 (Jan. 2012), p. 011102.

[Tsa12b] MB Tsang et al. “Constraints on the symmetry energy and neutron skins from experiments and theory”. In: *Physical Review C* 86.1 (2012), p. 015803.

[UPP16] R Utama, J Piekarewicz, and HB Prosper. “Nuclear mass predictions for the crustal composition of neutron stars: A Bayesian neural network approach”. In: *Physical Review C* 93.1 (2016), p. 014311.

[VB72] D Vautherin and DM Brink. “Hartree-Fock calculations with Skyrme’s interaction. I. Spherical nuclei”. In: *Physical Review C* 5.3 (1972), p. 626.

[Vid09] I Vidaña et al. “Density dependence of the nuclear symmetry energy: A microscopic perspective”. In: *Physical Review C* 80.4 (2009), p. 045806.

[Vid18] I Vidaña et al. “The d*(2380) in Neutron Stars—A New Degree of Freedom?” In: *Physics Letters B* 781 (2018), pp. 112–116.

[Wan17] M Wang et al. “The AME2016 atomic mass evaluation (II). Tables, graphs and references”. In: *Chinese Physics C* 41.3 (2017), p. 030003.

[Wel17] A Welker et al. “Binding Energy of Cu 79: Probing the Structure of the Doubly Magic Ni 78 from Only One Proton Away”. In: *Physical Review Letters* 119.19 (2017), p. 192502.

[WFF88] RB Wiringa, V Fiks, and A Fabrocini. “Equation of State for Dense Nucleon Matter”. In: *Physical Review C* 38.2 (Aug. 1988), pp. 1010–1037.

[WI03] G Watanabe and K Iida. “Electron screening in the liquid-gas mixed phases of nuclear matter”. In: *Physical Review C* 68.4 (2003), p. 045801.

[Wir93] RB Wiringa. “From Deuterons to Neutron Stars: Variations in Nuclear Many-Body Theory”. In: *Reviews of Modern Physics* 65.1 (Jan. 1993), pp. 231–242.

[WL11] N Wang and M Liu. “Nuclear mass predictions with a radial basis function approach”. In: *Physical Review C* 84.5 (2011), p. 051303.

[Wol13] RN Wolf et al. “Plumbing Neutron Stars to New Depths with the Binding Energy of the Exotic Nuclide Zn 82”. In: *Physical Review Letters* 110.4 (2013), p. 041101.

[WP17] G Watanabe and CJ Pethick. “Superfluid density of neutrons in the inner crust of neutron stars: new life for pulsar glitch models”. In: *Physical Review Letters* 119.6 (2017), p. 062701.

[WS33] E Wigner and F Seitz. “On the Constitution of Metallic Sodium”. In: *Physical Review* 43.10 (May 1933), pp. 804–810.

[WZ20] XH Wu and PW Zhao. “Predicting nuclear masses with the kernel ridge regression”. In: *Physical Review C* 101.5 (2020), p. 051301.

[Xu09] J Xu et al. "Locating the inner edge of the neutron star crust using terrestrial nuclear laboratory data". In: *Physical Review C* 79.3 (2009), p. 035802.

[Xu21] K Xu et al. *How neural networks extrapolate: From feedforward to graph neural networks*. Mar. 2, 2021. arXiv: `2009.11848v5 [cs.LG]`.

[ZFH17] JL Zdunik, M Fortin, and P Haensel. "Neutron star properties and the equation of state for the core". In: *Astronomy & Astrophysics* 599 (2017), A119.

[Zuk11] A Zuker. "The anatomy of the simplest Duflo-Zuker mass formula". In: *11th Symposium on Nuclei in the Cosmos*. Vol. 100. SISSA Medialab. 2011, p. 083.